Integrated-Optic Electrorefraction Modulators

by

Sasa Ristic

B.A.Sc., The University of British Columbia, 2001

A THESIS SUBMITTED IN PARTIAL FULFILLMENT OF
THE REQUIREMENTS FOR THE DEGREE OF

Doctor in Philosophy

in

The Faculty of Graduate Studies

(Electrical and Computer Engineering)

The University of British Columbia

April 2007

Abstract

The large electroabsorption (EA) and electrorefraction (ER) effects that can be achieved in coupled quantum well (CQW) structures give these structures great potential for use in intensity, phase, and polarization modulators for future optical links. This thesis focuses on designing structures that will result in state-of-the-art performance of CQW-based modulators.

In this thesis, a design for a push-pull polarization-modulation scheme is presented, and it requires placing multiple repetitions of two different CQW structures in the optical waveguide of the proposed polarization modulator. The main function of one of the two structures is to provide a large increase of the refractive index for the TM polarization, without a proportionate increase of the refractive index for the TE polarization. It is shown that this effect can be achieved by anticrossing light holes. The main function of the other structure is to provide a large decrease of the refractive index for the TE polarization, without a proportionate decrease of the refractive index for the TM polarization. It is shown that, although this effect can be efficiently achieved by anticrossing heavy holes, the CQW structures that achieve this effect by anticrossing electrons are less sensitive to the layer thickness and compositional variations that may be expected during the growth process. The large EA and ER effects in CQW structures are typically seriously compromised by the layer variations, and, it is shown in this thesis that decreasing the confinement of the anticrossing wave functions can decrease the sensitivities of the CQW structures to these variations. In addition, the very small confinement of light holes in the InGaAlAs-based material systems together with the small sensitivity of the light-hole band edge to the compositional variations, make the anticrossing of the light holes the most robust-to-growth and, therefore, the most promising mode of operation for CQW-based ER intensity, phase, and polarization modulators.

The absorption spectra of the novel CQW structures designed in this thesis are obtained using the variational method for solving the 1S exciton equation in the effective-mass, envelope-function approximation, and the electric-field-induced refractive index changes are obtained using the Kramers–Krönig relations.

Table of Contents

List of Figures

List of Abbreviations

ACQW	Asymmetric Coupled Quantum Well
AWG	Arrayed Waveguide Grating
CATV	Cable Television
CQW	Coupled Quantum Well
DFB	Distributed Feedback
DGD	Differential Group Delay
EA	Electroabsorption
EDFA	Earbium-Doped Fiber Amplifier
ER	Electrorefraction
HWHM	Half-Width-at-Half-Maximum
ITU	International Telecommunication Union
LAN	Local-Area Network
MQW	Multiple Quantum Well
NRZ	Non-Return-to-Zero
OOK	On-Off Keying
PCS	Personal Communications Services
QCSE	Quantum-Confined Stark Effect
QWPC	Quantum Well Polarization Conversion
RF	Radio Frequency
RZ	Return-to-Zero
RZ-DPSK	Return-to-Zero Differential-Phase-Shift-Keyed
SCM	Sub-Carriers Multiplexing
SNR	Signal-to-Noise Ratio
SQW	Square Quantum Well
TE	Transverse-Electric
TDM	Time-Division Multiplexing
TM	Transverse-Magnetic
VCSEL	Vertical-Cavity Surface-Emitting
WDM	Wavelength-Division Multiplexing

Acknowledgments

Throughout my PhD studies, I have received great love and support from my wife, Dr. Jelena Ristic, and for this, I am very thankful to her. I am also very thankful to my parents, Nada and Djordjo Ristic, and my sister, Sanja Ristic, for their understanding and emotional support.

Many thanks to my supervisor Dr. Nicolas Jaeger. Our seven-year relationship started when he accepted me in his laboratory as an undergraduate student who wanted to gain experimental experience. From the moment he took me in his laboratory, I was immediately sold on the field of Photonics before I even knew what exactly it was. It is difficult not to be affected by Dr. Jaeger's drive and passion for the field. His multifaceted mentorship guidance and support, which also meant generous financial support, help me develop into an independent and confident researcher.

I would also like to thank the Natural Sciences and Engineering Research Council of Canada (NSERC), the University of British Columbia, and the British Columbia Advanced Systems Institute for their financial support.

Thanks are due to several faculty members, primarily Dr. David Pulfrey. His support has helped me secure both external funding from the NSERC and internal funding from University Graduate Fellowship (UGF). I am very thankful for all the help and encouragement he has given me throughout my graduate and undergraduate studies and for making me feel that I could rely on his help in the future as well. The same is true for Dr. John Madden and Dr. Lukas Chrostowski, who have also been supportive of my work. Dr. Mario Beaudoin, who is in charge of the Nanofabrication Facility in the AMPEL building, has been very helpful and extremely approachable whenever I had any growth-related questions. I am grateful to him and also Dr. Tom Tiedje, from the Physics Department, for growth-related discussions.

Although, I have enjoyed many interesting research-related discussions with the following graduate UBC students from Dr. Pulfrey's group, I also cannot thank them enough for all the good times we have had. Thank you Dr. Leonardo Castro, Dylan McGuire, Dr. David John, and Paul Pereira. Also, I have been lucky to be surrounded by a great group of people in Dr. Jaeger's laboratory. Thank you Dr. Jeffrey Bull, Pejman Ghanipour, Michael Manarovici, Kyle MacDonald, Sameer Chandani, and Ryan Kisch.

Also, thanks are due to our dear friends who made Vancouver feel like home for me and my wife for the past 12 years. Thank you Nebojsa and Jelena Plavsic, Aleksandar and Vanja Vitkovic, Zanka and Aleksandar Lizdek, Jasna and Svetlana Sokolovic, Pedja Kesic, Sinisa and Ljubica Predojevic, Igor Rudic and Snezana Slavic, and, particularly, Ljubomir Kaludjercic and Dijana Mandic with their children, our nieces, Ksenija and Katarina Kaludjercic.

Co-Authorship Statement

The work presented in this thesis was a collaboration between me and my supervisor, in which I took the leading role.

Chapter 1
Introduction

High-speed optical fiber communication networks play a vital role in the ongoing information revolution. Consequently, there is a huge demand for improving performance of the optical networks and their components, such as: semiconductor lasers, photodetectors, and electro-optic modulators. The research objective of this thesis is to make a contribution to the area of optical communications by pursuing the development of InGaAlAs-based electro-optic modulators using coupled quantum well (CQW) structures [1]–[3]. Electro-optic modulators based on CQW structures have the potential to become a leading technology for efficient high-speed conversion of electrical into optical signals, not only in optical communications but also in signal processing and instrumentation. This is mainly because CQW structures provide very large electroabsorption effect (electric-field-induced change of optical absorption) and electrorefraction effect (electric-field-induced change of refractive index) and should enable modulators based on them to have shorter lengths and lower drive voltages than

modulators based on square quantum wells or on the linear electro-optic effect. Both the short lengths and the low drive voltages possible with CQW modulators will be essential requirements for next-generation high-speed optical networks, which will, in turn, require electro-optic modulators having bandwidths of 100 GHz and above. [4]

In this thesis, a design for the first push-pull polarization modulator that is based on any type of quantum well structure is presented [1]. The effect is achieved by placing multiple repetitions of two types of CQW structure in the optical waveguide of the modulator. Upon the application of an electric field normal to the planes of the quantum wells, one of the structures mainly provides a positive change of the refractive index for the TM polarization, while the other structure mainly provides a similar negative change of the refractive index for the TE polarization. As a result, an input polarization state containing equal powers in both the TE and TM fundamental modes of the waveguide can be switched between orthogonal states. Polarization modulation has been traditionally associated with linear electro-optic modulators, and it has been used in an increasing number of modulation schemes, which have provided considerable improvements to the systems using them [5]. The CQW polarization modulator design presented in this thesis will enable these modulation schemes to be applied in next-generation high-speed optical networks as well.

Although they provide large electroabsorption and electrorefraction effects, CQW structures are quite sensitive to the layer thickness and compositional variations that are likely to occur in their quantum well layers during growth processes [2], [3]. The layer variations severely affect the properties of CQW structures, reducing the magnitude of the electroabsorption and electrorefraction effects that can be achieved. This thesis also presents a method that can be used to decrease the sensitivities of CQW structures to layer variations and, thus, significantly improve the magnitude of the electroabsorption and electrorefraction effects achievable with these structures. The method is mainly based on decreasing confinement of the electronic states in the CQW structures to their quantum well layers [3], and it can be used to improve not only the performance of the polarization modulator, but also the performance of electroabsorption and electrorefraction modulators in general. The large improvement achievable is expected to make a considerable impact on the state-of-the-art of electro-optic modulators.

The discussion of CQW modulators begins in Section 1.5 of this Introduction, Chapter 1, and continues throughout Chapters 2–6, which contain manuscripts that have been published, have been submitted for publication, or will be submitted for publication in journals. The last chapter of this thesis, Chapter 7, presents a discussions that relates Chapters 2–6 to each other, and to the field of optical fiber communications in general, and it also gives recommendations for future work on CQW modulators. The remainder of the Introduction starts with a discussion of analog and digital optical links (Section

1.1), which is followed by a comparison of directly modulated transmitters (Section 1.2) and linear electro-optic effect based external modulators (Section 1.3) for use in these optical links. Section 1.3 presents an overview of the most common linear electro-optic effect based external modulators: semiconductor polarization modulators, semiconductor Mach–Zehnder modulators, semiconductor mode converters, $LiNbO_3$-based modulators, and polymer modulators. More specifically, Section 1.3.7 presents a comparison of the linear electro-optic effect based external modulators and gives a motivation for using quantum well based modulators in modern optical links. In Section 1.4, a discussion of the electroabsorption effect in square quantum wells (Section 1.4.1) is followed by a discussion of the electrorefraction effect in them (Section 1.4.2) and by a comparison of these two types of modulator (Section 1.4.2). Although the discussion of square quantum well modulators in Section 1.4 points to the qualities that make them very popular in today's optical links, it also reveals the shortcomings that motivate research into CQW modulators.

1.1 Optical Fiber Communications

Today's global need for greater telecommunication network capacities seems insatiable. In the 1970s, the transmission loss of optical fibers was reduced to only ~0.5 dB/km within a 12 THz spectral region near 1310 nm and to only ~0.2 dB/km within a 15 THz spectral region near 1550 nm [6]. It was clear that data transmission capacities of optical

fibers would eventually overshadow those achievable with the copper wire [7]. Subsequently, a global research effort was initiated in order to develop optical transmitters and receivers operating around both 1310 nm and 1550 nm. Although the spectral region around 1550 nm has smaller optical loss than that around 1310 nm, and is dominant in long-haul communications, the region near 1310 nm has also been widely used in fiber-optic communications as the group-velocity dispersion is zero, *i.e.*, the dispersion changes sign, close to 1310 nm. Besides optical loss, group-velocity dispersion in fibers is one of the most important properties limiting the performance of a communication system [8]. It is also worth mentioning that the first-generation fiber-optic systems operated in the region near 800 nm using multimode fiber. The relatively large loss in this region (~2.5 dB/km) and the intermodal dispersion [8] limited digital systems to bit rates of only ~45 Mbps and repeater spacing of only ~10 km [7]. Due to its cost-effectiveness and maturity, this short-wavelength technology has reemerged recently in short-haul applications, such as in local-area networks (LANs) [9].

1.1.1 Digital Communications

The majority of fiber-optic systems are digital and operate in the spectral range around 1550 nm. In these systems, data are typically encoded in binary representation. Among the various characteristics of lightwaves that can be modulated, *e.g.*, intensity, phase, frequency, and polarization, intensity modulation has been most commonly used mainly

because of the simplicity of the envelope photodetection [10]. Therefore, as will be explained in more detail below, optical transmitters are realized either by direct modulation or by external modulation of the intensity of light coming out of a semiconductor laser. In direct-modulation transmitters, the current of a semiconductor laser is directly modulated by the binary electrical data stream, which switches the intensity of the laser's output from the "on" state (maximum light intensity at the output) to the "off" state (almost no light at the output), and vice versa [11], see Fig. 1.1(a). In external-modulation transmitters, the intensity of light from a semiconductor laser is switched on and off by an external optical modulator, which has its electrical port driven by the digital data stream [10], see Fig. 1.1(b). The on-off modulation in digital optical systems is also referred to as on-off keying (OOK).

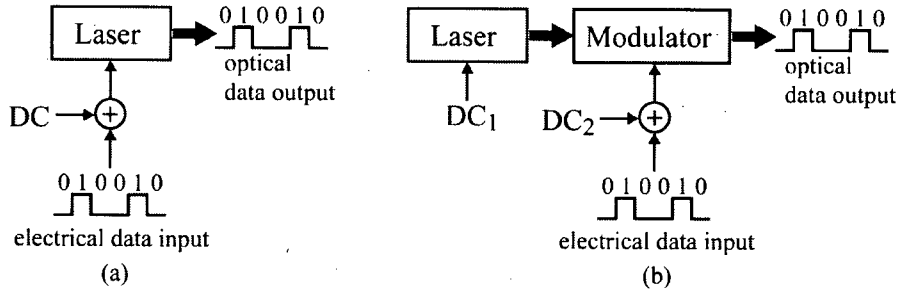

Figure 1.1: Schematics of an optical transmitter for digital communications: (a) directly-modulated semiconductor laser and (b) externally-modulated semiconductor laser.

In order to maximize the transmission capacity of a digital fiber-optic network, many different data streams at lower bit rates are commonly multiplexed to achieve higher bit rates in a single optical channel operating at a single wavelength. Typically, the

interleaving is done electronically, and is referred to as time-division multiplexing (TDM). The highest transmission rate in commercially available TDM systems is around 10 Gbps for each channel [12]. Many researchers are working on the next generation of TDM systems that will operate at 40 Gbps data rates. Traditionally, when planning future networks, service providers expect a fourfold increase in a network capacity at about 2.5 times the cost of the network equipment [13]. In combination with the TDM, commercial digital fiber-optic networks employ wavelength-division multiplexing (WDM), increasing the transmission capacities to about 1 Tbps [12]. In WDM links, many 10 Gbps (or lower bit rate) channels, each at a different carrier wavelength (λ), are multiplexed onto the same single-mode fiber using, for example, an arrayed waveguide grating (AWG) [14], as shown in Fig. 1.2. The channels form an infinite frequency grid centered at 193.1 THz, and are typically separated by 50 or 100 GHz, as regulated by the International Telecommunication Union (ITU) [12]. As also shown in Fig. 1.2, the multiplexed light is amplified by a cascade of erbium-doped fiber amplifiers (EDFAs), with about 100 km spacing between them [7], before entering the AWG demultiplexer at the other side of the link. Due to their ability to simultaneously amplify, in the optical domain, many WDM channels in the low-loss 1550 nm spectral region, EDFAs play a very important role in fiber-optic communications [15]. The gains of EDFAs cover the whole C-band (1530 nm–1565 nm) and a large part of the L-band (1565 nm–1625 nm), *i.e.*, the spectrum between 1565 nm and 1610 nm. For amplification of wavelengths shorter than these, including those around 1310 nm, Raman amplifiers are commonly

used [14] (Raman amplifiers are also used to complement EDFAs in ultra-long-haul systems). As shown in Fig. 1.2, at the end of a WDM link, which can be several thousand kilometers long [7], each channel is demultiplexed and passed to a separate receiver, which is a fast photodetector, for a simple envelope demodulation [14].

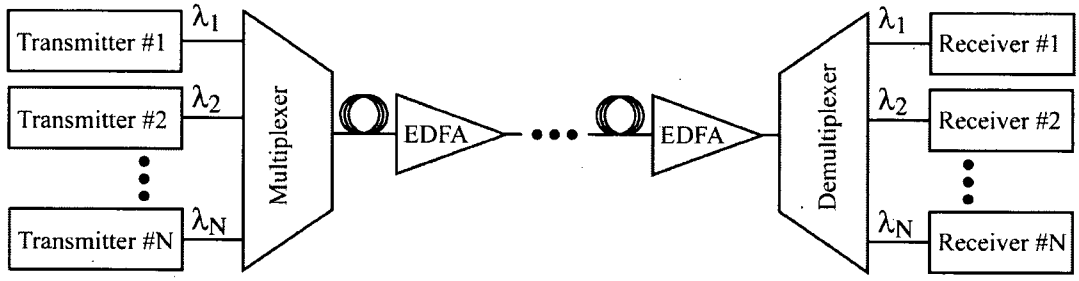

Figure 1.2: Schematics of a wavelength-division-multiplexed digital fiber-optic link.

1.1.2 Analog Communications

Although the vast majority of fiber-optic links are digital, there are an increasing number of applications for analog fiber-optic links. They are used for faithful transmission of RF signals over distances that are typically not as long as the distances covered by most digital links but are still too long for the use of coaxial cables. For example, the standard 3/8" coaxial cable exhibits a transmission loss of over 50 dB/km at the frequency of 1 GHz [16]. The fact that analog links mainly span relatively short distances makes the zero-dispersion 1310 nm spectral region very popular for these applications because the relatively high loss in the spectral region is not a limiting factor for short distances [11].

Similar to digital links, in analog links, transmitters are based on direct or external intensity modulation of semiconductor lasers, and the receivers are simply high-speed photodetectors. However, in analog links, the light intensity of the carrier is not switched on-off, but, rather, small-signal modulation is used in order to faithfully transmit the RF signal over the link. Small-signal modulation in analog links is more bandwidth-efficient than the OOK in digital links, and it also circumvents the costly analog-to-digital and digital-to-analog data conversion.

Some of the applications of analog links include the up-link (down-link) for cellular/PCS antenna remoting (here, PCS stands for Personal Communications Services), and transmit (receive) function in radar systems. Also, one of the first, and perhaps most commercial, applications of analog links was the distribution of cable television (CATV) signals [17]. Depending on the application, analog links can use only a single optical carrier, or they can employ wavelength-division multiplexing, similar to the digital links [18]. Also, similar to the TDM used in digital links for combining multiple signals into a single channel at a certain wavelength, sub-carrier multiplexing (SCM) is used in CATV systems to electronically combine multiple low-bandwidth signals onto the same carrier wavelength, as shown in Fig. 1.3 [19]. In an SCM link, N different signals (S_1 to S_N), each having a different RF carrier frequency (f_1 to f_N), are added into a larger bandwidth signal that modulates a semiconductor laser. At the other end of the fiber, the optical

signal enters the high-speed photodetector (PD), where it is converted back into an electrical signal. At the end of the link, N band pass filters (BPF_1 to BPFN) are used to separate the N input signals. Also, it is usual that some of the signals in an SCM link are digital.

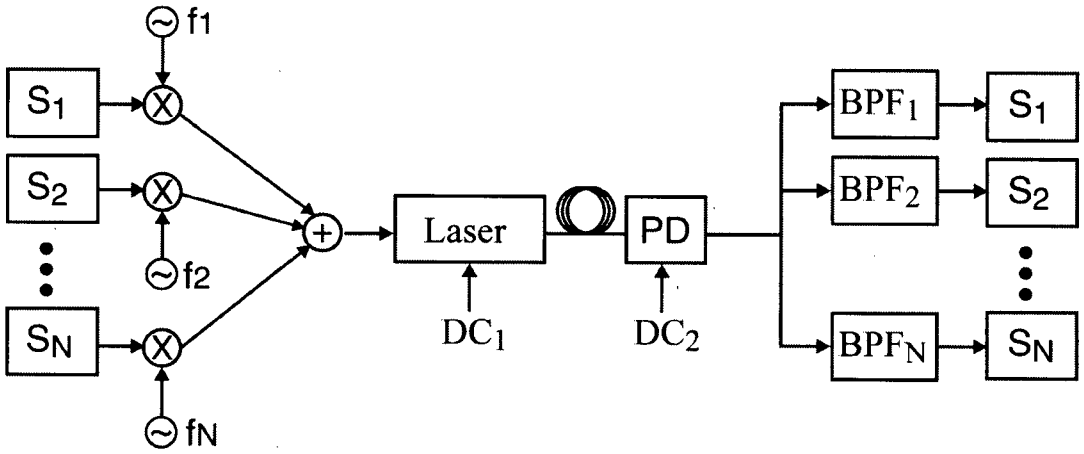

Figure 1.3: Schematics of a sub-carrier-multiplexed analog fiber-optic link.

1.2 Optical Transmitters

As mentioned above, optical transmitters used in both digital and analog fiber-optic links are based on either direct or external modulation of the light coming out of a semiconductor laser. The performance requirements for these transmitters depend on the application and whether the optical link in question is digital or analog. An overview of the performance requirements for optical transmitters, with an emphasis on external

modulators, is given in [10]; the most important of these requirements are summarized below.

One of the basic requirements for optical transmitters used in most digital links is, again, operation near 1550 nm. In addition, the transmitters are required to operate at high data rates, *i.e.*, have wide modulation bandwidths. In modern WDM links, data transmission capacities could be further increased by designing the links to have even larger numbers of low bit rate channels. However, such designs are difficult to implement because the optical multiplexing and demultiplexing circuits become very complex for large channel counts. Therefore, wide-modulation-bandwidth transmitters are very important for future high-capacity digital networks. An optical transmitter for digital links is also required to have large signal-to-noise ratio (SNR) and large extinction ratio. For example, an OOK transmitter should introduce as little noise into the system as possible. The device should leak as little light as possible when in its "off" state, and it should put out as much power as possible when in its "on" state. Also, as electronic drives that output more than 3.5 V become very expensive for data rates of 40 Gbps and higher, optical transmitters for the next-generation digital networks must have very low drive voltages. Finally, the last requirement for optical transmitters used in digital links, that will be mentioned here, is low chirp. Both directly modulated lasers and external intensity modulators introduce a certain amount of undesirable phase modulation in addition to the intensity modulation of the lightwave carrier. This effect results in an optical frequency (wavelength) chirp. In

optical waveguides that have nonzero group velocity dispersion, such as the common single-mode fibers used in the low loss 1550 nm spectral region, chirped optical pulses suffer excessive broadening and reduction of their peak powers. This effect limits the bit-rate-distance product (BL) in 1550 nm digital links, making them dispersion-limited, rather than loss-limited systems. One way of quantifying chirp in external modulators is using Henry's alpha parameter (α_H) [10], which is defined as the ratio between the change of the real part of the refractive index (δn) and the imaginary part of the refractive index (δk) in the optical waveguide of the modulator. An equivalent to α_H in directly modulated lasers is the "linewidth enhancement factor" and is defined in the same way. It can also be shown that

$$\alpha_H = \frac{\delta n}{\delta k} = -2I(t)\frac{\partial \Phi(t)/\partial t}{\partial I(t)/\partial t}, \tag{1.1}$$

where $\Phi(t)$ and $I(t)$ are time-dependent phase and intensity of light exiting the external modulator.

In analog links, low frequency chirp is not such an important requirement for optical transmitters, as analog links are typically shorter than digital links and many of them operate near 1310 nm, where common single-mode fiber has zero group velocity dispersion. Also, small-signal modulation, which is characteristic of analog links, typically introduces less frequency chirp than OOK in digital links. Similar to digital links, many analog links require very fast transmitters that introduce little noise into the

system, and output as much power as possible. Similar to digital transmitters, analog transmitters are required to achieve large changes in the intensity of light upon only small changes in the drive voltage, which is directly related to the so called small-signal modulation efficiency. Maybe the greatest difference between analog and digital transmitters is that the response of analog transmitters should be as linear as possible because in analog links data signals are supposed to be transmitted over the fiber link in a faithful manner without significant nonlinear distortions. There are several methods that can be used to compensate, to a certain degree, for nonlinear transmitter response, both in the electrical domain (*e.g.*, using pre-distortion circuitry) and in the optical domain (*e.g.*, cascading two external modulators in a way that their nonlinear responses cancel each other) [17]. Nonetheless, for these schemes to be effective, the transfer function of the transmitter should be as linear as possible. Finally, it is very important for analog transmitters, as well as the digital transmitters, to be affordable, to be insensitive to changes in temperature, and to have long lifetimes.

Having summarized the basic requirements for digital and analog transmitters, a performance comparison between the directly modulated transmitters and externally modulated transmitters will now be presented. The simplest and most economical way to implement an optical transmitter is to directly modulate the current of a semiconductor laser and, thus, modulate the intensity of its output light. Directly modulated lasers have small footprints and low power consumption. However, they have quite limited

frequency responses. The resonance frequencies of distributed feedback (DFB) lasers or vertical-cavity surface-emitting lasers (VCSELs) are typically lower than about 30 GHz [20]. As the modulation frequency is increased toward the resonance frequency, noise and non-linear distortions rapidly increase. In addition, directly modulated lasers generate significantly more chirp than most external modulators do. Although the performance of directly modulated lasers is being continuously improved using innovative methods, such as injection-locking [20], it is a widely accepted opinion that externally modulated lasers will continue to dominate in high-frequency (>20 GHz) links [10]. Furthermore, external modulators are essential for some modulation schemes, such as return-to-zero (RZ) modulation [14]. Unlike non-return-to-zero modulation (NRZ), where optical pulses completely fill the bit interval, in RZ modulation, optical pulses are much narrower than the bit interval. The NRZ modulation scheme was implied in Fig. 1.1. The RZ modulation scheme is illustrated in Fig. 1.4 below. Here, a pulse generator outputs a train of optical pulses that are significantly narrower than the bit interval, which is determined by the NRZ data stream driving the optical modulator. The optical modulator gates the pulses corresponding to "bit 0," outputting RZ optical data stream. Using a mode-locked laser as a pulse generator is not cost effective, and the pulses are typically generated by another external modulator that modulates the output of a DFB laser [14]. The major disadvantage of RZ modulation is that it requires modulators that have higher bandwidths than those used for NRZ modulation. Nonetheless, RZ modulation offers important

benefits, such as clock transitions for the receiver even when the data contains a long string of 1s [21].

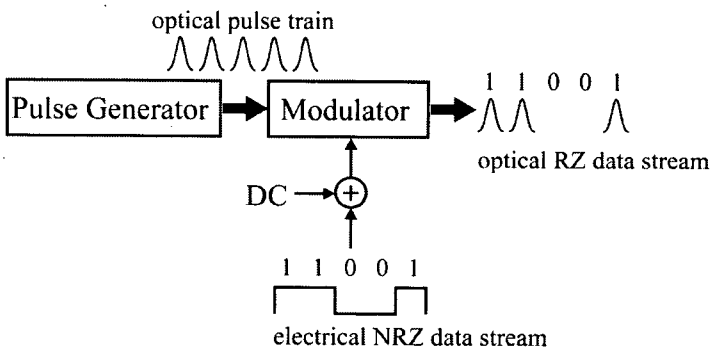

Figure 1.4: Return-to-zero optical modulation scheme.

As will be explained in more detail in the following discussion on external modulators, unlike directly modulated lasers, some external modulators are capable of modulating the polarization of light. Polarization-modulation schemes have provided great improvements to both the analog and digital links that use them.

1.3 Overview of External Modulators

In this section, an overview of most common external modulation technologies is presented. First, attention is paid to the technologies that use the linear electro-optic effect in crystals and do not need any quantum wells for optical modulation. Subsequently, the main limitations of these technologies are discussed, giving a

motivation for modulators based on quantum well structures, particularly those based on coupled quantum well structures, as they are the main focus of this thesis.

1.3.1 Linear Electro-Optic Effect in Semiconductors

In GaAs and other crystals having the zincblende structure (*e.g.*, InP), the change in the refractive index of the bulk crystal upon the application of the electric field (F) (after relatively simple tensor mathematics) can be shown to be one of the following three cases depending on the field direction [22]:

Case I: electric field applied in [001] direction

$$\begin{aligned} n[001] &= n_0 \\ n[\bar{1}10] &= n_0 + \Delta n \\ n[110] &= n_0 - \Delta n \end{aligned} \tag{1.2}$$

Case II: electric field applied in [110] direction

$$\begin{aligned} n[1\bar{1}0] &= n_0 \\ n[11\sqrt{\bar{2}}] &= n_0 + \Delta n \\ n[11\sqrt{2}] &= n_0 - \Delta n \end{aligned} \tag{1.3}$$

Case III: electric field applied in [111] direction

$$\begin{aligned} n[1\bar{1}0] &= n_0 + \frac{\Delta n}{\sqrt{3}} \\ n[11\bar{2}] &= n_0 + \frac{\Delta n}{\sqrt{3}} \\ n[111] &= n_0 - \frac{2\Delta n}{\sqrt{3}} \end{aligned} \tag{1.4}$$

In all of three cases, n_0 stands for the refractive index of the unperturbed, isotropic crystal, and

$$\Delta n = \frac{n_0^3}{2} r_{41} F, \tag{1.5}$$

where r_{41} (negative constant) is the electro-optic coefficient of the crystal. However, because [111]-cut substrates and electric fields in [111] direction are not very common, the first two cases (Case I and Case II) are typically used for electro-optic modulators, resulting in three different modulation schemes: polarization modulation, intensity modulation (using, for example, Mach–Zehnder interferometer), and mode conversion.

1.3.2 Semiconductor Polarization Modulators

A GaAs polarization modulator is shown in Fig. 1.5(a). Several micrometers of an $Al_xGa_{(1-x)}As$ epitaxial layer are first grown on top of (001) GaAs. Typically, in order to provide the vertical confinement of light, during the growth of the $Al_xGa_{(1-x)}As$ epitaxial layer, the Al mole fraction, x, is decreased in the region where the waveguide core is intended to be because the refractive index of the core needs to be higher than that of the cladding, and the refractive index of $Al_xGa_{(1-x)}As$ increases as x is decreased. When the top cladding layer is grown, x is increased to the same value it was for the bottom cladding layer. In order to provide the horizontal confinement of light, the AlGaAs is then etched to obtain a narrow, about 3 μm wide, optical single-mode ridge waveguide

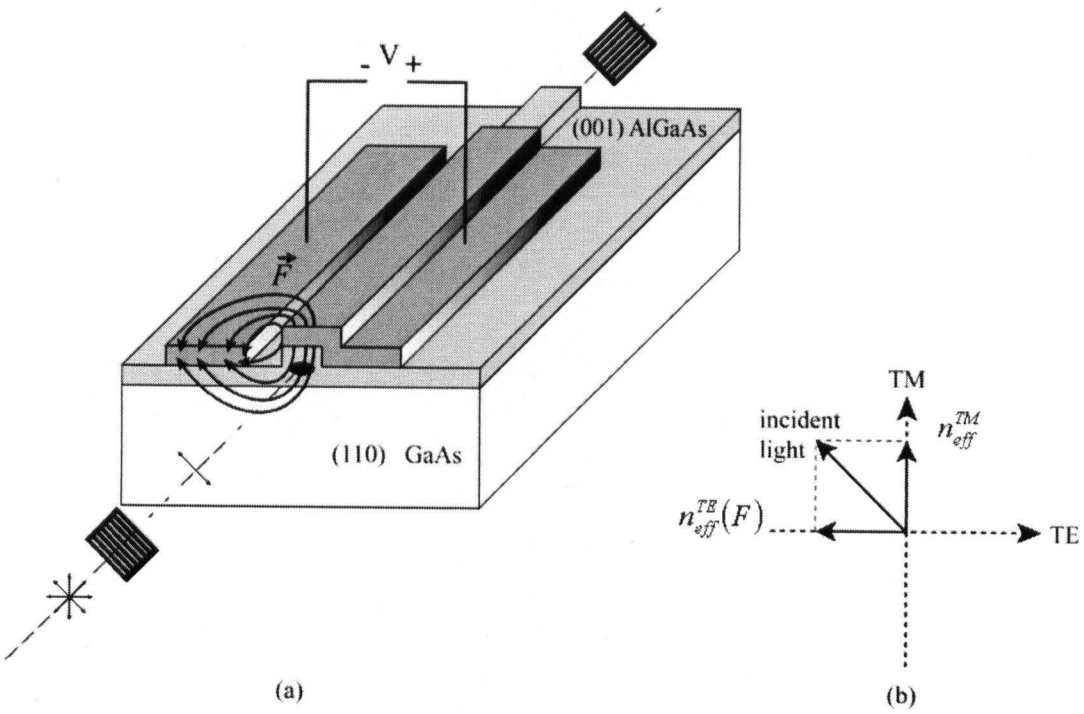

Figure 1.5: Semiconductor polarization modulator: (a) device schematics and (b) refractive index change directions (Case I).

parallel to the [110] direction. Once the optical waveguide has been fabricated, electrodes, which are about 1 μm thick and 100 μm wide, are formed, and the sample is cleaved along (110) plane in order to get smooth input and output facets of the waveguide. As it is only the vertical component of the applied electrical field that is utilized for the polarization modulation scheme, one of the electrodes is evaporated directly above the optical waveguide in order to maximize the field "seen" by the light traveling through the waveguide. It is also a common practice to deposit about 0.2 μm of an optical buffer layer on the substrate before the electrodes are formed. This decreases the optical loss in the waveguide due to the free electrons in the metal.

For these particular crystal and field orientations, the refractive index change will be as shown in the Case I: Refractive index in the vertical direction (refractive index "seen" by the transverse-magnetic (TM) polarized light, *i.e.*, the fundamental TM optical mode of the waveguide) will not change upon an application of the electric field, and the refractive index in the horizontal direction (refractive index "seen" by the transverse-electric (TE) polarized light, *i.e.*, the fundamental TE optical mode) will change by a small amount. The change of the refractive index along the direction of the waveguide, [110] direction, is unimportant because there is no appreciable longitudinal component of the optical field. Consequently, if the incident light is polarized at 45° with respect to [001] direction, which can be achieved by passing unpolarized light through a polarizer rotated at the same 45° with respect to [001] direction [see Fig. 1.5(a)], or by aligning highly polarized laser light with the 45° direction, the light couples equal amounts of power into the TE and TM modes, which "see" two different effective refractive indices (n_{eff}^{TE} and n_{eff}^{TM}, respectively). This is illustrated in Fig. 1.5(b). Here, it is important to note that a plane wave polarized, for example, in the [001] direction and propagating in bulk semiconductor crystal would "see" only the refractive index of the bulk crystal, *i.e.*, n_0. This is different from waveguide modes, such as the TM-polarized fundamental mode propagating in an optical waveguide, which will "see" an average refractive index that depends on the waveguide material and geometry as well as surrounding materials, *i.e.*, the effective refractive index for the fundamental TM mode(n_{eff}^{TM}).

As the TE and TM modes "see" different effective refractive indices, they will undergo different phase shifts after propagating the length of the waveguide (L), as given in the following two equations:

$$\phi_{TM} = \frac{\omega}{c} \cdot n_{eff}^{TM} \cdot L \tag{1.6}$$

$$\phi_{TE}(F) = \frac{\omega}{c} \cdot n_{eff}^{TE}(F) \cdot L, \tag{1.7}$$

where

$$n_{eff}^{TE}(F) = n_{eff}^{TE}(F = 0) + \Delta n_{eff}^{TE} \tag{1.8}$$

and

$$\Delta n_{eff}^{TE}(F) = \frac{\left(n_{eff}^{TE}(F = 0)\right)^3}{2} r_{41} F. \tag{1.9}$$

Also, here, ω is the frequency, and c is the speed of the light. The magnitude of r_{41} (1.4×10^{-12} m/V for wavelength near 1550 nm) is very nearly the same for GaAs and AlGaAs of the waveguide. The phase shift of the TM mode is just a passive phase shift, and it is not affected at all by the presence of the electrical field. The TE mode, however, in addition to the passive phase shift, experiences a phase shift proportional to the electric field. The phase difference between the two components at the output of the waveguide is often called "phase retardation." It can be easily shown that for a phase retardation of 180°, the polarization modulator can switch polarization of light between two orthogonal states using simple phase modulation of the fundamental TE mode [23].

If the waveguide was designed in such a way that $n_{eff}^{TE}(F=0)$ and n_{eff}^{TM} had the same magnitudes, and if no voltage (electric field) was applied, the TE and TM modes would undergo the same passive phase shifts. There would be no phase difference between them at the output of the device, where they would combine to form light polarized at the same angle as the incident light. If a polarizer is placed at the output of the device (such polarizer is often called the analyzer) and rotated 90° relative to the polarization of the incident light, as shown in Fig. 1.5(a), no light will go through the analyzer. However, if enough voltage is applied (V_π), the phase difference between the two modes at the output of the waveguide will be 180°, and this means that the polarization of the incoming light is rotated by 90°, so that all of the light will pass through the analyzer. Therefore, simply by adding the analyzer to a polarization modulator, the device can be used to convert polarization modulation into intensity modulation. The transfer function of the intensity modulator is described by the following expression [23]

$$\frac{I_{out}}{I_{in}} = \sin^2\left(\frac{\pi}{2}\frac{V}{V_\pi}\right), \tag{1.10}$$

where I_{in} and I_{out} are intensity of light at the input and the output of the waveguide, respectively, V is the applied voltage, and V_π (half-wave voltage) is the voltage needed to induce 180° of phase retardation between the two modes. The transfer function, which has the same functional form for all intensity modulators based on linear electro-optic effect, is also plotted in Fig. 1.6. If $n_{eff}^{TE}(F=0)$ is not matched to n_{eff}^{TM}, the transfer

function would have an extra phase term in the argument of the sinusoidal, which will move the function left or right on the horizontal axis.

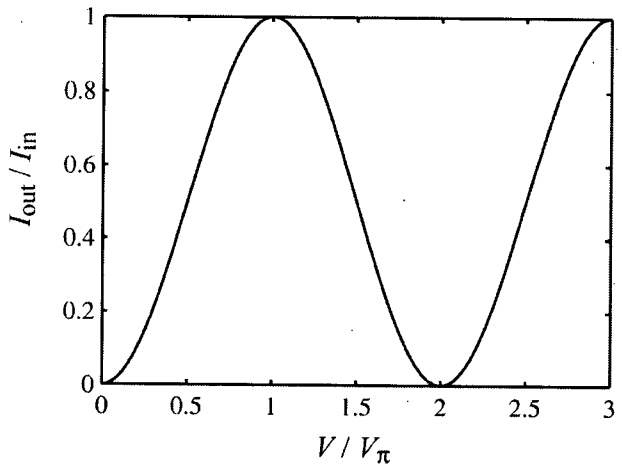

Figure 1.6: Intensity modulator transfer function.

If used as an intensity modulator for digital applications, this device would switch intensity of light from "off" state ($V = 0$) to "on" state ($V = V_{\pi}$). The transfer function given in Eq. (1.10) does not include the waveguide loss for the two modes. If the waveguide loss was included in Eq. (1.10), which is straightforward to do following the approach given in [23], it would be obvious that the waveguide loss is detrimental to the maximum optical power available from the device, and that differential loss between the two modes is detrimental to the extinctio ration of the device, which is defined as

$$Extinction\ Ratio = 10\log_{10}\left(\frac{I_{out}}{I_{in}}\right). \qquad (1.11)$$

Also, due to the fact that the effective refractive index changes for the two modes are not of the same magnitude and opposite sign, there will be a net phase change during the

operation of the device, and it will suffer from large frequency chirp. This is one of the main reasons why the polarization modulator is not widely used in digital communications.

If used in analog intensity-modulation applications, the device would be biased at $V = V_{\pi} / 2$, where the transfer function is most linear, and only small-signal modulation would be applied. Applications of polarization modulation, rather than intensity modulation, will be discussed below following the summary of the other most common polarization and intensity modulators.

1.3.3 Semiconductor Mach–Zehnder Modulators

A GaAs Mach–Zehnder intensity modulator is shown in Fig. 1.7. In this case, the incident TE light is split between two different waveguides, which in turn merge into a single output waveguide. The electrodes are designed and positioned in such a way that light traveling in one waveguide "sees" a vertical electric field pointing up, and the light in the other waveguide "sees" the vertical electric field pointing down. The orientation of the crystal is the same as for the polarization converter, so that the refractive index change is that of the Case I.

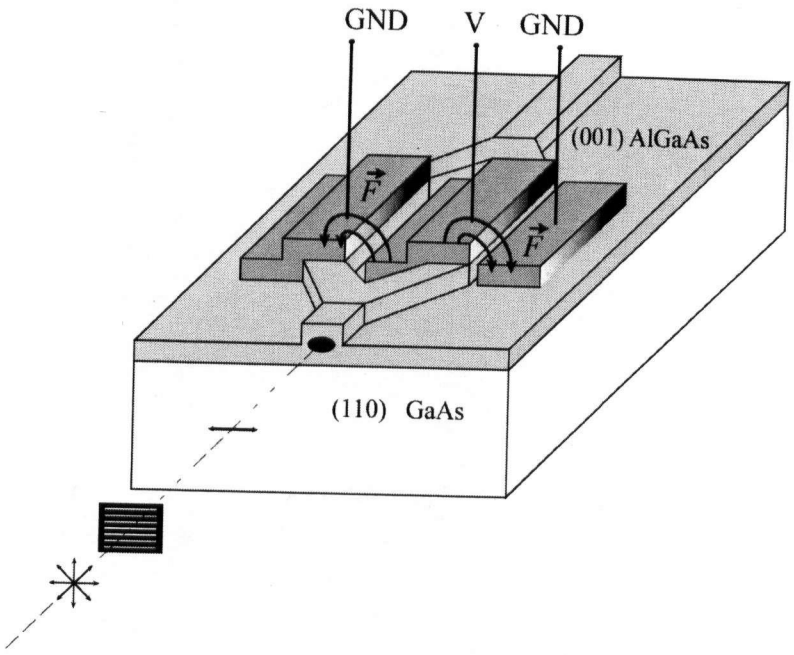

Figure 1.7: Semiconductor Mach–Zehnder intensity modulator (Case I).

In the Mach–Zehnder case, however, only TE light is launched into the device, and only the refractive index change in the horizontal direction matters. The refractive index changes in the two waveguides will have the same magnitude but opposite sign because of the opposite polarity of the field applied to each of the branches. If no field is applied to the device, the incident TE light splits into two equal-power components that undergo the same (only passive) phase shifts and add up in phase as the two branches merge into the single output waveguide. This is the "on" state of the modulator. When an electric field is applied to the device, the phase shift in one branch will be -90° and in the other +90°, so that the total phase retardation will be 180°. The two components of light will add up destructively upon merging into the single output waveguide, and the analyzer is

not needed. This is the "off" state of the modulator. This type of a Mach–Zehnder intensity modulator is called a "push-pull" Mach–Zehnder modulator [10], and its transfer function has the same sinusoidal form as shown in Fig. 1.6.

In theory, push-pull Mach–Zehnder modulators introduce no net phase change and do not suffer from the problem of chirp. In practice, it is impossible to fabricate the two branches of the modulator to have the same geometry and provide exactly the same magnitude of the refractive index change, which is required for "zero-chirp" operation. The problem of the two arms not being perfectly symmetric can be solved by driving the push-pull device differentially, *i.e.*, applying different voltages to the two electrodes of the device, which allows for the chirp to be fine-tuned to the desired value. However, if chirp is not an issue at all for a particular application, voltage can be applied to only one arm of the modulator and the intensity modulation would still be possible. When the two arms of the push-pull Mach–Zehnder modulator are not perfectly balanced, they will also have different waveguide losses and optical mode shapes, preventing the light signals from the two branches to cancel completely in the "off" state. Similarly, the splitting ratio of the input Y-splitter is never ideally 50:50. The imbalance between the two arms is the limiting factor for the extinction ratio in push-pull Mach–Zehnder modulators [10].

1.3.4 Semiconductor Mode-Conversion Modulators

An illustration of a mode converter is shown in Fig. 1.8 (a). As can be seen from the figure, the electric field is applied in the horizontal, [110], direction, and the refractive

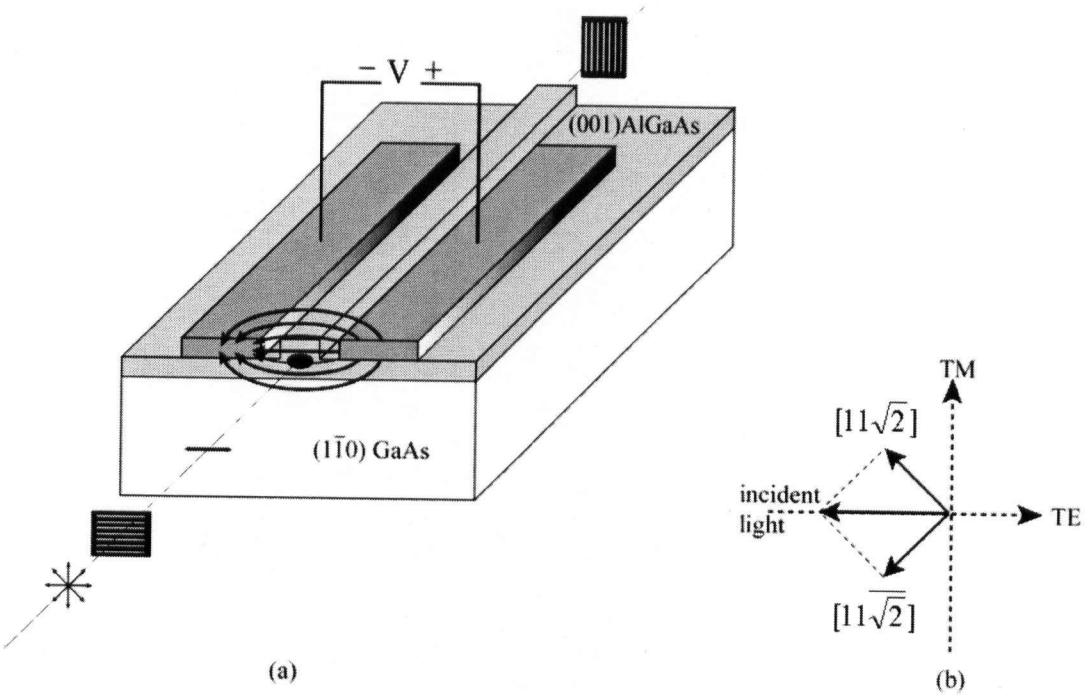

Figure 1.8: Semiconductor mode-conversion modulator: (a) device schematics and (b) refractive index change directions (Case II).

indices in $[11\sqrt{2}]$ and $[11\overline{\sqrt{2}}]$ directions (oriented ±45° with respect to the horizontal) will change by the same amount, although with opposite signs, corresponding to the Case II [see Fig. 1.8.(b)]. Horizontally polarized incident light (TE mode) can be thought of as being effectively split into the two equal-power "hybrid modes" components polarized along these two directions, as shown is Fig. 1.8(b). If no voltage is applied to the

electrodes, and if the effective refractive indices are the same for TE and TM modes, these two components will add up in phase at the output and combine into the TE mode again. If, however, enough voltage is applied to the electrodes (V_π), one of the vectors will undergo -90° phase shift and the other one will undergo +90° phase shift. The two components of light will then recombine at the output to form a TM mode. By definition, optical waveguide modes are states of light that do not change, unless somehow perturbed, as they propagate down a longitudinally invariant waveguide. The ability of the device to transfer power from one fundamental mode of the waveguide into another (TE into TM, or vice versa) is the reason the device is called a mode converter, not simply a polarization converter.

It is important to emphasize that complete mode conversion, which means that all power from one mode is transferred into the other, is possible only if the unperturbed (no external field condition) effective refractive indices of the TE and the TM mode are the same. This condition is also called the zero modal birefringence condition. In order to fully understand this, one can use the coupled-mode theory, rather than the simplistic explanation given above [24]. The effective refractive indices are inherently similar in III–V semiconductor optical waveguides. However, in order to achieve the low modal birefringence required for mode conversion, the geometry of the optical waveguide needs to be carefully designed. [4].

Similar to the polarization modulator, the 90° polarization rotation in a mode converter can be turned into intensity modulation simply by adding a cross-polarized analyzer. Its transfer function can be represented by Eq. (1.10) and illustrated by Fig. 1.6. Following the same logic as in the two previous modulation schemes, it is obvious that this is a push-pull device capable of zero-chirp operation. In comparison with the polarization modulator, the mode converter is twice as efficient because the material refractive index changes for two axes, not just one. Also, if the two modes experience different amounts of loss in the waveguide, the extinction ratio could be severely affected. Fortunately, the problem could be easily solved by rotating the input polarizer in order to put more power into the mode that suffers greater loss, matching the powers of the two modes at the output. In Mach–Zehnder modulators, the differential optical loss due to the imbalance of the two arms cannot be compensated so easily after the device has been fabricated.

1.3.5 Lithium Niobate Modulators

Modulators based on the linear electro-optic effect in Lithium Niobate ($LiNbO_3$) represent the most mature external optical modulator technology used in optical telecommunications. In them, optical waveguides are most often fabricated by diffusing titanium (Ti) into the crystal [10]. After the optical waveguide has been fabricated, its facets are polished, not simply cleaved as in III–V semiconductor modulators. Also, a thin optical buffer layer is often deposited on top of the waveguide (particularly for z-cut

modulators introduced below) to decrease the optical loss due to the metallic electrodes. Unlike the isotropic III–V semiconductors, $LiNbO_3$ is an anisotropic, uniaxial crystal. Its material refractive index in one direction is different from those in the other two directions. This special direction is called the extraordinary optical axis, and the refractive index corresponding to it is called the extraordinary refractive index (n_e). The other two axes are called the ordinary axes, and the refractive indices are called the ordinary refractive indices (n_o). When the crystal is used for its electro-optic effect, its extraordinary axis is called z-axis, and the other two axes are called x-axis and y-axis. Unlike, for example, the III–V semiconductor GaAs crystal that has only one nonzero electro-optic coefficient ($r_{41} = -1.4\times10^{-12}$ m/V), $LiNbO_3$ has 4 different nonzero electro-optic coefficients: $r_{33} = 30.8\times10^{-12}$, $r_{13} = 8.6\times10^{-12}$, $r_{22} = 3.4\times10^{-12}$, and $r_{51} = 28.0\times10^{-12}$ m/V [10]. The electro-optic effect in $LiNbO_3$ is typically used in three different modulation schemes, as shown in Fig. 1.9.

Upon the application of an electric field in the z direction (F_z), z-cut and y-propagating (waveguide is parallel to the y-axis) $LiNbO_3$ crystals will "see" the refractive index in the x direction change from n_o (~2.29) to

$$n_x' = n_o - \frac{n_o^3}{2} r_{13} F_z, \tag{1.12}$$

and the refractive index in the z direction change from n_e (~2.2) to

$$n_z' = n_e - \frac{n_e^3}{2} r_{33} F_z , \qquad (1.13)$$

as shown in Fig. 1.9(a). Because, $r_{33} >> r_{13}$, the phase of the vertical, TM, polarization is much more efficiently modulated than the phase of the horizontal, TE, polarization. This

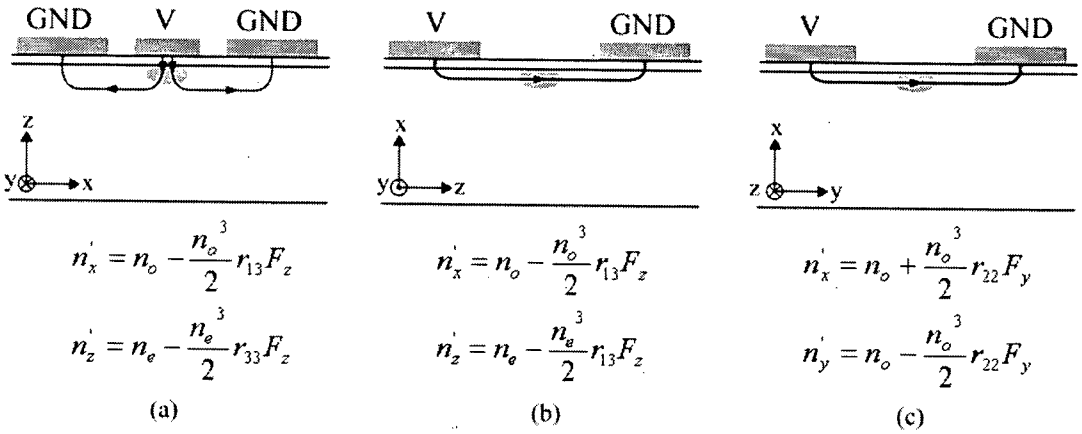

Figure 1.9: Lithium Niobate modulator: (a) z-cut, y-propagating device, (b) x-cut, y-propagating device, and (c) x-cut, z-propagating device.

type of refractive index change provides for an efficient TM-polarization phase/frequency modulator, TM-polarization Mach–Zehnder modulator, as well as a polarization converter, because the differential phase change for the TE and TM modes is quite large. The fact that the largest electro-optic coefficient for $LiNbO_3$, r_{33}, is more than twenty times larger than r_{41} for GaAs is somewhat deceiving, as it may seem that the refractive index change achievable in $LiNbO_3$ is more than twenty times larger than the one achievable in GaAs. However, the refractive index change in $LiNbO_3$ is only 3–4 times larger because it also strongly depends on the material refractive index itself, and the

isotropic material refractive index for GaAs (~3.4) is considerably larger than either the ordinary or extraordinary index of $LiNbO_3$.

Fig. 1.9(b) illustrates x-cut, y-propagating $LiNbO_3$. The refractive indices in the transverse x and z directions change in the same way as for z-cut, y-propagating $LiNbO_3$, except that here the z-axis and F_z are in the horizontal direction, so that x-cut, y-propagating $LiNbO_3$ is most appropriately used for TE-polarization phase/frequency/intensity modulation, or again, in polarization modulators.

Although in z-cut, y-propagating $LiNbO_3$ and x-cut, y-propagating $LiNbO_3$ efficient polarization modulation is possible, the polarization modulation is not push-pull. In addition, unlike the isotropic III–V semiconductors, y-propagating $LiNbO_3$ has large material birefringence ($n_o >> n_e$), which, in turn, results in large modal birefringence that cannot be simply overcome with any particular waveguide design. Consequently y-propagating $LiNbO_3$ polarization modulators suffer from large (10–15 ps) differential group delay (DGD) between the two modes, which is significantly larger than the DGD for GaAs mode converters (<0.5 fs). Such large DGD precludes y-propagating $LiNbO_3$ polarization modulators from being used in very important polarization-modulation applications [25].

Fig. 1.9(c) shows another typical $LiNbO_3$ modulation scheme. Here, $LiNbO_3$ is x-cut and z-propagating, and the electric field (F_y) is applied in the horizontal, y-direction. Consequently, the field-dependent refractive index in the x-direction,

$$n_x' = n_o + \frac{n_o^3}{2} r_{22} F_y, \tag{1.14}$$

and the field-dependent refractive index in the y-direction,

$$n_y' = n_o - \frac{n_o^3}{2} r_{22} F_y, \tag{1.15}$$

experience same-magnitude, opposite-sign changes from the unperturbed ordinary refractive index. The push-pull, low-modal-birefringence polarization modulation is ideal for certain long-haul applications [25], [26]. Unfortunately, r_{22} is quite a bit smaller than r_{33}, and the drive voltages in z-propagating $LiNbO_3$ modulators are larger than those in y-propagating $LiNbO_3$ modulators.

1.3.6 Polymer Modulators

Electro-optic polymers are an immature modulator technology [10], [27]. The polymers are synthetic organic materials obtained by embedding active electro-optic polymers, *i.e.*, nonlinear optical chromophores, into a matrix of a standard polymer host, such as PMMA. It is very easy to form multilayer polymer stacks using spin-coating, which makes polymers very easy to integrate with various optoelectronic circuits. Unlike

metallic electrodes on semiconductor epitaxial layers, metallic electrodes can be easily sandwiched between polymer layers. In order to obtain a macroscopic electro-optic effect from the microscopic electro-optic effect that is characteristic of chromophore molecules, the molecules need to be aligned. This is achieved by heating (in the range between 100 and 200 °C) and cooling the polymer in a strong electric field (100–200 V/μm). This process is called polling. The electrodes used to apply the polling field are often removed and replaced by more appropriate, typically faster, microwave electrodes.

After polling, the isotropic electro-optic polymer becomes uniaxial. Its extraordinary axis is aligned with the direction of the field, and its ordinary axis is normal to the direction of the applied field. The extraordinary material refractive index is $n_e = n + 2\Delta$, and the ordinary material refractive index is $n_o = n - \Delta$, where $n \approx 1.6$ and $\Delta \approx 0.1$. If the z axis is aligned with the extraordinary axis, and only electric field in z direction is applied, the refractive index change for electro-optic polymers will be similar to the one for z-cut, y-propagating $LiNbO_3$, as shown in Fig. 1.9(a), and Eqs. (1.12) and (1.13). r_{33} is about three times larger than r_{13}, and it could be increased if a greater polling field is applied. Unfortunately, the greater the polling field, the greater the material loss and birefringence. r_{33} can vary from several pm/V to ~100 pm/V. In electro-optic polymers, due to the low refractive index, r_{33} needs to be ~80 pm/V in order for the refractive index change of the polymer to be similar to that of $LiNbO_3$ for the same electric-field change.

Fig. 1.10 illustrates a push-pull Mach–Zehnder polymer modulator. During the polling process, the electric field is applied in opposite directions in two neighboring

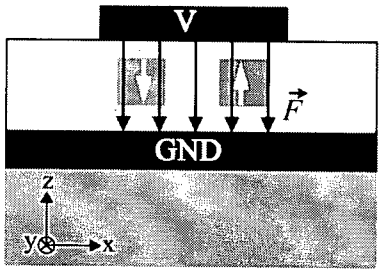

Figure 1.10: Cross-section of push-pull polymer Mach-Zehnder modulator.

regions containing the electro-optic polymer, providing for the push-pull effect. The two regions form the cores of the optical waveguides in the two branches of a Mach–Zehnder modulator. The opposite alignment of the molecules (white arrows) with respect to the applied electric field (black arrows) is indicated in the figure. The waveguide cores in the horizontal direction are defined by decreasing the refractive index of the surrounding material (cladding) using either dry etching or photobleaching techniques [10]. Light confinement in the vertical direction is achieved by spin-coating materials with lower refractive indices than that of the core, above and below the waveguide.

1.3.7 Comparison of Linear Electro-Optic Modulators

The preceding sections presented only the basics of some of the best known linear electro-optic modulation technologies. Here, a more detailed performance comparison of

the technologies is given. One of the most important performance requirements for optical modulators is wide electro-optic bandwidth. For example, future WDM links will require optical modulators to operate at data rates of 40 Gbps and higher. The optical modulators that will be used in future WDM links will, therefore, need to have electro-optic bandwidths greater than 30 GHz, depending on the spectral efficiency of the digital signal (ratio of the bit rate to the bandwidth), which depends on the modulation and coding schemes used in the links [21]. In addition, high-frequency operation must be achieved without sacrificing modulator performance, *e.g.*, the RF drive voltage should be less than 3.5 V [10].

Most high-frequency modulators, particularly those intended for operation at 40 Gbps and higher data rates, employ some type of traveling-wave electrodes, rather than lumped electrodes [28]. A lump electrode structure is basically a capacitor, such as shown in Fig. 1.8, connected in parallel with an impedance-matching resistor (typically, a 50 Ω resistor for broadband matching is used). In lumped electrode structures, the electrode length is short compared to the RF wavelength. The bandwidth of a lumped electrode structure is determined by the RC time constant, and the electro-optic bandwidth of the modulator is the smaller of the inverse of the RC time constant or the inverse of the time the light takes to propagate along the length of the capacitor, between its plates. The former is usually more limiting. In order to increase the electro-optic effect and lower the drive voltage, it is desirable to make the electrodes as long as possible, increasing the interaction between

the light and the modulating electric field. However, the capacitance increases with the electrode length, decreasing the bandwidth. As the linear electro-optic effect requires the electrodes of electro-optic modulators to be several centimeters long, traveling-wave electrodes need to be used. Even the short electroabsorption modulators ($L < 1$ mm), which will be described in more detail in the following section, have shown better performance using traveling-wave electrodes [29].

In traveling-wave electro-optic modulators, the modulating signal is applied to one end of the electrodes, and the other end of the electrodes is terminated with a resistive load. The impedance of both the electrode and the load are matched to the impedance of the source, which is typically 50 Ω, so the electrode can be considered to be an extension of the transmission line and its bandwidth is not limited by the electrode charging time. Here, the basic idea is that the modulating electric field launched at one end of the electrodes propagates down the traveling-wave electrode at the same speed as the light, which is launched in the same direction in the optical waveguide. If the two speeds are not matched, the light-electric-field interaction will not integrate effectively as the two waves propagate. In semiconductor modulators, the electrical signal travels faster than the optical signal and is relatively easily slowed down by capacitive loading, as illustrated in Fig. 1.11 [4], [30], [31].

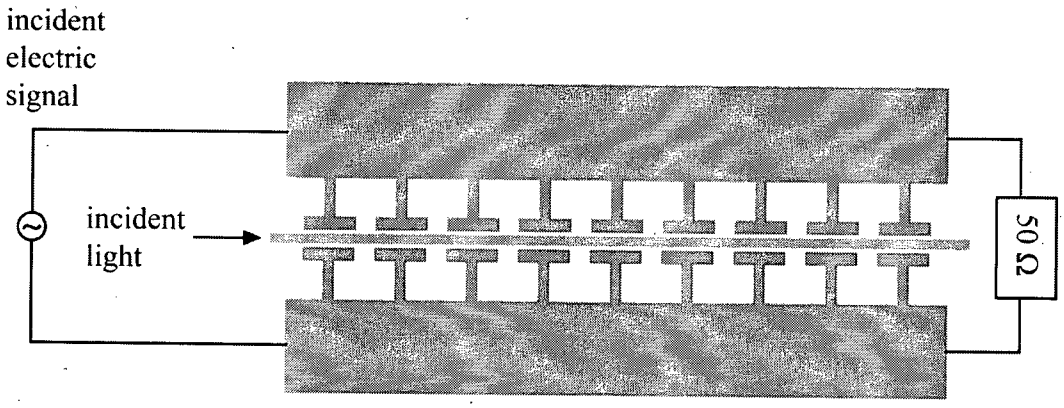

Figure 1.11: Top view of a mode converter with coplanar traveling-wave electrode with periodic T-shaped capacitive loads.

The electro-optic 3 dB bandwidth due to the velocity mismatch between the modulating signal and the optical mode is inversely proportional to the electrode length (L), as shown in the following equation

$$f_{3dB} = \frac{c}{L \cdot \left| n_{eff}^{elec} - n_{eff}^{opt} \right|}, \tag{1.16}$$

where n_{eff}^{elec} and n_{eff}^{opt} are the effective refractive index of the electrode structures and the effective refractive index of the optical mode, respectively, and c is the speed of light [4]. In $LiNbO_3$ modulators, unlike in III–V semiconductor modulators, the material refractive index for electromagnetic waves is significantly larger for the microwave/millimeterwave frequencies than it is for optical frequencies. Therefore, the velocity of the electrical signal in the traveling-wave electrode needs to be increased considerably for fine velocity matching, which is challenging to do without increasing the drive voltage [27].

The electro-optic bandwidth of modulators is also limited by the electrode microwave loss, which is usually more dominant than the velocity mismatch effect for very high frequencies. The electro-optic 3dB bandwidth due to electrode loss is inversely proportional to the square of the length of the electrodes, as shown below

$$f_{3dB} = \frac{2.54}{(\alpha_0 L)^2}, \tag{1.17}$$

where α_0 is a constant dependent on the dimensions and the resistivity of the electrodes, and L is, as before, the length of the electrode [4].

In addition, a very important design constraint for high-performance electro-optic modulators is impedance matching. If the impedance of an electrode is not closely matched to the impedance of the source and/or the termination, the modulator will suffer from large frequency-dependent reflection loss and resonance issues.

The large electro-optic effect in $LiNbO_3$ modulators (again, the effect is 3–4 times larger than that in GaAs) does not necessarily provide for a device that is strikingly shorter and, thus, faster than other electro-optic modulators, because of constraints such as impedance matching, velocity matching, and low drive voltages, as mentioned above. To the contrary, $LiNbO_3$ Mach–Zehnder modulators typically have the largest footprints of all the available modulator technologies, which is perceived as one of their major

disadvantages [10]. Although a $LiNbO_3$ Mach–Zehnder modulator with bandwidth greater than 75 GHz, having 2 cm long electrode, has been demonstrated, the drive voltage for the device was large (V_π = 5.1 V) [32]. The length of the electrode had to be extended to 3 cm and its bandwidth consequently lowered to 30 GHz, in order for the modulator, with otherwise the same design, to have a drive voltage of only 3.5 V. Besides their large footprint, bias instability in $LiNbO_3$ Mach–Zehnder modulators is also perceived as one of their major disadvantages. A sudden change of the bias voltage can trigger a slow bias drift with a time constant of several hours to several days. The bias drift is due to slowly moving charge that is either trapped in $LiNbO_3$ and SiO_2 buffer layers, or is trapped at their surfaces and interfaces. The charge can be process related or it can be generated during the operation of the device by thermal or optical excitation. To minimize the drift problem, $LiNbO_3$ surfaces should be treated, and, also, the conductivities of the layers should be matched [10]. Nevertheless, due to large investments in $LiNbO_3$, it is still considered the benchmark technology for the linear electro-optic modulators [10]. $LiNbO_3$ optical waveguides exhibit low loss (~0.2 dB/cm), they can handle the largest optical powers (10s to 100s of mW), and they can be designed for very efficient coupling with the standard single-mode fibers (5 dB fiber-to-fiber insertion loss) [27].

In contrast with $LiNbO_3$ modulators, polymer modulators are a very immature technology, which is not yet very popular in the marketplace [10]. The technology has a

major advantage of being inexpensive and easy to integrate with various devices. The small refractive indices of polymers (~1.6) make them well matched to optical fibers (refractive index of silica is ~1.46). Also, the small refractive index and its small change from optical frequencies to microwave frequencies, provides for easy fabrication of 50 Ω traveling-wave electrodes, and excellent microwave-lightwave velocity match. Polymer Mach–Zehnder modulators with bandwidths of over 40 GHz, and drive voltages of about 10 V, have been reported [27]. The optical loss in polymer waveguides is typically ~3 dB/cm and the total, fiber-to-fiber loss is about 10–12 dB. The intense research in the field is continuously improving the properties of electro-optic polymers. One of the major challenges that the technology has to overcome is the instability of the electro-optic chromophores. If the optical power is large enough (~10 mW), the chromophores become excited and misaligned, diminishing the macroscopic electro-optic effect. For example, a 30 % decrease in the electro-optic efficiency has been estimated after a 10^4 h operation for a device with a 10 μm^2 optical waveguide cross-sectional area and 10 mW of light power at 1320 nm [27]. The misalignment of the chromophores can also be induced by high-electric-field or thermal excitation. Further improvements to the stability of electro-optic polymers and to room-temperature deposition techniques may make electro-optic polymer modulators into a very desirable technology.

GaAs Mach–Zehnder electro-optic modulators have benefited immensely from the growth and fabrication processes that have been developed for telecommunication lasers

and photodetectors. Being a GaAs technology, they can, potentially, be monolithically integrated with lasers, photodetectors, and other GaAs-based devices. Many devices can be obtained from a 6" GaAs wafer, and their waveguide facets are easily cleaved ($LiNbO_3$ waveguides must be polished). Their typical chip length of ~3 cm is smaller than that of $LiNbO_3$ Mach–Zehnder devices, which is ~5 cm [10]. They can also handle large optical powers and their optical waveguide loss is ~1dB/cm, and the total, fiber-to-fiber loss is about 10–15 dB [27]. The GaAs dielectric properties provide for good microwave electrodes, and 40 Gbps devices with drive voltages of about 5 V are commercially available [10].

GaAs polarization converters also benefit from a mature GaAs growth and fabrication process, inheriting many properties that are similar to those of GaAs Mach–Zehnder modulators. Versawave Technology Inc. (formerly JGKB Photonics Inc.) has been a leader in developing ultrahigh-speed mode-conversion modulators [33]. Although still a young technology, Versawave's mode converters exhibit remarkable properties when packaged as intensity polarization modulators as well as polarization modulators. Versawave's mode converter, being a push-pull device, inherently has low chirp (±0.1) when packaged as an intensity modulator [34]. It also has the benefit that the chirp can be adjusted simply by rotating the input polarizer and/or the analyzer. Its package size (2–2.5 inches long) is the shortest of all the available linear electro-optic modulators [33]. Compared to GaAs Mach–Zehnder modulators, the mode converter is single-optical-

waveguide device and does not suffer from additional optical losses due to the Y-splitters. Fiber-to-fiber optical loss is less than 7 dB. Having a bandwidth of ~33 GHz and drive voltage of 3.5–4 V, the device has a great potential for future 40 Gbps optical networks [33], [34].

When packaged as a polarization modulator, a mode converter has very similar properties to the intensity modulator [35]. Due to its low birefringence, it has very low differential group delay (10s of 10^{-15}s), which is much smaller than that for y-propagating $LiNbO_3$ polarization modulators [25], as mentioned in the section on $LiNbO_3$ modulators. Ever since it was introduced, Versawave's polarization modulator has attracted considerable attention for being a fast device, with many desirable properties, which enable an ever-increasing number of polarization-modulation applications to be used at ultrahigh speeds [5]. As explained in [5], Versawave's polarization modulator was recently used at Bell Laboratories for a 10^{-2} reduction (*i.e.*, 100 times improvement) in uncorrected bit error rate of a WDM transmission using in a novel polarization-alternating scheme. Here, the polarization modulator was used to switch the polarization of alternating pulses in a return-to-zero differential-phase-shift-keyed (RZ-DPSK) data stream in order to reduce nonlinear degradation in a communication system, providing for a record-breaking reach. The same modulator was also used in an experiment at the Naval Research Laboratory, where, in an analog optical link, polarization modulation provided a 35 dB improvement in inter-channel crosstalk compared to amplitude modulation. Also, it has been shown

that high speed polarization modulators can be used for scrambling the polarization of a forward pumped Raman amplifier in order to reduce the effect of the pump's polarization dependent gain on the data.

In conclusion, the outstanding performance of the Versawave's mode converter as an intensity modulator, as well as a polarization modulator, that can be used in an ever-increasing number of applications is very inspiring. If a similar but shorter device could be made, it would enable these important modulation schemes to be used in still faster, future optical networks. For it to be significantly shorter, the device must be based on an effect that is significantly greater than the linear electro-optic effect used in the devices mentioned above. Various quantum well structures have been studied over the years in order to realize large electrorefraction as well as electroabsorption effects in semiconductors, both of which are essential for future electro-optic modulators and related electro-optic devices.

The main focus of the thesis is improving the-state-of-the-art in polarization and intensity modulators. In the thesis, coupled quantum well structures, rather than the more common square quantum well structures, are recognized as the most promising technology to achieve this goal in the foreseeable future. The rest of the Introduction chapter presents insights into the optical processes in square and coupled quantum well structures and their application to electro-optic modulators.

1.4 Multiple Quantum Well Modulators

Multiple quantum well (MQW) modulators are based on an array of identical, uncoupled square quantum wells (SQWs). Typically, 10–20 repetitions of a SQW are placed in the optical waveguide of an MQW modulator in order to enhance the interaction with the optical mode [36], [37]. However, as the SQWs are uncoupled, it is sufficient to focus on the optical processes for only one SQW in order to understand the basic operation of the MQW modulator. Fig. 1.12 illustrates a short-period MQW structure, with only two quantum wells, that has $In_{0.53}Ga_{0.47}As$ wells and $In_{0.52}Al_{0.48}As$ barriers. In the left-hand side quantum well, the lowest energy electron wave function (Ψ_{E1}) and the second lowest energy electron wave function (Ψ_{E2}) are shown in the conduction band and have "L" (for left-hand side) superscripts. Also, the two lowest energy heavy-hole wave functions (Ψ_{HH1} and Ψ_{HH2}) and the two lowest energy light-hole wave functions (Ψ_{LH1} and Ψ_{LH2}) are shown in the valence band and have the "L" superscripts. The corresponding wave functions in the right-hand side well have "R" superscripts.

The wave functions in Fig. 1.12 are obtained separately for each well, without a possibility of coupling with the corresponding wave functions in the other well, *i.e.*, assuming that the two wells are infinitely spaced. When the SQWs are brought together, as long as they remain sufficiently far apart, the coupling between the wave functions, *i.e.*, their overlap integrals, will remain small. The overlap integral for two 1-dimensional

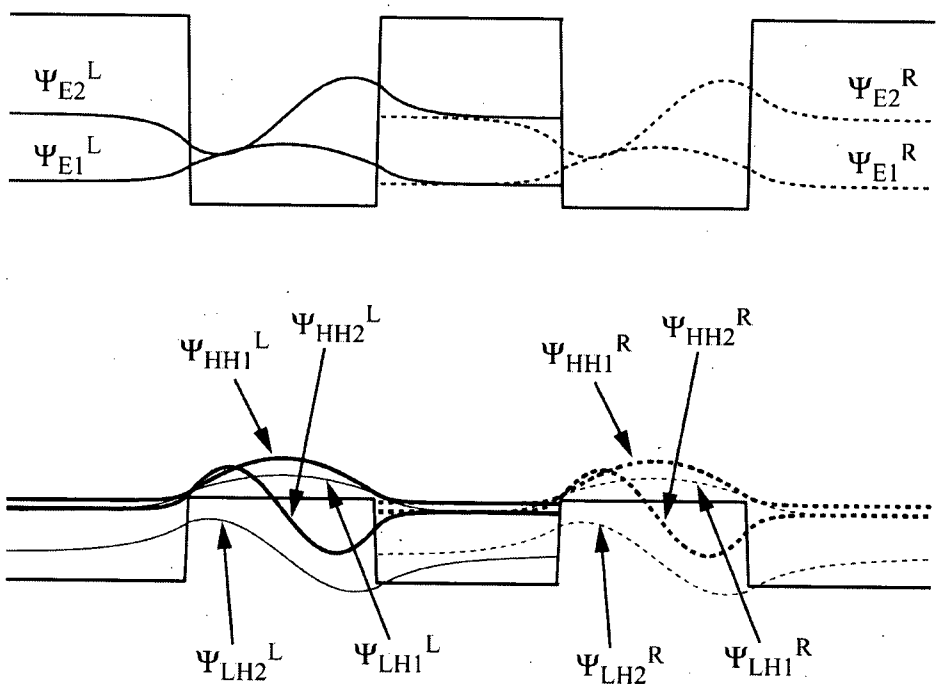

Figure 1.12: An array of two uncoupled SQWs, where, in each well, the two lowest energy electron wave functions (Ψ_{E1} and Ψ_{E2}), heavy-hole wave functions (Ψ_{HH1} and Ψ_{HH2}), and light-hole wave functions (Ψ_{LH1} and Ψ_{LH2}) are shown. The wave functions in the left-hand side well (those with superscript "L") are obtained separately from those in the right-hand side well (those with superscript "R"), *i.e.*, without a possibility of coupling. The quantum wells are $In_{0.53}Ga_{0.47}As$, and the barriers are $In_{0.52}Al_{0.48}As$.

wave functions $f_A(z)$ and $f_B(z)$ is defined as

$$I_{AB} = \int_{-\infty}^{+\infty} f_A(z) f_B(z) dz \,. \tag{1.18}$$

As SQWs are brought together, the high energy wave functions start to couple before the low energy wave functions do. It is clearly shown in Fig. 1.12 that $\Psi_{LH2}{}^{L}$ and $\Psi_{LH2}{}^{R}$ exhibit the deepest penetrations into the middle barrier and, thus, will have the

highest degree of coupling. Consequently, the energies and distributions of the two wave functions will change. However, it is often necessary to keep the barriers as thin as possible in order to increase the number of SQWs in the optical waveguide and increase their interaction with the optical mode. Fortunately, as explained below, it is the lowest energy wave functions (Ψ_{E1}, Ψ_{HH1}, and Ψ_{LH1}), which are more strongly confined to the quantum well layers than the respective second lowest energy wave functions (Ψ_{E2}, Ψ_{HH2}, and Ψ_{LH2}), that dominate the optical processes in MQW modulators, and the barriers are typically as thin as 50 to 100 Å. The characteristic thicknesses for the quantum wells are also typically smaller than 100 Å, depending on the specific application and the MQW modulator design. Also, the choice of material for the quantum wells depends on the specific application and intended wavelength of operation.

1.4.1 Electroabsorption in SQWs

Optical absorption in semiconductor structures of various dimensions (*e.g.*, 1D, 2D, or 3D) strongly depends on the density of states in these structures. This is also true for quantum well structures, which have dimensionality between 2D and 3D [38]. In order for light to excite an electron from a valence-band state into a conduction band state, and become absorbed in the process, it needs to have the energy equal to the energy difference between these two states, assuming that the final state is not already occupied. The energy of light (E) is inversely proportional to its wavelength in vacuum (λ_0), *i.e.*,

$E = h \times c/\lambda_0$, where h is Planck's constant and c is speed of light in vacuum. The two electron states need to be at the same point in space, *i.e.*, they need to have a significant spatial overlap, and, because light adds negligible momentum to the system, they must have the same value for the wave vector k. Such electron transitions are called direct interband transitions. In addition, the ability of light to induce the direct interband transition between these two states depends on its polarization and on the symmetry of the unit cells corresponding to the states [39], which is referred to as the "polarization selection rule."

Fig. 1.13 illustrates how the lowest energy electron wave function (Ψ_{E1}) and either of the lowest energy hole wave functions (Ψ_{HH1} or Ψ_{LH1}) in a SQW react to an electric field applied in the direction normal to the plane of the quantum well [40]. In order to achieve the electroabsorption and the electrorefraction effects that are used in optical modulators, the electric field must be applied in the direction normal to the planes of the quantum well structures regardless whether they are uncoupled SQWs, coupled quantum wells, or some other type of quantum well structure. The effective mass of the heavy holes is much larger than the effective mass of the light holes, and, consequently, the heavy-hole wave functions and the light-hole wave functions have different energies in a quantum well, they experience different degrees of confinement by a quantum well, and they exhibit different degrees of sensitivity to an applied electric field. However, the nature of their

response to an electric field is the same, and the hole wave function in Fig. 1.13 can be used to represent either Ψ_{HH1} or Ψ_{LH1}.

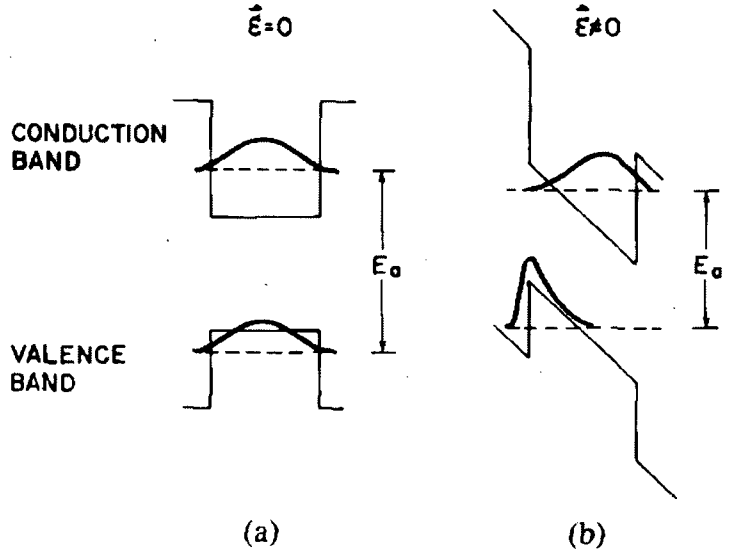

Figure 1.13: Effect of the electric field ($\hat{a}$) on the lowest energy electron wave function, Ψ_{E1}, and on either of the lowest energy hole wave functions, Ψ_{LH1} or Ψ_{HH1}: (a) zero-electric-field case, (b) nonzero-electric-field case [40]. © 1988 IEEE

As shown in Fig. 1.13, upon the application of an electric field, the electron and the hole wave functions will be pulled to opposite sides of the quantum well, where they "see" the lowest potential energies. Their movement to the opposite sides of the quantum well is not surprising considering that electrons and holes have charges of opposite signs. The field, therefore, reduces the overlap integral [Eq. (1.18)] between these two states. In general, when no electric field is applied to a symmetric quantum well, such as those in Figs. 1.12 and 1.13(a), only those electron and hole wave functions corresponding to

states that have the same quantum number will have appreciable overlaps (Ψ_{E1} and Ψ_{HH1}, Ψ_{E1} and Ψ_{LH1}, Ψ_{E2} and Ψ_{HH2}, Ψ_{E2} and Ψ_{LH2}, Ψ_{E3} and Ψ_{HH3}, Ψ_{E3} and Ψ_{LH3}, etc.) [41]. Light-induced transitions between these states are called "allowed" transitions. As the electric field is increased, the nominally "allowed" transitions become less possible and the nominally "forbidden" transitions (Ψ_{E1} and Ψ_{HH2}, Ψ_{E1} and Ψ_{LH2}, etc.) start to dominate. Such behaviour can be easily proved mathematically, using simple geometrical arguments and the orthogonality of wave functions [41].

Fig. 1.13 illustrates another important effect that the electric field has on these states. As shown in the figure, the electric field reduces the energy separation (E_a) between these two states. Conversely, the field increases the corresponding wavelength separation between these two states, and this phenomenon is, therefore, commonly called "red shifting."

Similar to [10], Fig. 1.14 shows a rough sketch of zero-electric-field optical absorption in SQWs corresponding to electron-light-hole transitions. In the literature, optical absorption is represented by the absorption coefficient α (1/cm), which determines the fraction of photons absorbed over a given distance [39]. As mentioned above, the optical absorption is directly related to the density of states. The two steps in Fig. 1.14 are related to the joint density of states [38] for electrons and light holes, assuming that there is no coulombic interaction between them, and assuming that the SQW confines only the two

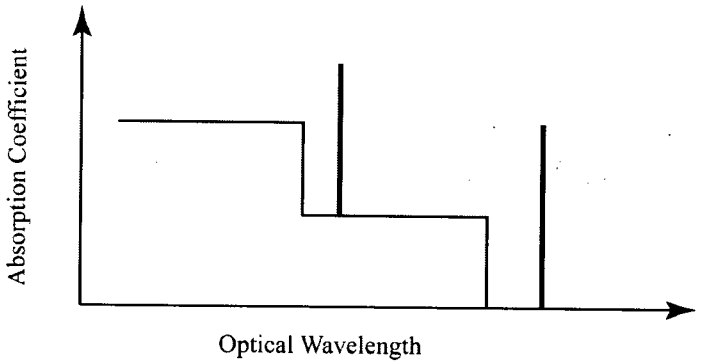

Figure 1.14: Schematic representation of SQW optical absorption for electron-light-hole transitions.

lowest energy electron and the two lowest energy light-hole wave functions. The lower step starts at the wavelength corresponding to the energy separation between Ψ_{E1} and Ψ_{LH1}, and its height is proportional to the overlap integral for these two wave functions. Similarly, the second step starts at the wavelength corresponding to the energy separation between Ψ_{E2} and Ψ_{LH2}, and, also, its height is proportional to the overlap integral for these two wave functions. As explained above, when an electric field is applied to the SQW, the edges of these steps will shift on the horizontal axis and their heights will start diminishing, while the heights of the nominally "forbidden" transitions will start appearing.

In order to fully describe optical absorption in SQWs and explain the origin of the two vertical lines in Fig 1.14, the electron and the light-hole states cannot be treated as independent, and the coulombic attraction between them must be included. As light excites an electron from a state in the valence band into an available state in the

conduction band, an oppositely charged light-hole (or heavy hole) is created in the valence band. The coulombic attraction forces the electron to spend more time in the vicinity of the light hole, and the two-particle system resembles that of the hydrogen atom. The more time the electron spends in the vicinity of the light-hole, the greater the probability of finding the electron and hole in the same unit cell and, thus, the greater the strength of the optical absorption [38]. This two-particle system is called an exciton.

The vertical line sitting at a higher wavelength corresponds to the lowest energy state of the exciton associated with the Ψ_{E1}–Ψ_{LH1} transition (E1–LH1 exciton), while the other line corresponds to the lowest energy state of the exciton associated with the Ψ_{E2}–Ψ_{LH2} transition (E2–LH2 exciton). These states are similar to the lowest energy, radially symmetric 1S states of the 2-dimensional hydrogen atom. In this thesis, for the purpose of modeling electroabsorption and electrorefraction, the relative motion of an electron around a hole in the plane of the quantum well will be restricted to radially symmetric 1S orbitals [42]. The energy separation of the 2D 1S exciton state from the edge of the corresponding free-particle density of states step is called the exciton binding energy (E_B) [42]. In the literature, E_B is given as a negative energy measured relative to the free-particle density of states step, *i.e.*, the energy separation between the electron and hole states when the coulombic coupling is ignored. This is analogous to the 2D hydrogen atom, where the energies of the bound states are negative and those of the unbound states are positive (the same is true for the 3D hydrogen atom). Also, similar to the 2D

hydrogen atom, there are an infinite number of bound exciton states, where the energy separation between the states becomes progressively smaller for high-energy states. However, these states make smaller contributions to the electroabsorption and electrorefraction effects and are commonly neglected in the numerical modeling of these effects [38], [42], again, as is done in this thesis. It is also worth mentioning that the coulombic force enhances the free-particle density of states in the vicinity of the step edge, increasing the absorption coefficient for the corresponding energies. This is also analogous to the unbound positive-energy hydrogen atom states. Therefore, in the following discussions, these states will be referred to as exciton continuum states.

It has already been mentioned above that the electric field pulls electrons and holes in opposite directions and decreases the absorption due to the continuum. This is also true for the excitonic absorption. As an electric field applied in the direction normal to the quantum well separates an electron and a hole in the same direction, the separation between the two particles also increases in the two directions parallel to the plane of the quantum well. The in-plane increase of the exciton occurs because it is energetically favorable for the two-particle system to be nearly spherical. Stretching an exciton into a "pancake" would imply mixing in some highly non-spherical orbitals that have high energies. Conversely, squeezing the exciton by narrowing the quantum well, for example, makes it smaller in all three dimensions. Therefore, the electric field will separate the electron and hole in an exciton and decrease the time they spend in the vicinity of one

another, dramatically decreasing their probability of being in the same unit cell and, in turn, decreasing the excitonic absorption coefficient. As the in-plane motion of an electron around a hole is assumed to be restricted to the radially symmetric 1S orbital, the application of an electric field implies an increase of the orbital's radius and a decrease of E_B, which is small compared to the "red shift" of the absorption edge. It is interesting to note that excitons also contribute to the absorption in bulk, 3D semiconductors, however, the contribution is much smaller because the exciton in the bulk material is considerably larger. Also, the potential confinement due to the quantum well prevents the quantum well excitons from being easily destroyed by the electric field, and the excitonic absorption features can be observed at electric fields higher than 100 kV/cm, which is a very useful effect for quantum well optical modulators.

Fig. 1.15 shows the effect that the electric field has on the absorption spectra for a MQW modulator containing only two 94 Å wide GaAs–AlGaAs SQWs for the polarization of light that is parallel to the planes of the quantum wells (TE polarization) and for the polarization of light that is normal to the planes of the quantum wells (TM polarization) [43]. According to the polarization selection rules for interband transitions in III–V semiconductors [39], only the light holes contribute to the absorption of TM polarization (*i.e.*, there is no heavy-hole contribution), and the basic features of the absorption spectra in Fig. 1.15(b) are similar to those of the absorption spectrum in Fig. 1.14. However, Fig. 1.15(b) shows realistic, experimental absorption spectra where the contributions of the

discrete 1S exciton state and the continuum exciton states are not separate functions (delta function and step-like function, respectively), but rather, they form smooth, continuous curves that arise due to several broadening mechanisms.

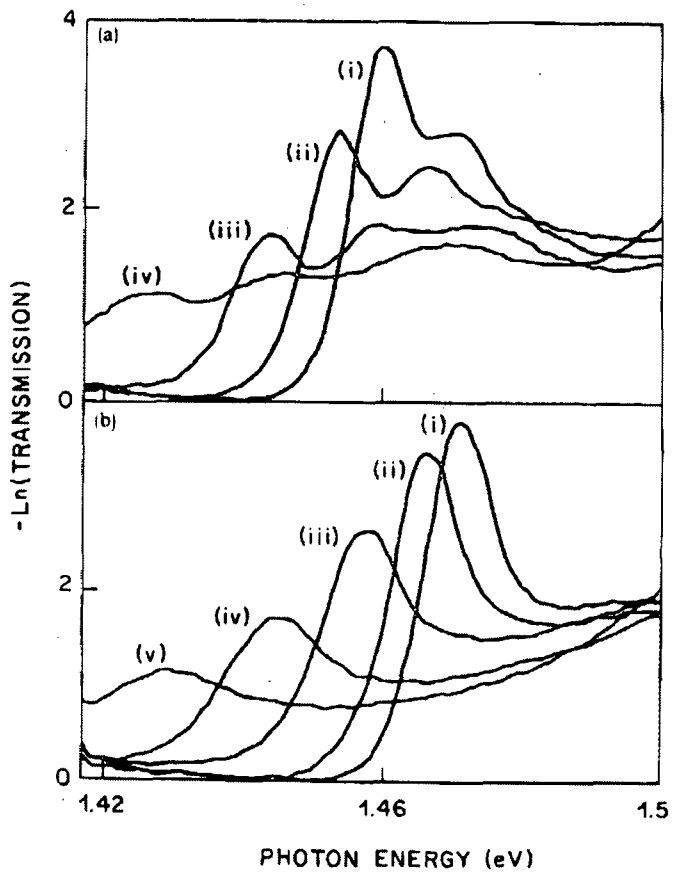

Figure 1.15: Experimental absorption spectra of a waveguide modulator containing only 2 GaAs–AlGaAs SQWs (94 Å wide wells) for: (a) TE polarization and (b) TM polarization. The curves (i)–(v) correspond to electric fields of 16, 100, 130, 180, and 220 kV/cm [43].

As will be explained below, the lowest energy transitions dominate in the absorption processes for MQWs, and only the exciton and the beginning of the continuum states

corresponding to the lowest energy Ψ_{E1}–Ψ_{LH1} transition are shown in Fig. 1.15(b). The linewidth function for the broadening evident in the figure is usually well described by a Lorentzian function (for homogeneous broadening mechanisms), a Gaussian function (for inhomogeneous broadening mechanisms), or a convolution of the two (for simultaneous homogeneous and inhomogeneous broadening mechanisms). The energy width of an absorption peak reflects the resonant state of the corresponding exciton. By the uncertainty principle, the longer the lifetime of the exciton, the better defined the energy, and consequently, the corresponding absorption peak will be sharper. The absorption peak will be broadened (or the exciton lifetime will be shortened) by the following five major mechanisms. First, optical phonon scattering efficiently separates an electron from the corresponding hole (homogeneous broadening). Second, the external electric field will pull the electron and hole in opposite directions (homogeneous broadening). This effect is clearly shown in Fig. 1.15 (b). Third, in MQW modulators, any variations in the sizes of the quantum wells will contribute to the total absorption peak broadening, as each distinct quantum well will have its absorption peak at a distinct energy (inhomogeneous broadening). Fourth, if the electric-field varies across the region containing the quantum wells, each quantum well will have a slightly different response (inhomogeneous broadening). Fifth, particles have finite probabilities of tunnelling out of quantum wells, which means that many states close in energy to each bound state are possible (homogeneous broadening).

Considering the points made above, it is simple to understand the basic principle behind electroabsorption modulators. The wavelength of operation is chosen so that the corresponding energy is ~20–30 meV below the lowest energy exciton, and the electric field F is switched from a low value of $F \approx 0$ kV/cm to $F \approx 100$ kV/cm. Comparing the curve (i) in Fig. 1.15(b) to, for example, the curve (iv), it is clear that the absorption of TM-polarized light increases from a small value (the "on" state of the electroabsorption modulator) to a much larger value (the "off" state of the electroabsorption modulator). Large "red shifting" of the lowest energy exciton and its persistence for large fields needed to achieve the "red shift," provide for large extinction ratios in electroabsorption modulators. This phenomenon is called the Quantum-Confined Stark Effect (QCSE) [44]. Most common electroabsorption modulators, however, modulate the TE light. The polarization selection rules [39], state that both the heavy holes and the light holes participate in electroabsorption for the TE polarization, where the contribution of the heavy holes dominates. Fig. 1.15(a) illustrates electroabsorption for TE polarization, which is very similar to that for TM polarization except that the lowest energy exciton peak corresponds to the $\Psi_{E1}-\Psi_{HH1}$ transition and the second lowest peak corresponds to the $\Psi_{E1}-\Psi_{LH1}$ transition. The light holes have smaller effective masses than the heavy holes, so that the $\Psi_{E1}-\Psi_{LH1}$ energy separation is greater than the $\Psi_{E1}-\Psi_{HH1}$ energy separation.

1.4.2 Electrorefraction in SQWs

Beside the possibility of quite efficient modulation of the optical absorption in SQWs, the refractive indices for the TE and TM polarizations in SQWs also depend on the applied electric field and can be efficiently modulated. The real and imaginary parts of a linear, passive system's response function are related, and, therefore, the same is also true for the complex refractive index response function, $n + jk$. The absorption coefficient is related to the imaginary part of the complex refractive index by

$$\alpha = \frac{2\omega}{c} k , \tag{1.19}$$

and where ω and c are the radian frequency and speed of light, respectively. The radian frequency of light is of course related to its energy by a simple formula $E = \hbar\omega$, where $\hbar = h/2\pi$ is the reduced Planck's constant. The refractive index at frequency ω is a weighted integral of absorption coefficients for all frequencies except for ω, and it can be obtained from the Kramers–Krönig relation [44]

$$n(\omega) - 1 = \frac{c}{\pi} P \int_0^{\infty} \frac{\alpha(\Omega) d\Omega}{\Omega^2 - \omega^2} . \tag{1.20}$$

Here, the symbol P stands for the Cauchy principal value of the integral [10]

$$P \int_0^{\infty} \equiv \lim_{\delta \to 0} \left[\int_0^{\omega-\delta} + \int_{\omega+\delta}^{\infty} \right] . \tag{1.21}$$

The Kramers–Krönig relation thus states that electroabsorption is always accompanied by electrorefraction. However, using the Kramers–Krönig relation in the form given in Eq. (1.20) is impractical because the equation requires a knowledge of the absorption coefficients for all frequencies of light. Fortunately, the spectrum of the electric-field-induced change of the absorption coefficient in SQWs is well localized around the frequencies corresponding to the lowest energy transitions. Consequently, it is possible to calculate the magnitude of the electrorefraction close to the lowest energy transitions using the following equation [44]

$$\Delta n(\omega) = \frac{c}{\pi} P \int_{\omega 1}^{\omega 2} \frac{\Delta\alpha(\Omega) d\Omega}{\Omega^2 - \omega^2}, \tag{1.22}$$

where $\omega 1$ and $\omega 2$ are the lower and upper frequency limits confining the localized change of the absorption coefficient.

Fig. 1.16 illustrates the application of the Kramers–Krönig relation, given in Eq. (1.22), for calculating the refractive index change spectra (Δn) from the simulated absorption coefficient change spectra ($\Delta\alpha$) in a GaAs–AlGaAs SQW for TE polarization around 850 nm [45]. Here, the electric field is switched from 0 to 25 kV/cm, and the figure clearly shows a positive change in $\Delta\alpha$ for wavelengths longer than the wavelength corresponding to the Ψ_{E1}–Ψ_{HH1} transition (labeled as ehh11 in the figure). The electroabsorption is similar to that in Fig. 1.15 (a). Fig. 1.16 shows that Δn reaches a maximum or a minimum close to the wavelength where $\Delta\alpha$ changes sign, and vice versa.

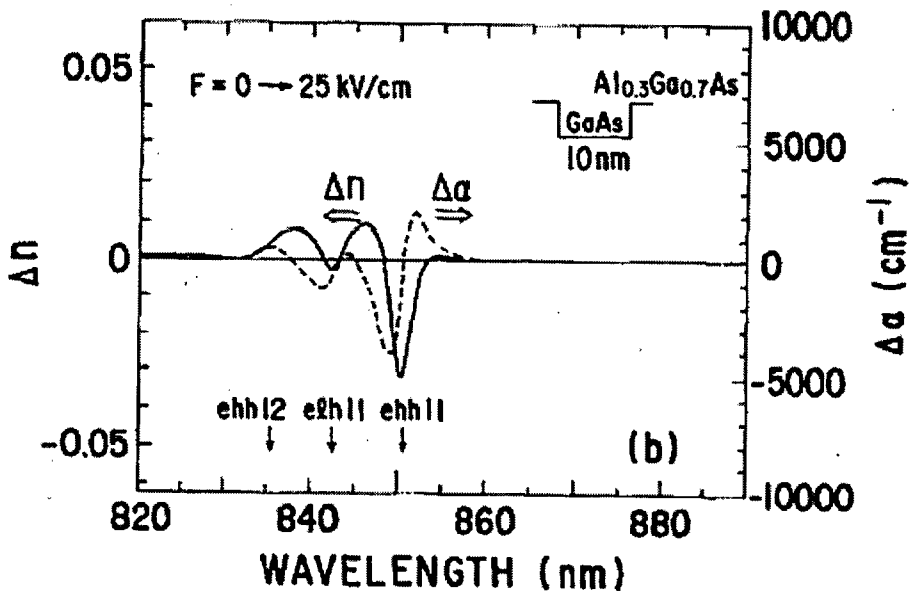

Figure 1.16: Simulated TE absorption change ($\Delta\alpha$) and refractive index change (Δn) in a GaAs–AlGaAs SQW for a field change from 0 to 25kV/cm [45].

This behavior is expected because $\Delta\alpha$ and Δn are actually a Hilbert-transform pair [46]. For the wavelengths just above the Ψ_{E1}–Ψ_{HH1} transition, it is clear that there is a nonzero change in the refractive index. The refractive index change is quite large, and it causes electroabsorption modulators to have significant chirp [10]. Although not clearly visible in Fig. 1.16, $\Delta\alpha$ decreases exponentially for energies below the lowest energy exciton peak, changing much more rapidly than Δn, which exhibits approximately a quadratic decrease for these energies [44]. Therefore, if the amount of detuning from the exciton peak is ~60–80 meV, rather than ~20–30 meV that is typical for electroabsorption modulators, Δn will still be appreciable although $\Delta\alpha$ and α will be small. This is the basic idea behind the use of SQWs for electrorefraction modulators.

1.4.3 Electroabsorption vs. Electrorefraction MQW Modulators

For electrorefraction (ER) MQW modulators, SQWs are commonly placed in the waveguide of a Mach–Zehnder interferometer in order to convert the refractive index modulation into intensity modulation. This is different from electroabsorption (EA) modulators, where the intensity of light is modulated in a single, straight waveguide by simply modulating the absorption coefficient in the MQW region. TE light is typically modulated in both ER and EA modulators. Also, both ER and EA modulators are typically implemented in a p-i-n diode configuration, as shown in Fig. 1.17. The p-i-n diode configuration is used for providing an electric field that is

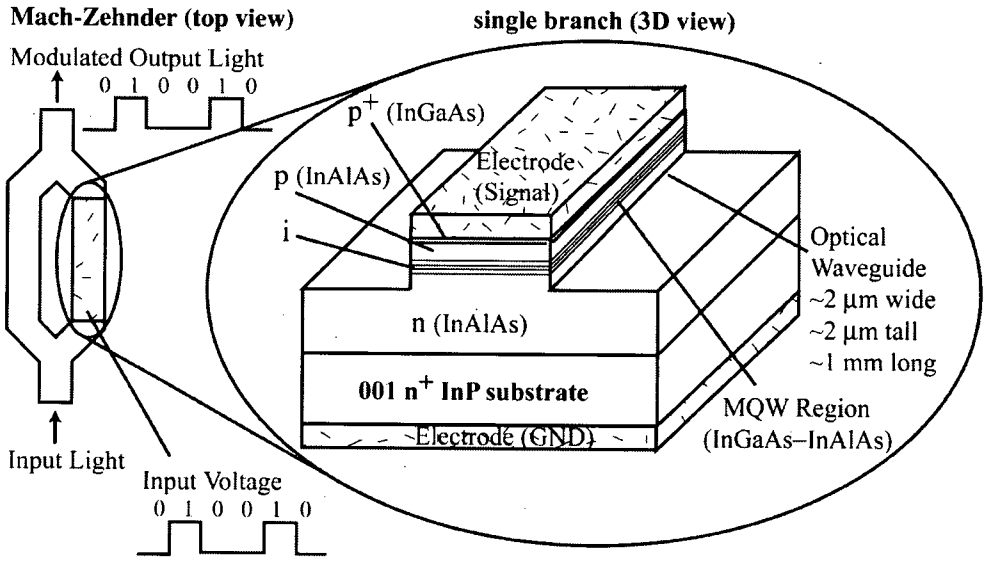

Figure 1.17: InGaAs–InAlAs p-i-n diode Mach–Zehnder modulator.

normal to the planes of quantum wells, and for increasing the overlap between the electric field and the thin (<0.5 μm) MQW region. The average refractive index of the MQW region is higher than that of the surrounding semiconductor for either polarization and provides for confinement of light in the vertical direction. However, although it can be quite short, the p-i-n diode structure is not inherently fast, and there has been considerable research dedicated to designing fast MQW modulators to fully realize their potential for high-frequency operation [47], [48].

One of the most attractive properties of EA MQW modulators is their small size. They are typically 80–300 μm long [10]. Such a small size provides for high yields per wafer, and, therefore, a low cost of fabrication. Similar to ER MQW modulators, the choice of the substrate and the material for the quantum well structures greatly affects the wavelength of operation of these devices. The large band gap in GaAs constrains GaAs / $Al_xGa_{1-x}As$ quantum well structures on GaAs substrates to be used at wavelengths close to 850 nm. Quantum well structures on InP substrates are used at telecommunication wavelengths. There are two main material technologies grown on InP. These are the $In_{1-x1}Ga_{x1}As_{y1}P_{1-y1}$ / $In_{1-x2}Ga_{x2}As_{y2}P_{1-y2}$ and $In_{x1}Ga_{y1}Al_{1-x1-y1}As$ / $In_{x2}Ga_{y2}Al_{1-x2-y2}As$ material systems. The first material technology typically consists of $In_{0.53}Ga_{0.47}As$ (x1 = 0.47 and y1 = 1) quantum wells lattice-matched to InP (x2 = 0 and y2 = 0) barriers and InP substrate. The second material technology typically consists of $In_{0.53}Ga_{0.47}As$ (x1 = 0.53 and y1 = 0.47) quantum wells lattice-matched to $In_{0.52}Al_{0.48}As$ (x2 = 0.52 and

y2 = 0) barriers and, also, to the InP substrate. The composition of the material used for the quantum wells and barriers is chosen depending on the desired potential energies for these layers, which, in turn, determine the energies of the bound states and the wavelength of operation. As will be shown in more detail below, the compositions of the epitaxial layers can also be chosen to introduce strain in the quantum well structures and to manipulate the relative magnitude of the TE and TM polarization responses. Tensile strain has been used in many EA modulators in order to make them polarization-insensitive [10]. The $In_{x1}Ga_{y1}Al_{1-x1-y1}As$ / $In_{x2}Ga_{y2}Al_{1-x2-y2}As$ material system has proven to be very beneficial for EA modulators because it has a very small valence band discontinuity ratio. The valence band discontinuity ratio is defined as the ratio of the band-edge discontinuity for the valence band (ΔE_v) to the band-edge discontinuity for the conduction band (ΔE_c), *i.e.*, ΔE_v / ΔE_c. For the $In_{x1}Ga_{y1}Al_{1-x1-y1}As$ / $In_{x2}Ga_{y2}Al_{1-x2-y2}As$ material system, ΔE_v / $\Delta E_c \approx 30/70$ %, which is considerably smaller than the valence band discontinuity ratio for the $In_{1-x1}Ga_{x1}As_{y1}P_{1-y1}$ / $In_{1-x2}Ga_{x2}As_{y2}P_{1-y2}$ material system (ΔE_v / $\Delta E_c \approx 60/40$ %) [49], [50]. Consequently, due to the small valence band discontinuity ratio, the quantum wells in the valence band are quite shallow and give the heavy holes a good chance of tunneling out of the MQW structure. Due to their large effective masses, the heavy holes tend to be very strongly confined to the quantum wells, and their accumulation due to high input optical powers screens the applied electric field and saturates the electroabsorption effect. Typically, the maximum input optical power

that can be launched into the waveguide of a MQW EA modulator is between 10 and 20 mW [10].

The large absorption in the "off" state of EA modulators also creates considerable current, which is detrimental to the operation of the high-frequency electrodes. Still, 40 Gbps devices with drive voltages lower than 3 V have been demonstrated [27]. Of all the modulator technologies, EA modulators for 40 Gbps links have the lowest drive voltages. However, for long-haul applications, EA modulators are not the strongest candidates because they have the largest chirp. The chirp parameter, α_H, for EA modulators can be greater than 2 [10]. Although, the EA modulators have large inherent optical losses in the "on" state (15–20 dB/mm) [27], they are very short devices and their total fiber-to-fiber loss can be made lower than 10 dB (typically between 6 and 8 dB) using additional optics to match the small, highly elliptical mode of the EA modulator to the large, round mode of standard single-mode fiber [51]. On the other hand, the large inherent optical loss prevents the length of the EA modulator from being significantly increased for an efficient use of traveling-wave electrodes, and EA modulators have largely been used in lumped-electrode configurations. Also, for the traveling-wave electrode configurations, EA modulators tend to have low impedances (20–30 Ω). Of course, being very short, they do not suffer from the microwave-lightwave velocity mismatch. The footprint and cost of packaged EA modulators can be further reduced by integrating them with DFB lasers [10]. Lastly, as they are operated very close to the semiconductor band edge, EA

modulators tend to be very sensitive to the temperature and wavelength of operation. Depending on the specific design and optimization of the EA modulator, its properties can change significantly across the C-band [27], [51], [52]. This is unlike the mode converter, as well as other linear electro-optic modulators, which operate very far from the band edge and have flat wavelength responses over the combined C and L bands [35].

As mentioned above, the wavelength of operation for ER MQW modulators is more detuned from the lowest energy exciton than that for EA MQW modulators. Consequently, they have smaller optical loss in the active region than EA modulators. However, because they require Y-splitters, the ER Mach–Zehnder modulators have considerably larger footprints and tend to have similar or even greater fiber-to-fiber optical loss than EA modulators. For example, the active region of a 10 Gbps lumped-electrode Mach–Zehnder modulator (InGaAsP wells and InP barriers) in [53] is only 600 μm long, whereas its total length including the Y-splitters and tapered-waveguide spot-size converters is 3 mm. The fiber-to-fiber loss for this device is ~6 dB. Having smaller absorption in the active region than the EA MQW modulators, ER MQW modulators have larger optical saturation powers. Similar to other Mach–Zehnder modulators, ER MQW modulators can be driven differentially and have small and adjustable chirp. Also, the imbalance between the two arms typically restricts their extinction ratio to about 15 dB (for a drive voltage of ~4V) [53], whereas ~20 dB extinction ratio is not typical for EA modulators [27]. As ER modulators absorb much less optical power than EA

modulators, they exhibit lower temperature sensitivity due to heating effects. The optically generated currents, therefore, interfere less with the operation of fast electrodes [27].

Although the development of high-frequency electrodes for EA and ER modulators is an active area of research, modern ER MQW modulators are mostly lumped-electrode p-i-n devices limited to 10 Gbps applications [10]. Recently, in an on-wafer experiment, an ER MQW modulator having travelling-wave p-i-n electrodes and a modulation bandwidth of 28 GHz has been demonstrated [54]. The drive voltage of this device was about 3 V, and its extinction ratio and fiber-to-fiber loss were >14 dB and ~9 dB, respectively. Also, recent modelling of ER MQW modulators having travelling-wave p-i-n electrodes has shown that modulation bandwidths exceeding 40 GHz could be achieved, although the drive voltages would be larger than 4 V and additional optical loss due to the electrode configuration would be inevitable [48]. The p-doped region in p-i-n devices introduces significant optical loss and microwave loss. The microwave loss is the main bandwidth-limiting factor of these p-i-n devices. The bandwidth could be improved with better electrode designs, which require larger thicknesses of the intrinsic regions containing the quantum wells and, therefore, provide lower electric fields to the quantum wells. These devices are likely to have Schottky-contact coplanar or microstrip electrodes [55], [56], [57]. Therefore, improving the ER effect of quantum well structures is an important requirement for future ER modulators. ER modulators based on coupled quantum wells,

rather than SQWs, are capable of providing this important benefit. The remainder of this thesis is dedicated to provide a background for the operation of coupled quantum well modulators (Section 1.5) and to provide the convincing arguments that the coupled quantum well modulators developed in this thesis will play an important role in future optical links (Chapters 2–7).

1.5 Coupled Quantum Well Structures

Coupled quantum well (CQW) structures consist of multiple quantum wells that are separated by thin barriers, which permit strong coupling between the states of the wells. In this thesis, we will be looking at CQW structures containing only two quantum wells separated by a thin barrier. The coupling creates new states, and these states exhibit electric-field dependences that are qualitatively different from those of the states in SQWs. CQW structures offer refractive index changes that have similar magnitudes to those typically obtainable in SQWs. The magnitude of the electric-field-induced refractive index change in SQWs is $\Delta n \approx 10^{-3}$ for 100 kV/cm change in the electric field [58]. In CQW structures, however, similar changes in the refractive index can be obtained for ~20 kV/cm change in the electric field, which is a significant improvement. Unlike in SQWs, in CQW structures, the electroabsorption is based on the modulation of the absorption strength associated with the exciton peaks, rather than on their "red shifting." As CQW structures are the main focus of this thesis, the electroabsorption and

electrorefraction in these structures will be discussed in detail. However, a brief description of the numerical models used to simulate electroabsorption and electrorefraction in these structures will be given first.

1.5.1 Modeling of CQW Structures

In this section, the model used for simulating electroabsorption and electrorefraction in the CQW structures studied in the thesis is described. This model is commonly used for simulation of CQW structures as well as SQWs [38], [42], [60]. In the model, the exction equation is used within the effective-mass, envelope-function approximation, and it is solved using the variational method. The effective mass exciton equation can be written as

$$\left(H_e - H_h + E_g - \frac{e^2}{4\pi\varepsilon_s|\vec{r}_e - \vec{r}_h|}\right)\Phi(\vec{r}_e,\vec{r}_h) = E\,\Phi(\vec{r}_e,\vec{r}_h), \tag{1.23}$$

where

$$H_e = -\frac{\hbar^2}{2m_e^*}\vec{\nabla}_e^2 + V_e(z_e) \tag{1.24}$$

and

$$-H_h = -\frac{\hbar^2}{2m_h^*}\vec{\nabla}_h^2 + V_h(z_h) \tag{1.25}$$

are the electron Hamiltonian and the hole Hamiltonian, respectively. Here, m_e^* and m_h^* are the effective masses for electrons and either light or heavy holes. It is assumed that the electric field is applied in the z direction and its effect is included in the potential energy for both electrons and holes (V_e and V_h, respectively). The third term on the left-hand side of Eq. (1.23) is the band gap energy, and the fourth term is the Coulomb potential energy, where e is the elementary charge, and ε_s is the permittivity of the quantum well material. The coulombic interaction in the above equation couples the electron and hole coordinates ($\vec{r}_e$ and $\vec{r}_h$, respectively) in all three dimensions. If it were not for this coupling, the two-particle wave function in Eq. (1.23) would be a simple product of the electron and hole wave functions and the equation would be separable. Neglecting the quantum well potential (V_e and V_h) in Eq. (1.23) would reduce it to the well-known hydrogen atom equation [61]. Similar to the hydrogen atom problem, Eq. (1.23) is more easily solved when recast in the center-of-mass coordinates in the plane of the quantum wells

$$\vec{R}_t = X\hat{x} + Y\hat{y} = \frac{m_e^*\vec{\rho}_e + m_h^*\vec{\rho}_h}{M} \tag{1.26}$$

and the difference coordinates in the plane of the quantum wells

$$\vec{\rho} = x\hat{x} + y\hat{y} = \vec{\rho}_e - \vec{\rho}_h, \tag{1.27}$$

where

$$M = m_e^* + m_h^* \tag{1.28}$$

is the total mass corresponding the electron-hole system. Performing the transformation, and defining the reduced mass of the electron-hole system as

$$\frac{1}{m_r} = \frac{1}{m_e^*} + \frac{1}{m_h^*}, \tag{1.29}$$

make Eq. (1.23) become

$$\left[-\frac{\hbar^2}{2M}\vec{\nabla}^2_{\vec{R}_t} - \frac{\hbar^2}{2m_r}\vec{\nabla}^2_{\vec{\rho}} + H(z_e) - H(z_h) - \frac{e^2}{4\pi\varepsilon_s|\vec{r}_e - \vec{r}_h|} - (E - E_g) \right] \Phi(\vec{r}_e, \vec{r}_h) = 0, \tag{1.30}$$

where

$$H(z_e) = -\frac{\hbar^2}{2m_e^*}\frac{\mathrm{d}^2}{\mathrm{d}z_e^2} + V_e(z_e) \tag{1.31}$$

and

$$-H(z_e) = -\frac{\hbar^2}{2m_h^*}\frac{\mathrm{d}^2}{\mathrm{d}z_h^2} + V_h(z_h) \tag{1.32}$$

are the usual 1-dimensional electron Hamiltonian and the 1-dimensional hole Hamiltonian, respectively, from which the energies and 1-dimensional wave functions are readily obtained by solving

$$H(z_e)\, f_n(z_e) = E_{en}\, f_n(z_e) \tag{1.33}$$

and

$$H(z_h)\, g_m(z_h) = E_{hm}\, g_m(z_h), \tag{1.34}$$

using the transfer matrix method [62].

The first term in Eq. (1.30) is the only term describing the center of mass of the system, which can be regarded as a freely moving particle of mass M and momentum

$$\vec{K}_t = \vec{k}_{et} + \vec{k}_{ht}, \tag{1.35}$$

which is negligible for direct interband transitions. The wave function can, therefore, be written as

$$\Phi(\vec{r}_e, \vec{r}_h) = \frac{e^{i(\vec{K}_t = 0)\vec{R}_t}}{\sqrt{A}} F(\vec{\rho}, z_e, z_h). \tag{1.36}$$

Using the completeness property of the free-electron and free-hole wave functions, the exciton envelope function can be written as

$$F(\vec{\rho}, z_e, z_h) = \sum_n \sum_m \phi_{nm}(\vec{\rho})\, f_n(z_e)\, g_m(z_h). \tag{1.37}$$

After some further manipulations of the equation, it can be shown that it satisfies

$$H_B \phi_{nm}(\vec{\rho}) = E_B \phi_{nm}(\vec{\rho}), \tag{1.38}$$

where

$$H_B = \left(-\frac{\hbar^2}{2m_r} \vec{\nabla}^2_{\vec{\rho}} - V_{nm}(\rho) \right) \tag{1.39}$$

and

$$V_{nm}(\rho) = \int dz_e \left| f_n(z_e) \right|^2 \int dz_h \left| g_m(z_h) \right|^2 \frac{e^2}{4\pi\varepsilon_s \sqrt{\rho^2 + \left| z_e - z_h \right|^2}}. \tag{1.40}$$

Eq. (1.40) is a simpler version of a more general equation [38] and does not allow distinct subbands in the conduction band and distinct subbands in the valence band to be coupled by the coulombic interaction. In Eq. (1.38),

$$E_B = E - \left(E_g + E_{en} - E_{hm} \right) \tag{1.41}$$

is the exciton binding energy, which is the negative quantity that was already mentioned in the discussion of electroabsorption in SQWs.

In order to obtain E_B and the wave function from Eq. (1.38), an additional approximation is made. It is assumed that the relative motion of an electron around a hole in the plane of the quantum well is restricted to the lowest energy 1S orbital, which is a reasonable assumption considering that the higher energy states make smaller contributions to the absorption coefficient, as mentioned in the discussion of electroabsorption in SQWs. The 1S state is radially symmetric in the plane of the quantum well structure

$$\phi_{nm}(\bar{\rho}) = \sqrt{\frac{2}{\pi}} \frac{1}{\lambda} e^{-\frac{\rho}{\lambda}}, \tag{1.42}$$

and it has an effective radius λ. This radius is found, and the problem is solved, using the variational method. In this method, the binding energy

$$E_B(\lambda) = \frac{\langle \phi | H_B | \phi \rangle}{\langle \phi | \phi \rangle} \tag{1.43}$$

as a function of the in-plane radius as an adjustable parameter is minimized. The in-plane extension of the exciton is comparable to the length of the quantum well structure in the z direction.

In [38], it is shown how E_B can be analytically obtained from the variational method for a simple case in which no coulombic coupling of distinct subband states is allowed.

However, this minimization procedure needs to be done numerically if the coulombic coupling of distinct subband states is allowed. For example, in CQW structures, the energy separation between the two lowest energy electron wave functions, $f_1(z_e)$ and $f_2(z_e)$, and the energy separation between the two lowest energy hole wave functions, $g_1(z_e)$ and $g_2(z_e)$, can be on the order of E_B (<10 meV). In such a case, the coulombic coupling of these states cannot be neglected, and the variational wave function becomes

$$F(\vec{\rho},z_e,z_h)=\left[af_1(z_e)+\sqrt{1-a^2}f_2(z_e)\right]\left[bg_1(z_h)+\sqrt{1-b^2}g_2(z_h)\right]\sqrt{\frac{2}{\pi}}\frac{1}{\lambda}e^{-\frac{\rho}{\lambda}}, \quad (1.44)$$

as explained in [63]. In this case, λ, a, and b have to be varied independently in order to find E_B for the 1S excitons. As will be shown below, $f_1(z_e)$ and $f_2(z_e)$ or $g_1(z_e)$ and $g_2(z_e)$ are confined to opposite wells of a CQW structure and will switch wells when the applied electric field reaches a certain value, which is called the resonant electric field, F_R. One of the main effects of the coupling is to increase F_R by several kV/cm.

The absorption spectra consist of the discrete and continuum exciton state contributions corresponding to both the electron-heavy-hole transitions and the electron-light-hole transitions [38]. The discrete exciton states contribution to the absorption coefficient is given as

$$\alpha_D(\hbar\omega)=C_0\frac{2}{L_{qw}}\left|\phi_{nm}(\vec{\rho}=0)\right|^2\left|I_{nm}\right|^2\left|\hat{e}\cdot\vec{p}_{cv}\right|^2B(E-\hbar\omega), \quad (1.45)$$

where a transition between an n electron state and an m hole state (light-hole or heavy-hole state) is considered. In CQW structures, it is typically sufficient to consider only the two lowest energy electron, heavy-hole, and light-hole states, and the absorption coefficients corresponding to the transitions between these conduction-band and valence-band states are simply added together. The first term in Eq. (1.45),

$$C_0 = \frac{\pi e^2}{n_r c \varepsilon_0 \omega m_0^2}, \tag{1.46}$$

depends on some of the already defined material parameters and fundamental constants, as well as the refractive index of the quantum well material (n_r), the free-space permittivity (ε_0), and the free electron mass (m_0). The second term in Eq. (1.45) is inversely proportional to L_{qw}, which is the length of one period of the quantum well structure. The third term is the in-plane exciton envelope function of Eq. (1.42) evaluated for zero relative displacement between the electron and the hole, which is proportional to the probability of finding the electron and the hole in the same unit cell. The fourth term is the overlap integral between the 1-dimensional electron and hole wave functions, as defined in Eq. (1.18). The fifth term is determined by the polarization selection rules, given below. The vector $\hat{e}$ is the unit vector describing the polarization of light, and the vector

$$\vec{p}_{cv} = \left\langle u_c \middle| \vec{p} \middle| u_v \right\rangle, \tag{1.47}$$

which is called the momentum matrix element. Here, $\vec{p}$ is the momentum operator and u_c and u_v are the conduction-band and valence-band unit-cell wave functions, respectively. For TE polarization ($\hat{e} = \hat{x}$ or $\hat{e} = \hat{y}$),

$$\left|\hat{e}\cdot\vec{p}_{cv}\right|^2 = M_b^2\begin{cases}\frac{3}{2} & heavy-hole\ exciton\\ \frac{1}{2} & light-hole\ exciton\end{cases}, \tag{1.48}$$

and for TM polarization ($\hat{e} = \hat{z}$),

$$\left|\hat{e}\cdot\vec{p}_{cv}\right|^2 = M_b^2\begin{cases}0 & heavy-hole\ exciton\\ 2 & light-hole\ exciton\end{cases}, \tag{1.49}$$

where

$$M_b^2 \cong \left(\frac{m_0^2 E_g\left(E_g+\Delta\right)}{6m_e^*\left(E_g+2\Delta/3\right)}\right) \tag{1.50}$$

is the bulk matrix element (squared). In Eq. (1.50), Δ is the spin-orbit splitting energy. Eqs. (1.48) and (1.49) state, as was already mentioned, that the electron-heavy-hole transitions do not contribute to absorption for TM polarization, and they dominate the absorption for TE polarization. Finally, the last term in Eq. (1.45) is the exciton broadening function, which is represented by the Lorentzian function

$$B\left(E-\hbar\omega\right)=\frac{\gamma}{\pi\left[\left(E-\hbar\omega\right)^2+\gamma^2\right]} \tag{1.51}$$

for homogeneous broadening mechanisms and by the Gaussian function

$$B\left(E-\hbar\omega\right)=\frac{1}{\sqrt{2\pi}\sigma}e^{-\frac{\left(E-\hbar\omega\right)^2}{2\sigma^2}} \tag{1.52}$$

for inhomogeneous broadening mechanisms [10]. In Eq. (1.51), γ is the half-width-at-half-maximum (HWHM). In Eq. (1.52), the HWHM corresponds to ~1.175σ. In both of these functions E stands for the total exciton energy, as given in Eq. (1.41). In reality, the broadening function is a convolution of the broadening functions corresponding to each of the broadening mechanisms that are relevant in a specific device. In this thesis, a Lorentzian broadening function that has $\gamma \approx 6$ meV is used. The semi-empirical formula used to obtain this value is given in [64]. It is also stated in [64], and confirmed by many simulations in this thesis, that the choice of the broadening function for CQW modulators has no significant effect on the electrorefraction process in these devices.

In the formula for the continuum states contribution to the absorption coefficient

$$\alpha_C(\hbar\omega) = C_0 \frac{m_r}{\pi\hbar^2 L_{qw}} M_b^2 \left|I_{nm}\right|^2 \int_0^\infty \mathrm{d}E_t \, M(E_t) S(E_t) B(E - \hbar\omega), \tag{1.53}$$

some of the terms that appear in Eq. (1.45) can be recognized. However, because the exciton states form a continuum here, Eq. (1.53) is an integral with respect to the transverse energy

$$E_t = \frac{\hbar^2 k_t^2}{2m_r} \tag{1.54}$$

of the electron-hole two-body system. Also, the momentum matrix element in Eq. (1.53) is different from that in Eq. (1.45) because the momentum matrix element in Eq. (1.45) is approximated with $k_t = 0$, which is a commonly used approximation. In Eq. (1.53), the

momentum matrix element in the integral depends on E_t, and for TE polarization becomes

$$M(E_t)=\begin{cases}\frac{3}{4}\left(1+\cos^2\theta_{nm}\right) & heavy-hole\ exciton\\ \frac{1}{4}\left(5-3\cos^2\theta_{nm}\right) & light-hole\ exciton\end{cases}, \tag{1.55}$$

while for TM polarization, it becomes

$$M(E_t)=\begin{cases}0 & heavy-hole\ exciton\\ \frac{1}{2}\left(1+3\cos^2\theta_{nm}\right) & light-hole\ exciton\end{cases}. \tag{1.56}$$

In these two equations,

$$\cos^2\theta_{nm}=\frac{E_{en}+\left|E_{hm}\right|}{E_{en}+\left|E_{hm}\right|+E_t}. \tag{1.57}$$

Also, in Eq. (1.53)

$$S(E_t)=\frac{s_0}{1+e^{-\frac{2\pi}{\sqrt{E_t/R_y}}}}, \tag{1.58}$$

which is the Sommerfeld enhancement factor for a 2D exciton. The Sommerfeld enhancement factor comes from the solution of $\phi_{nm}(\vec{\rho}=0)$ for the continuum states of a 2D exciton. A detailed derivation of the eigenfunctions and eigenenergies of the continuum states, as well as bound states of the 3D and the 2D hydrogen atom, is given in [61]. Typically, $1 \le s_0 \le 2$, and $s_0 = 2$ for a purely 2D exciton. R_y is the Ryberg energy. The total exciton energy for the continuum states in $B(E-\hbar\omega)$ is given as

$$E = E_g + E_{en} - E_{hm} + E_t. \tag{1.59}$$

Once the absorption spectra for either polarization are obtained by adding the discrete and continuum components, the corresponding refractive index changes can be obtained using the Kramers–Krönig relation given in Eq. (1.22). In the following section, the electrorefraction of a particular CQW structure is simulated using this model.

1.5.2 Electrorefraction in CQW Structures

Although the research on CQW structures has not been as intense as the research on SQWs, there has been considerable research effort dedicated to CQW structures in the last two decades. However, a large part of this effort was focused on studying the basic physics and optical phenomena in GaAs–AlGaAs CQW structures, both experimentally and theoretically [63], [65]–[71]. Compared to SQWs, there have been few attempts to develop and optimize devices based on CQW structures for EA and ER modulators, especially for 1550 nm operation. Regarding EA modulators, some of the research that did include specific device considerations, such as chirp, focused on GaAs material systems [72], [73]. A rare example of a 1550 nm CQW EA modulator, that demonstrated an improved effect compared to SQW EA modulators, was presented only recently [74] (in 2004). As regards ER modulators, the CQW structures studied have also been mainly based on GaAs material systems and have demonstrated significant improvements over SQW ER modulators, both theoretically [75] and, recently, experimentally [76], [77] (in

2001 and 2004, respectively). A 50 GHz modulator based on GaAs–AlGaAs quantum well structures studied in [77] has already been demonstrated in [78]. The drive voltage of the device was 3 V, which was unexpectedly large considering the theoretical predictions of a very large electrorefraction effect. Subsequently, it was shown that the electrorefraction effect in these structures is very sensitive to the layer thickness and compositional variations that occur during the growth process [79], making it challenging to realize the large electrorefraction effect predicted by theory. This is true for CQW structures in general, and it is probably the main factor impeding the development of ER, as well as EA, CQW modulators. In general, the CQW structures intended for 1550 nm operation are expected to be even more sensitive to the variations than GaAs-based structures because they contain ternary and/or quaternary epitaxial layers. So far, research on CQW structures in these material systems has only been theoretical [45], [60], [1]–[3], and no fabricated 1550 nm ER CQW modulators have been reported.

As will be shown in the following chapters, the two main objectives of this thesis are the improvement of the robustness to growth of CQW structures for ER as well as EA modulators and the facilitation of polarization modulation using these structures. However, before addressing these two objectives, basics of electrorefraction in CQW structures are presented.

Fig. 1.18 shows the energy-band diagram for an InGaAs–InAlAs CQW structure as well as the two lowest energy electron wave functions (Ψ_{E1} and Ψ_{E2}), the two lowest energy light-hole wave functions (Ψ_{LH1} and Ψ_{LH2}), and the two lowest energy heavy-hole wave functions (Ψ_{HH1} and Ψ_{HH2}) for an electric field, F, of 0, 19, and 35 kV/cm. The CQW structure also confines some other, higher energy wave functions, which are not shown in Fig. 1.18 because they do not make significant contributions to the electrorefraction effect. The CQW structure has $In_{0.53}Ga_{0.47}As$ wells and $In_{0.52}Al_{0.48}As$ barriers, so that all of the epitaxial layers are lattice-matched to (001) InP. The left-hand side well (QW1) is 48 Å thick, and the right-hand side well (QW2) is 54 Å thick. The middle barrier is 36 Å thick, and each of the external barriers is 90 Å thick. For $F = 0$ kV/cm, Ψ_{E1}, Ψ_{HH1}, and Ψ_{LH1} are localized in QW2 because it is thicker than QW1 and provides lower potential energy to these wave functions, as shown in Fig. 1.18(a). QW2 would have the same effect if it was made deeper than QW1. Compared to the other two wave functions, Ψ_{HH1} is the most strongly localized because it has the largest effective mass. The second lowest energy wave functions, *i.e.*, Ψ_{E2}, Ψ_{HH2}, and Ψ_{LH2}, are localized in QW1 for $F = 0$ kV/cm.

When the electric field is increased to about 19 kV/cm, as shown in Fig. 1.18(b), Ψ_{E1} and Ψ_{E2} become approximately equally distributed between the two wells. For this electric field, the energy separation between the two wave functions becomes the smallest, and the electric field is called the resonant electric field for electrons, F_E. When the electric field is increased above F_E, as shown in Fig. 1.18(c), Ψ_{E1} and Ψ_{E2} become strongly

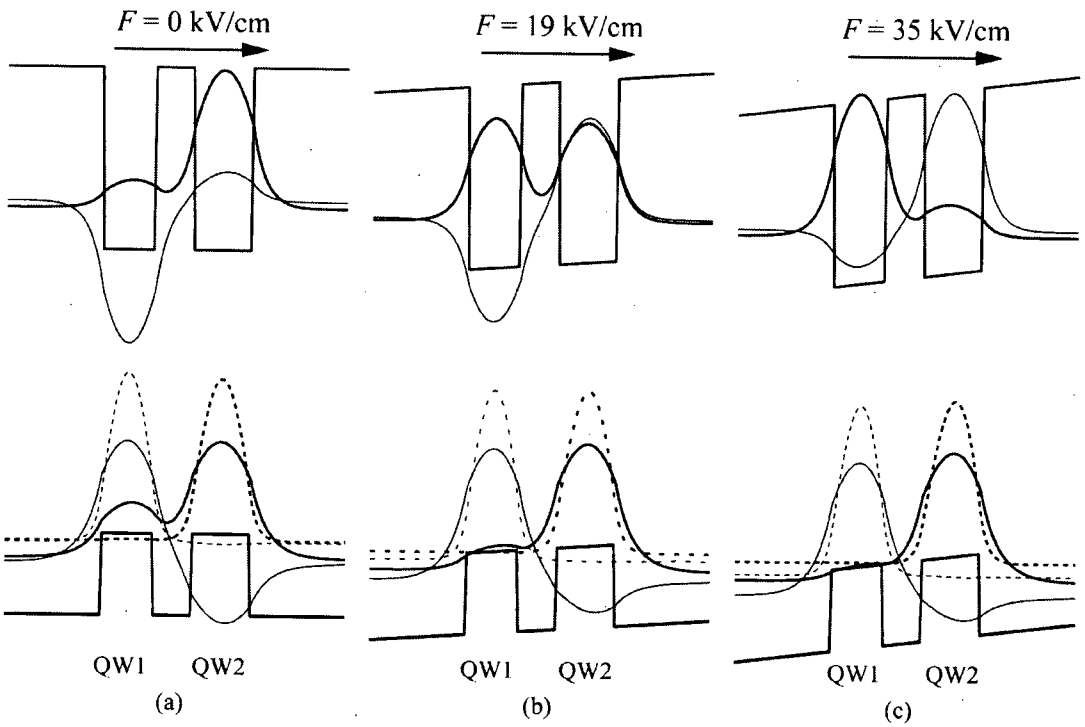

Figure 1.18: Energy-band diagram of a InGaAs–InAlAs CQW structure and Ψ_{E1} and Ψ_{E2}, Ψ_{LH1} and Ψ_{LH2}, Ψ_{HH1} and Ψ_{HH2} for (a) $F = 0$, (b) 19, and (c) 35 kV/cm. Ψ_{E1} and Ψ_{LH1} are shown as full thick lines, while Ψ_{E2} and Ψ_{LH2} are shown as full thin lines. Ψ_{HH1} is shown as dashed thick line, while Ψ_{HH2} is shown as dashed thin line.

localized in QW1 and QW2, respectively. No similar anticrossing of Ψ_{LH1} and Ψ_{LH2} or Ψ_{HH1} and Ψ_{HH2} occurs in Fig. 1.18. These wave functions simply become more strongly localized to their quantum wells as the electric field is increased. These wave functions would anticross if the electric field was applied in the opposite direction, or if QW1 was wider than QW2 and Ψ_{LH1} and Ψ_{HH1} were localized in it for $F = 0$ kV/cm. The electric-field-induced anticrossing of only one type of wave function, *e.g.*, the electron wave functions, without the anticrossing of the other types, *e.g.*, the light-hole and the heavy-

hole wave functions, gives rise to a special electrorefraction effect largely exploited in this thesis.

Figs. 1.19(a) and (b) show the electric-field dependence of the squared overlap integrals between the conduction and valence band wave functions of Fig. 1.18. The overlap integrals are evaluated using Eq. (1.18), and, for example, the curve

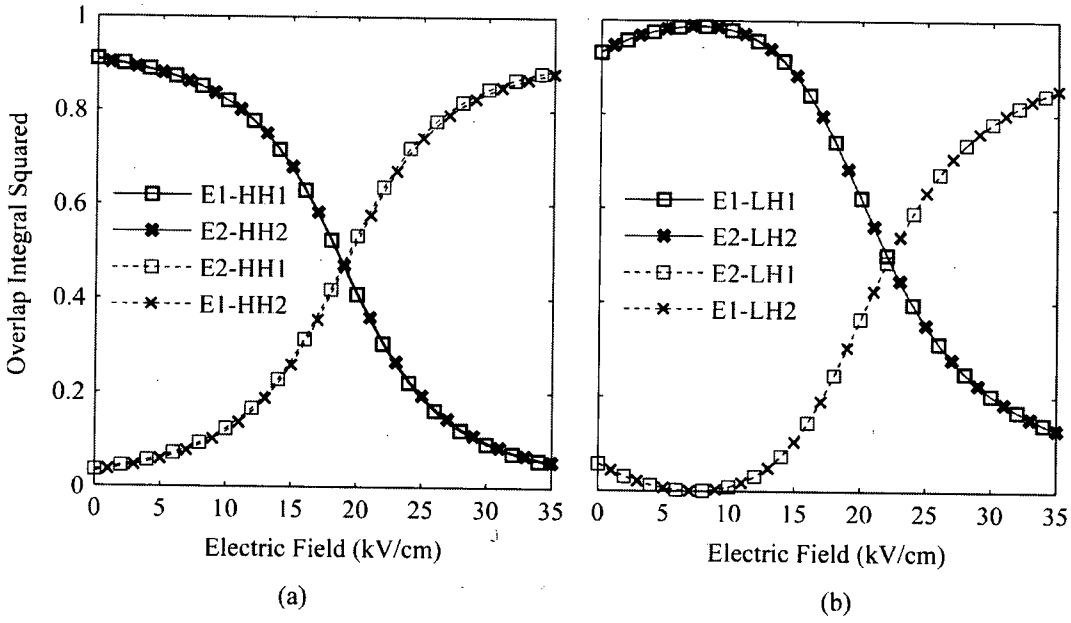

Figure 1.19: Squared overlap integrals of the wave functions corresponding to the transitions (a) between the two lowest energy electron and heavy holes and (b) between the two lowest energy electron and light holes.

corresponding to the overlap integral for the Ψ_{E1}–Ψ_{HH1} transition is labeled as "E1–HH1" in Fig. 1.19(a). In the literature, the transitions between Ψ_{E1} and Ψ_{HH1}, Ψ_{E2} and Ψ_{HH2}, Ψ_{E1} and Ψ_{LH1}, and Ψ_{E2} and Ψ_{LH2} are sometimes referred to as the "symmetric-mode transitions" [80]. Similarly, the transitions between Ψ_{E1} and Ψ_{HH2}, Ψ_{E2} and Ψ_{HH1}, Ψ_{E1}

and Ψ_{LH2}, and Ψ_{E2} and Ψ_{LH1} are sometimes referred to as the "asymmetric-mode transitions."

In Fig. 1.19(a), the squared overlap integrals corresponding to the electron-heavy-hole symmetric-mode transitions decrease with F, while the squared overlap integrals corresponding to the electron-heavy-hole asymmetric-mode transitions increase with F. This behavior results from the electric-field-dependent redistribution of Ψ_{E1} and Ψ_{E2} only, as the distributions of Ψ_{HH1} and Ψ_{HH2} barely depend on F in the region of interest ($0 \leq F \leq 35$ kV/cm). Also, the shapes of the curves in Fig. 1.19(a) suggest that the distributions of Ψ_{E1} and Ψ_{E2} are most sensitive to changes in F when these wave functions are approximately equally distributed between QW1 and QW2, *i.e.*, when $F \approx F_E$. In general, a distribution of any wave function in Fig. 1.18 is most sensitive to both changes in F and relative changes in the thicknesses and compositions of the two wells when the wave function is approximately equally distributed between the two wells, and, conversely, it is least sensitive to these changes when the wave function is strongly confined to one of the wells. Later in this thesis, this phenomenon will be used to design CQW structures which are quite robust to the growth process.

Fig. 19(b) shows that the squared overlap integrals corresponding to the electron-light-hole transitions exhibit similar dependence on F to that of the electron-heavy-hole transitions. However, the squared overlap integrals for the electron-light-hole symmetric-

mode transitions first increase as F is changed from 0 to about 7 kV/cm, and then decrease for higher F. The reason for this behavior is that Ψ_{LH1} and Ψ_{LH2} are less strongly confined to their respective wells than Ψ_{E1} and Ψ_{E2} are [see Fig. 1.18(a)], and it takes a small change in F (again, about 7 kV/cm) to maximize the spatial overlaps between the wave functions for the symmetric-mode transitions before they start decreasing toward very small values. Fig. 19(b) also shows that the opposite is true for the electron-light-hole asymmetric-mode transitions. In addition, the weak confinement of Ψ_{LH1} and Ψ_{LH2} for small F makes the value of F for which the squared overlap integrals of the symmetric-mode and asymmetric-mode transitions are equal be somewhat larger than the one for the electron-heavy-hole transitions in Fig. 19(a).

Besides obtaining the electric-field dependence of the squared overlap integrals associated with the wave functions confined by CQW structures, it is essential to obtain the electric-field dependence of the exciton binding energies associated with these wave functions. This is because the contributions of the discrete exciton states to the absorption spectra [Eq. (1.45)] dominate the electroabsorption and, in turn, electrorefraction in CQW structures, and these contributions strongly depend on both the squared overlap integrals and binding energies associated with the wave functions. In Eq. (1.45), the discrete exciton state absorption spectrum, α_C, is proportional to the probability of an electron in state n and a hole in state m being in the same unit cell in the plane of the quantum well, *i.e.*, $\left|\phi_{nm}(\vec{\rho}=0)\right|^2$, which, in turn, is proportional to the exciton binding energy. Again,

according to Eq. (1.42), the exciton binding energy is inversely proportional to the exciton in-plane radius, λ. Figs. 1.20(a) and (b) show how the binding energies of the heavy-hole and the light-hole excitons depend on F.

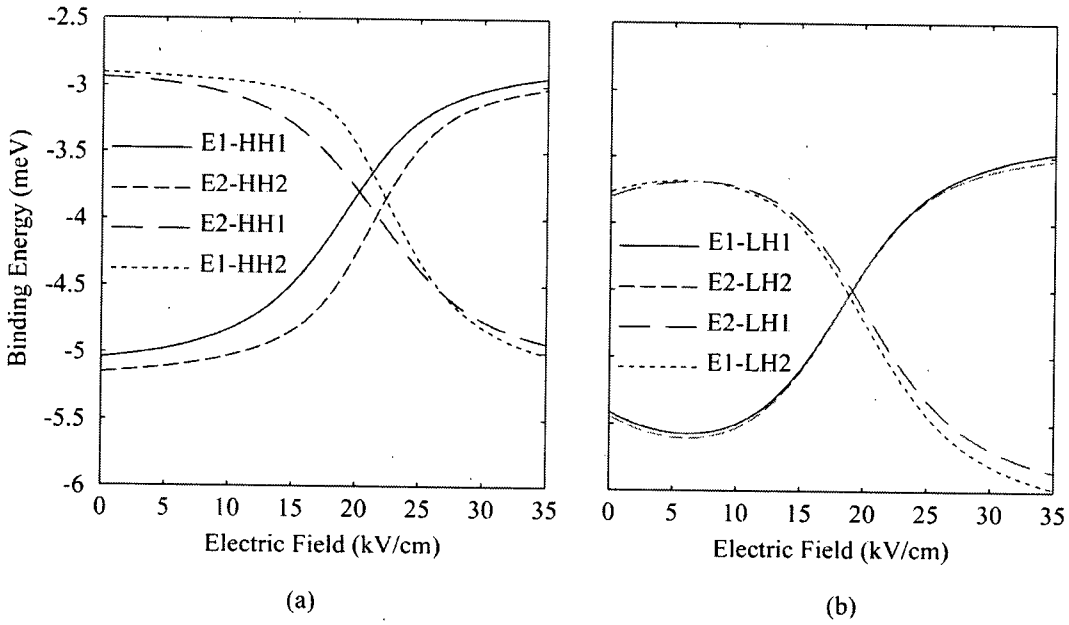

Figure 1.20: Binding energies of the excitons corresponding to the transitions (a) between the two lowest energy electron and heavy holes and (b) between the two lowest energy electron and light holes.

For small values of F, those below F_E, the binding energies corresponding to the symmetric-mode transitions are large, and the binding energies corresponding to the asymmetric-mode transitions are small. For large values of F, those above F_E, the binding energies corresponding to the symmetric-mode transitions are small, and the binding energies corresponding to the asymmetric-mode transitions are large. This behavior of the binding energies in Fig. 1.20 is similar to the behavior of the squared overlap integrals in Fig. 1.19 because, as mentioned above, separating the electron and hole wave functions

of an exciton in the z direction (direction normal to the planes of the quantum wells) increases the in-plane exciton size.

Now, having obtained the electric-field dependence of the squared overlap integrals and the binding energies in CQW structures, it is easy to describe electroabsorption in these structures. Fig. 1.21 shows the absorption spectra for the TM polarization for $F = 0$, 20, and 35 kV/cm. According to the polarization selection rules given in Eqs. (1.48) and (1.49), heavy-hole excitons do not contribute to the TM absorption spectra, and only the light-hole exciton peaks are present in Fig. 1.21. For $F = 0$ kV/cm, the two exciton peaks in the figure are dominated by the symmetric-mode transitions, which have large squared overlap integrals and large binding energies for small F ($F < F_E$). In the absorption spectrum, the symmetric-mode transitions are indistinguishable from the asymmetric-mode transitions, not only because the asymmetric-mode transitions have small squared overlap integrals and small binding energies for small F, but also because the energy separations between the symmetric-mode transitions and asymmetric-mode transitions are of the same order of magnitude as the HWHM of the broadening function. For $F = 35$ kV/cm, the heights and the energy/wavelength positions of the two peaks are similar to those for $F = 0$ kV/cm, however, for $F = 35$ kV/cm, the peaks are dominated by asymmetric-mode transitions, as they have large squared overlap integrals and large binding energies for large F ($F > F_E$). For $F = 20$ kV/cm, however, the symmetric-mode transitions and the asymmetric-mode transitions make similar contributions to the

absorptions peaks, which are considerably lower than the absorption peaks for $F = 0$ and 35 kV/cm.

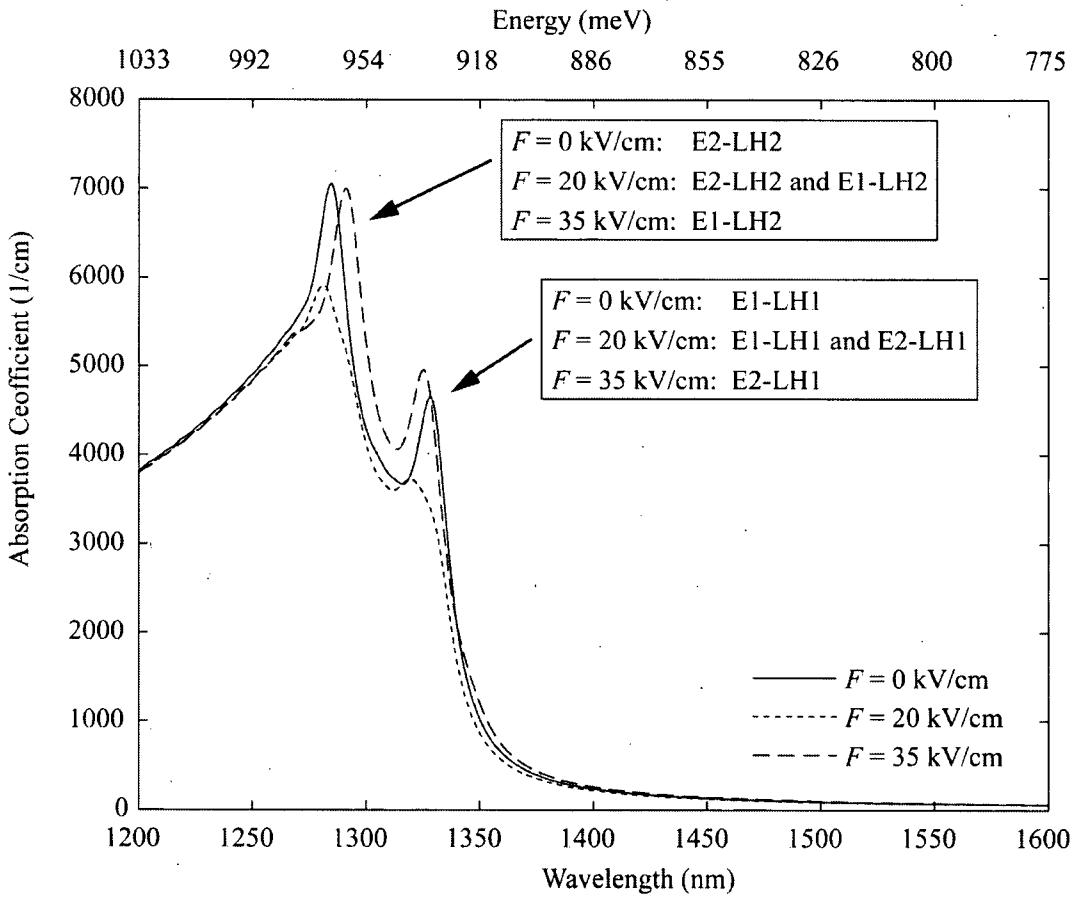

Figure 1.21: Absorption spectra for the TM polarization.

The fact that the absorption peaks are smaller when the symmetric-mode transitions and asymmetric-mode transitions make similar contributions, as compared to when one type of transition dominates, cannot be solely explained by the squared overlap integrals in Fig. 1.19. This is because there is no significant electric-field-induced change in the energies of the transitions and the total sum of the squared overlap integrals. For

example, in Fig. 1.19(b), the squared overlap integrals for the symmetric-mode transitions are ~1, and those for the asymmetric-mode transitions are ~0 for $F \approx 7$ kV/cm. Therefore, the total sum of the squared overlap integrals is ~1. When $F \approx 22$ kV/cm, the squared overlap integrals for both the symmetric-mode and asymmetric mode transitions are ~0.5, so that the total sum of the squared overlap integrals is, again, ~1. The squared overlap integrals, alone, therefore, conserve the absorption strength in Eq. (1.45). However, the squared overlap integrals in Eq. (1.45) are scaled by the corresponding values of $\left|\phi_{nm}(\vec{\rho}=0)\right|^2$, which are, again, proportional to the binding energies. For small F, the absorption peaks are large because they are dominated by the symmetric-mode transitions, which have their squared overlap integrals (~1) scaled by large $\left|\phi_{nm}(\vec{\rho}=0)\right|^2$ calculated for large binding energies of about -5.5 meV. For $F \approx 20$ kV/cm, however, the absorption peaks are small because the squared overlap integrals for the symmetric-mode and asymmetric-mode transitions (their sum is ~1) are scaled by small $\left|\phi_{nm}(\vec{\rho}=0)\right|^2$ calculated for small binding energies of about -4.5 meV. For $F \approx 35$ kV/cm, the absorption peaks are large again because they are now dominated by the asymmetric-mode transitions, which have their squared overlap integrals (~1) scaled by large $\left|\phi_{nm}(\vec{\rho}=0)\right|^2$ calculated for small binding energies of about -6 meV.

Similar to Fig. 1.21, Fig. 1.22 shows the absorption spectra for the TE polarization. The electroabsorption process for the TE polarization is analogous to that for the TM

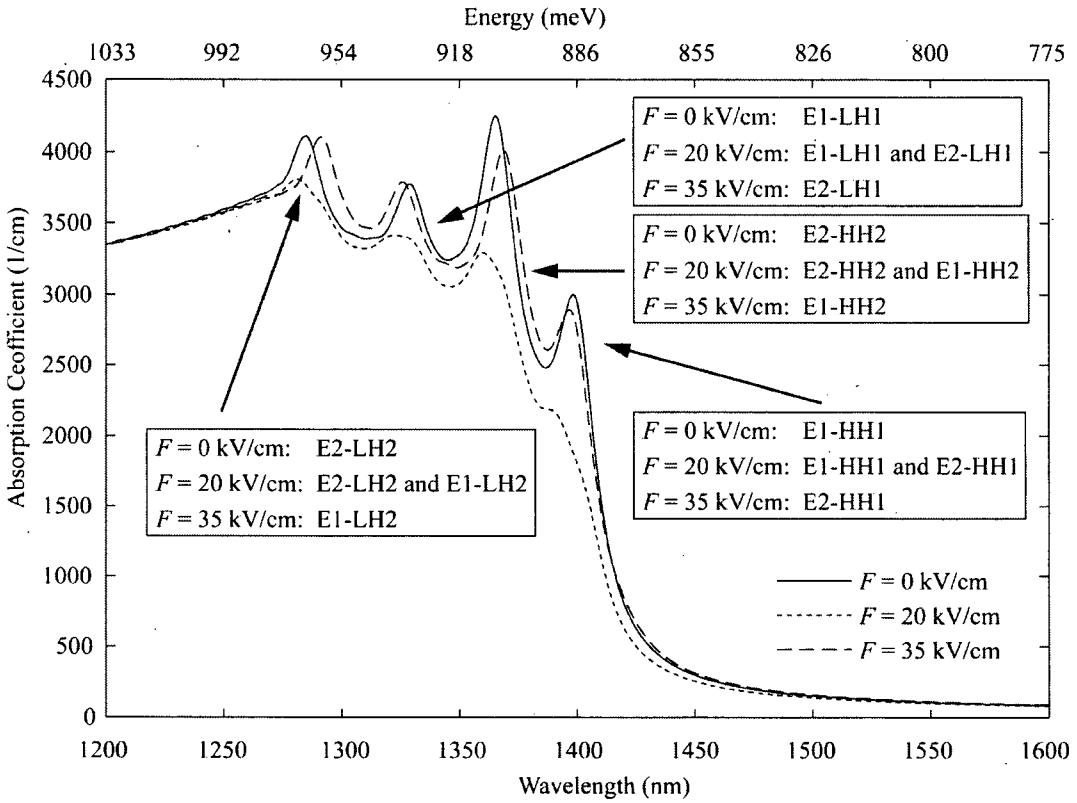

Figure 1.22: Absorption spectra for the TE polarization.

polarization, except that the polarization selection rules allow for the participation of the heavy-hole excitons as well. Because the heavy holes have larger masses than the light holes, the heavy-hole excitons typically have lower transition energies than the light-hole excitons. This point is also illustrated in Fig. 1.23, which shows the transition energies/wavelength for the heavy-hole and light-hole excitons. For $F < F_E$, the absorption spectra for both polarizations are dominated by the symmetric-mode transitions, and the energies of these transitions change only slightly with F. As F is increased above F_E, the symmetric-mode transitions show a certain amount of red shift

(E1–HH1 and E1–LH1 transitions) or blue shift (E2–HH2 and E2–LH2 transitions). Here, however, the absorption spectra are dominated by the asymmetric-mode transitions, which do not display significant red or blue shifts. Consequently, the absorption peaks do not move left or right on the horizontal axis in response to changes in F. Rather, the absorption peaks only move up and down, creating large changes in the areas below the absorption spectra. Such behavior is very desirable for obtaining large electrorefraction effects in CQW structures [60].

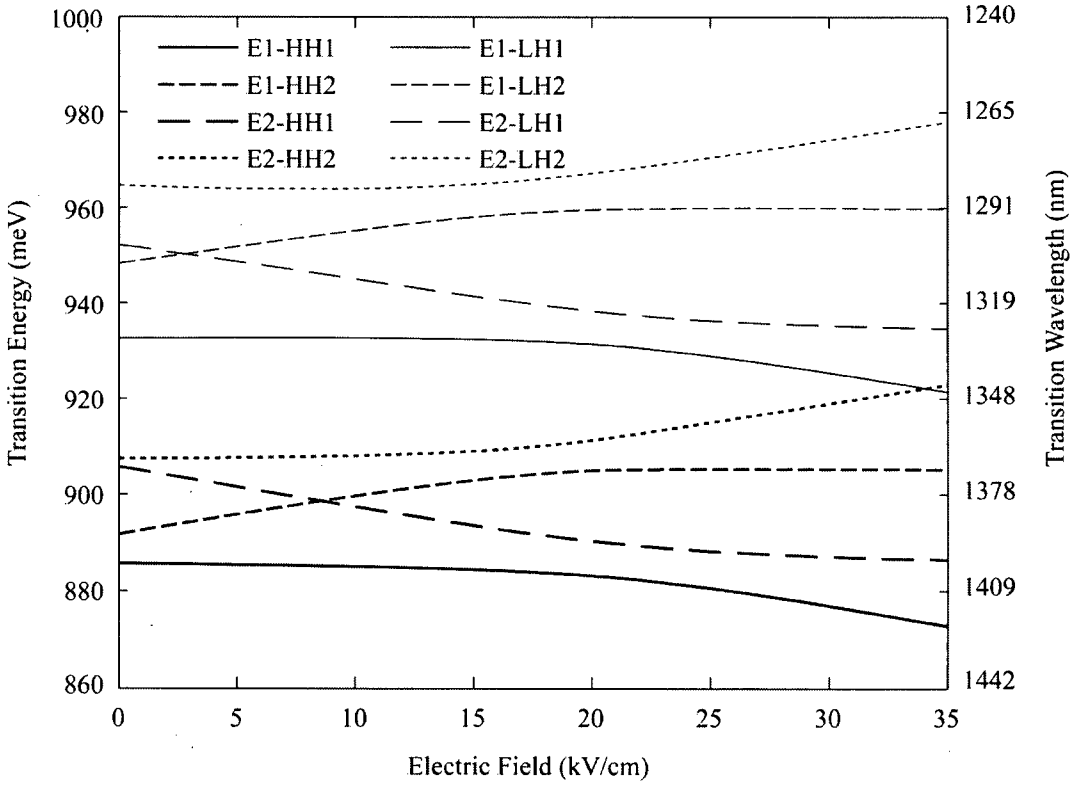

Figure 1.23: Transition energies and wavelengths for the heavy-hole and light-hole excitons.

Figs. 1.24(a) and (b) show the change of the absorption coefficient and the refractive index for the TM polarization when F is switched between 0 and 20 kV/cm and between 20 and 35 kV/cm, respectively. Because there is no significant blue or red shifting of the

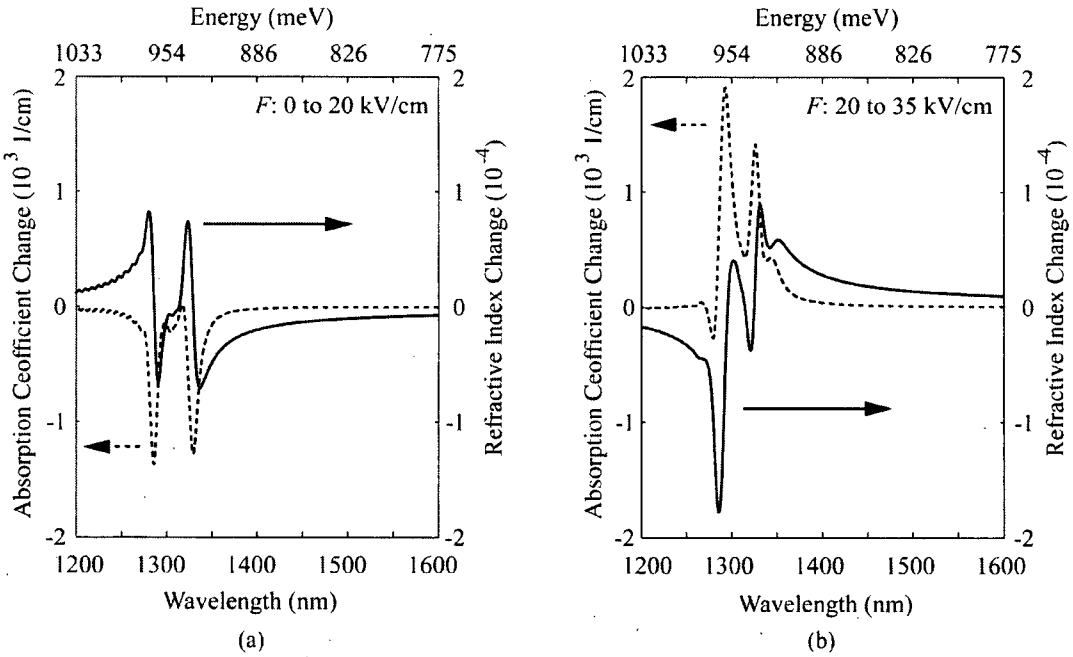

Figure 1.24: TM polarization absorption coefficient change and refractive index change when F is switched between (a) 0 and 20 kV/cm and (b) 20 and 35 kV/cm.

absorption peaks, the absorption coefficient changes in Figs. 1.24(a) and (b) are well localized in wavelength. For the same reason, the absorption coefficient changes in Figs. 1.24(a) and (b) are almost entirely negative and positive, respectively. Consequently, for the wavelengths that are longer than the wavelength corresponding to the lowest energy exciton peak, the Kramers–Krönig relation in Eq. (1.22) predicts large refractive index

changes that are respectively also negative and positive, as shown in Figs. 1.24(a) and (b). The same is true for the absorption coefficient change and the refractive index corresponding to the TE polarization, as shown in Figs. 1.25(a) and (b).

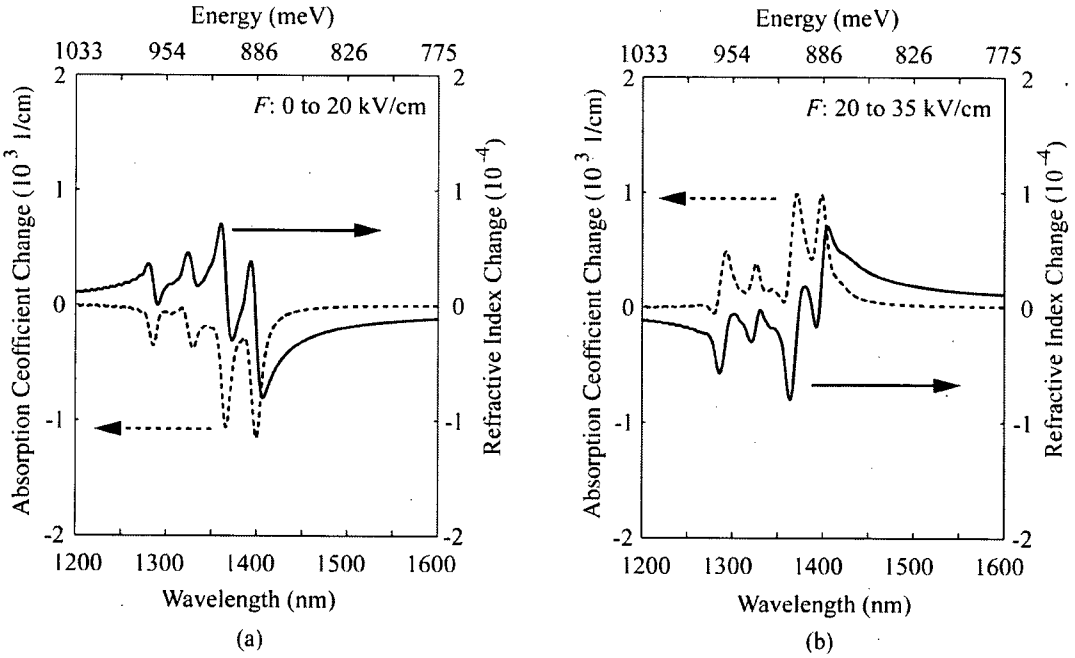

Figure 1.25: TE polarization absorption coefficient change and refractive index change when F is switched between (a) 0 and 20 kV/cm and (b) 20 and 35 kV/cm.

Unlike in CQW structures, in SQWs, an application of the electric field causes large red shifts of the absorption peaks, so that both large positive and large negative changes of the absorption spectra are created (see Fig. 1.15). The opposite-sign changes of the absorption coefficients in SQWs create opposite-sign changes in the refractive indices at higher wavelengths, which is highly undesirable [60].

Fig. 1.26 shows the electric-field-dependent refractive index changes for three different wavelengths across the C-band. Disregarding the increase of the refractive indices for the

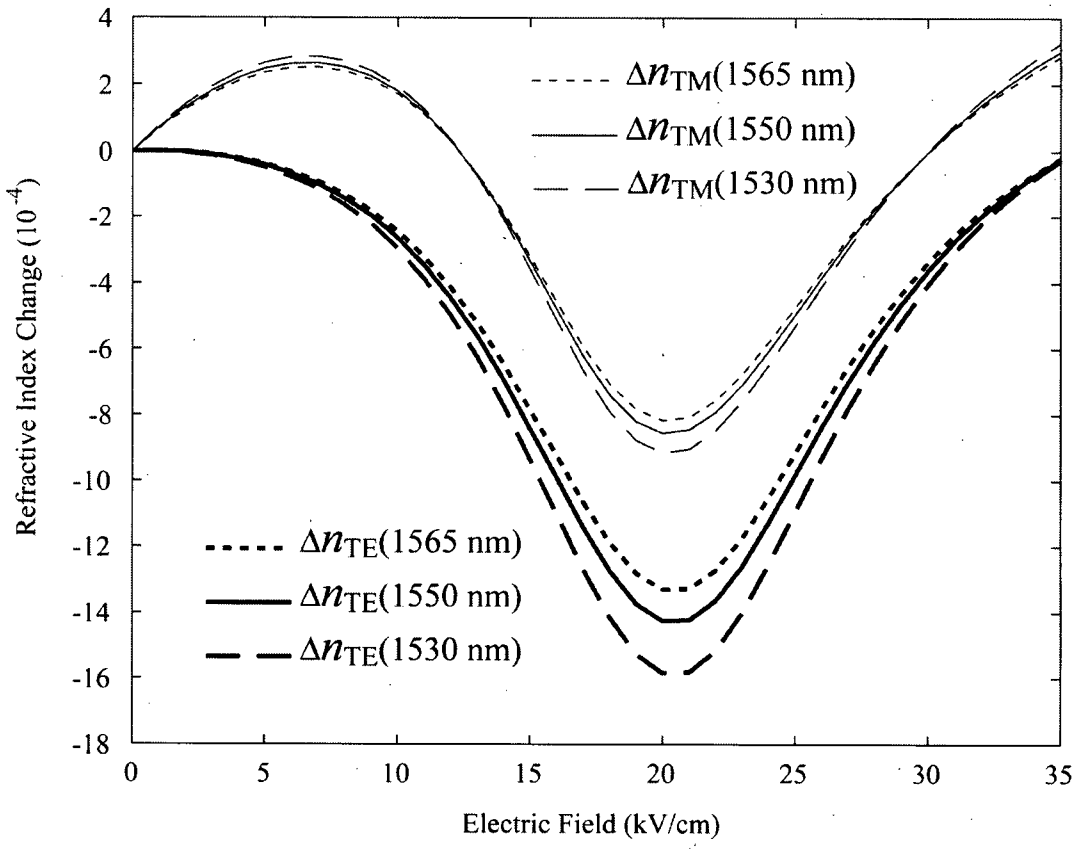

Figure 1.26: Electric field dependence of the refractive index changes for the TE and TM polarizations across the C-band.

TM polarization around $F \approx 7$ kV/cm, which are due to the increase of the light-hole absorption peaks mentioned above, the refractive indices decrease with F in the region below F_E and increase with F in the region above F_E for all curves in Fig. 1.26. The "V" shapes of the curves are characteristic for CQW structures. For any wavelength in Fig. 1.26, the electrorefractive effect is larger for the TE polarization than for the TM

polarization because the heavy-hole excitons participate in the electrorefraction for the TE polarization and are closer to the wavelength of operation than the light-hole excitons. Consequently, the CQW structures are typically intended for TE Mach–Zehnder modulators, where either the negative slope of the refractive index change below F_E or the positive slope of the refractive index change above F_E can be used [60], [80].

In Fig. 1.26, the refractive index change shows relatively small dependence on the wavelength of operation across the C-band. If this dependence was required to be decreased even further, detuning of the lowest energy excitons from the wavelength of operation would need to be increased. The exciton energies could simply be increased by decreasing the thicknesses of the quantum wells in the CQW structure. Unfortunately, the larger the detuning, the smaller the electrorefraction effect. Both of these trends are evident from Fig. 1.26, where the TM polarization exhibits a smaller dependence on the wavelength of operation as well as a smaller electrorefraction effect. Also, due to the larger detuning of the corresponding excitons, the TM polarization exhibits smaller optical loss and modulation of the optical loss at the wavelength of operation than the TE polarization does. However, the magnitude of the optical loss is not easily modeled as it strongly depends on the broadening function used in the model. The Gaussian broadening functions tend to underestimate the loss, while the Lorentzian broadening functions tend to overestimate the loss. For example, the semi-empirical Lorentzian broadening function used for modeling of the CQW structure analyzed above, and all of the CQW structures

in this thesis, has a HWHM of about 6 meV [64] and predicts the absorption coefficients for the two polarizations to be in the 10s of cm^{-1} at 1550 nm. However, if a Gaussian broadening function with the same value for the HWHM is used, the corresponding absorption coefficients are several orders of magnitude smaller for both polarizations, again at 1550 nm. Nevertheless, the choice of the broadening function has little (practically no) effect on the refractive index change at the wavelength of operation. Fig. 1.27 compares the refractive index changes obtained using the Gaussian and the Lorentzian broadening functions at 1550 nm, showing no appreciable difference between the two. It turns out that no appreciable difference between the two broadening functions

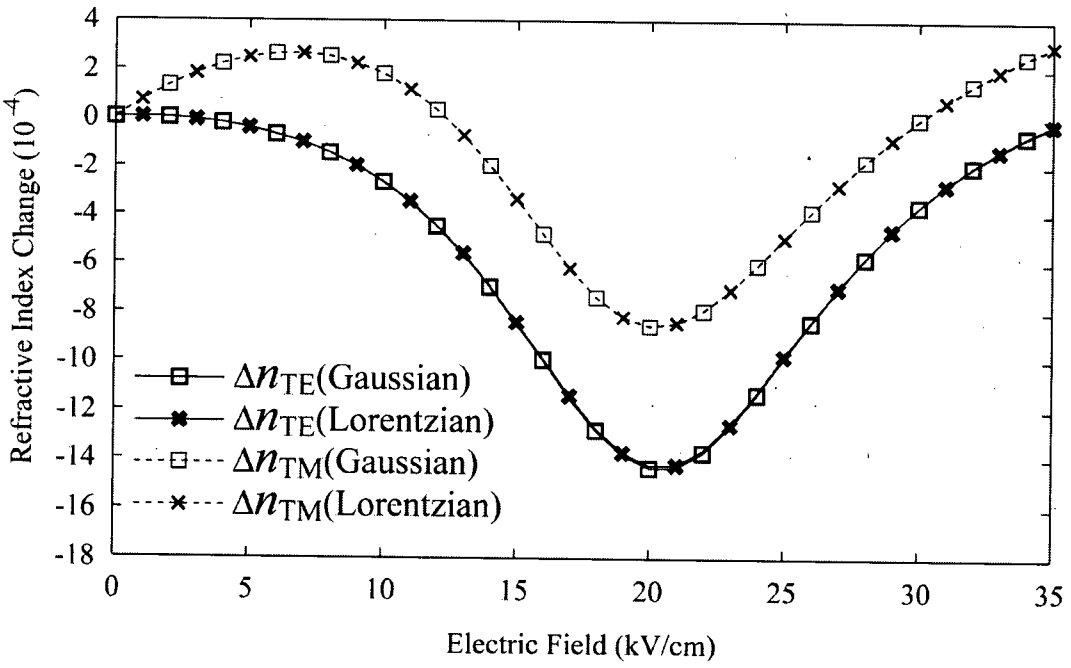

Figure 1.27: Comparison of the 1550 nm refractive index changes obtained using the Gaussian and the Lorentzian broadening functions.

is seen even if the HWHMs of the broadening functions are changed. The refractive

index changes are insensitive to the choice of the broadening function because the choice of the broadening function does not significantly affect the areas under the absorption spectra for relatively large wavelength detunings. According to the Kramers–Krönig relation given in Eq. (1.22), it is these areas that affect the magnitudes of the refractive index changes.

Unfortunately, due to the lack of experimental reports on the absorption spectra in InGaAlAs-based CQW structures, choosing the appropriate broadening function for the modeling of these structures is a somewhat challenging task. One way of ensuring small optical losses at the wavelengths of operation is to allow for large wavelength detunings that are comparable to those used in typical 1550 nm ER MQW modulators. For example, in [81], an optical waveguide of a p-i-n diode contained multiple repetitions of 85 Å thick InGaAsP quantum wells and 85 Å thick InP barriers in the 0.4 μm thick intrinsic region. Detuning of the lowest energy exciton in the SQWs from the 1550 nm wavelength of operation was 133 nm. Optical waveguide loss for the TE polarization was measured to be ~1 cm^{-1} (~0.4 dB/mm) for zero applied voltage. Due to the large red shift of the lowest energy exciton, which is characteristic for SQWs, a 4 V change in the applied voltage induced more than a three-fold increase in the measured waveguide loss and less than 4×10^{-4} increase in the measured effective refractive index. A similar behavior was observed in [82] for a p-i-n diode containing twenty 103 Å InGaAsP wells and 80 Å InP barriers in the intrinsic region, which formed ~60 % overlap with the optical mode. A

voltage change from 0 to 5 V induced a red shift of the lowest energy exciton from ~1440 nm to ~1480 nm, resulting in a large refractive index change (*i.e.*, large phase change across the device) as well as a large optical loss increase for 1557 nm wavelength in a 0.6 mm long waveguide, as shown in Fig. 1.28. As can be seen in the figure, optical loss for

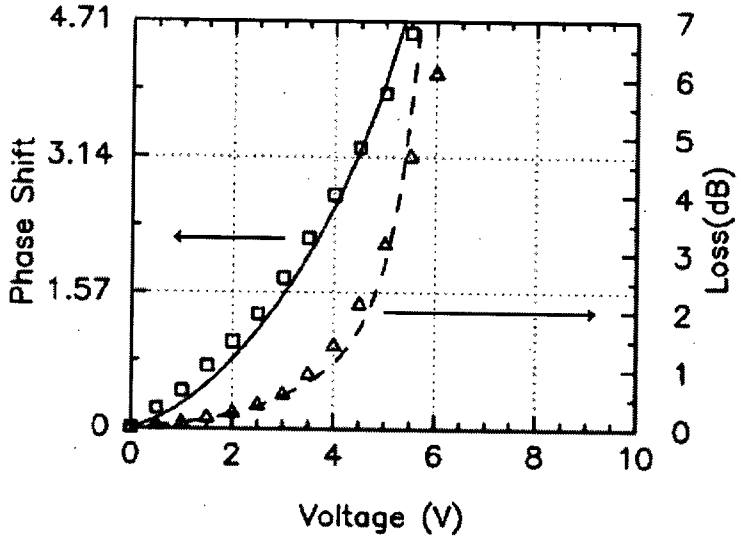

Figure 1.28: Optical loss and phase shift for 1557 nm wavelength in a 0.6 mm long section of an optical waveguide containing twenty InGaAsP–InP SQWs. The squares and triangles are experimentally obtained data points, while the lines come for theoretical models that use fitting parameters [82].

small voltages is only a fraction of a decibel and increases to ~1.5 dB for a half-wave voltage of ~4.5 V. As the excitons in CQW structures do not exhibit significant red shifts for the small changes in F that are typically applied to them, the optical loss at the wavelength of operation stays relatively independent of F. For example, let's look at a half-wave phase change

$$\Delta\phi_{\pi} = \frac{2\pi}{\lambda} \times \Delta n \times \Gamma \times L = \pi \qquad (1.60)$$

in an optical modulator at λ = 1550 nm, if we assume that the optical mode has an overlap factor of Γ = 0.60 for the CQW region, which provides a refractive index change of $\Delta n = 10 \times 10^{-4}$, the interaction length would need to be L = 1.3 mm. Consequently, the optical loss of the CQW modulator can be estimated to be below 1dB for a wavelength detuning that is somewhat larger than 100 nm. Even smaller losses can be expected in CQW modulators that are not based on p-i-n diode structures. The p-doped regions are lossy not only for the electrical signal, but also for the optical mode. The optical loss due to the p-doped region, $\alpha_p \approx (25 \times 10^{-18}\ \mathrm{cm}^2) \times \Gamma_p \times p$, depends on the overlap that the region makes with the optical mode, Γ_p, as well as the amount of doping, p ($\sim 10^{18}\ \mathrm{cm}^{-3}$) [52]. Besides α_p, another major contribution to the residual, wavelength-independent loss is the photon scattering due to the imperfections of the optical waveguide geometry. For example, in a p-i-n diode having a reactive-ion-etched optical waveguide and $p = 2 \times 10^{17}$ cm^{-3}), the residual loss for the TE polarization was measured to be ~0.3 dB/mm [83]. The contribution of the wavelength-dependent loss due to the 0.4 μm thick InGaAlAs–InAlAs MQW region was ~0.2 dB/mm for ~130 nm wavelength detuning.

In addition to the above discussion on optical loss in CQW structures, there are two remaining aspects of them that should be addressed in this chapter before proceeding to the following chapters, where the contributions of this thesis to the state-of-the-art in CQW modulators are given.

First, as will be explained in more detail in Chapters 4 and 5, increasing the thickness of the middle barrier decreases the magnitude of F needed for switching in CQW structures. Unfortunately, increasing the thickness of the middle barrier also increases the sensitivity to the thickness (~3 Å) and compositional variations (1–2 %) that can be expected to occur in the CQW epitaxial layers during the growth process. In the CQW structures that have switching fields smaller than ~20 kV/cm, the layer thickness and compositional variations can be very detrimental to the electrorefraction effect. For example, Fig. 1.29 illustrates the effect of a 3 Å increase in the thickness of QW2 for the CQW structure

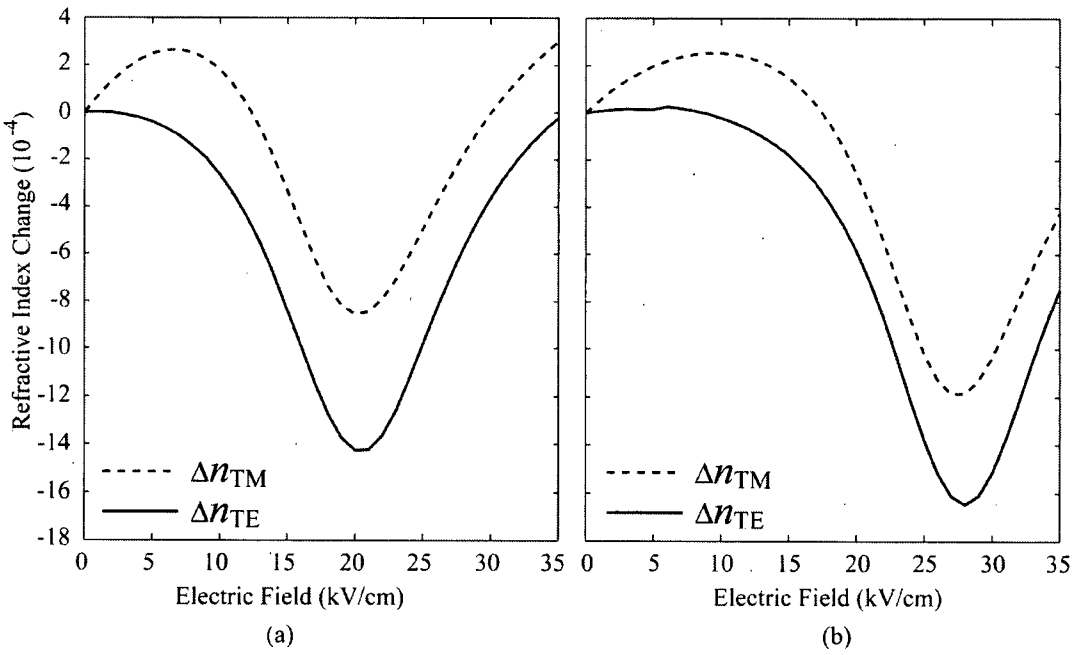

Figure 1.29: (a) 1550 nm refractive index changes for the TE and TM polarizations in the CQW structure of Fig. 1.18 (same as Fig. 1.26) and (b) the same for a 3 Å increase in the thickness of QW2.

shown in Fig. 1.18. The 3 Å thickness variation increases F_E and places the negative

slope of the refractive index change in the electric-field region in which it is supposed to be positive. Randomly distributed thickness variations (of approximately ±3 Å) are unavoidable between the epitaxial layers in CQW structures [58], and therefore, the total change in the refractive index that the optical mode experiences will be an average of the contributions to the refractive index changes that correspond to each variation. Many of these contributions will have opposite signs and diminish the total, average refractive index change in CQW structures. Again, methods for decreasing the sensitivities of CQW structures to thickness and compositional variations, without compromising the drive electric fields, will be presented in Chapters 4 and 5.

Second, in order to increase the difference between the electrorefraction effects for the TE and TM polarizations, and, thus, achieve efficient polarization modulation, as will be discussed in Chapters 2, 3, and 6, the epitaxial layers in CQW structures need to be slightly strained.

1.5.3 Strain in CQW Structures grown on (001) InP

The lattice constant of InP is $a_0 = 5.869$ Å [84], [85]. Therefore, unless the epitaxial layers in CQW structures are intended to be strained, their compositions have to be chosen so that their lattice constants match that of the (001) InP substrate. For example, $In_{0.53}Ga_{0.47}As$ and $In_{0.52}Al_{0.48}As$ are both lattice-matched to (001) InP. If an epitaxial layer

having a lattice constant a ($\neq a_0$) is grown on top of a (001) InP substrate, or some other epitaxial layer (or a stack of layers) having lattice constant a_0, the new epitaxial layer will stretch to accommodate to the lattice constant of the thick bottom layer. Strictly speaking, this is true only if the thickness of the top layer is smaller than the critical thickness, h_c, which is the maximum allowed thickness of the epitaxial layer that can be accommodated by the system without generating any material dislocations and defects [86]. The in-plane strain, *i.e.*, in-plane fractional distortion of the lattice,

$$\varepsilon_{\parallel} = \varepsilon_{xx} = \varepsilon_{yy} = \frac{a_0}{a} - 1 \tag{1.61}$$

is the same in both x and y directions for cubic semiconductors (*e.g.*, InP and GaAs) that have their lattice constants the same in all directions [85]. The strain in Eq. (1.61) is called biaxial tension or biaxial compression depending whether a is smaller or larger than a_0, respectively. The biaxial strain is accompanied by strain in the growth direction

$$\varepsilon_{\perp} = \varepsilon_{zz} = -2\frac{c_{12}}{c_{11}}\varepsilon_{\parallel}, \tag{1.62}$$

where c_{12} and c_{11} are elastic stiffness constants [85].

One of the main properties of strained epitaxial layers is energy splitting of otherwise degenerate heavy-hole and light-hole band edges. Fig. 1.30 illustrates this effect for InGaAs and InAlAs layers grown on (001) InP. In both cases, the light-hole band edge is above the heavy-hole band edge for tensile strain, and it is below the heavy-hole band edge for compressive strain. Consequently, it is possible to design the depths of QW1 and

QW2 in CQW structures to be different for light holes and heavy holes, and thereby it is possible to manipulate the relative magnitudes of the electrorefraction effect for the TE and TM polarizations, as will be shown in Chapters 2, 3, and 6. The nature of the band-edge splitting is the same for the quaternary layers studied in these chapters. Also, opposite-sign biaxial strains in some of the layers in these CQW structures are used to balance the strains in neighboring layers and increase h_c of the overall structure.

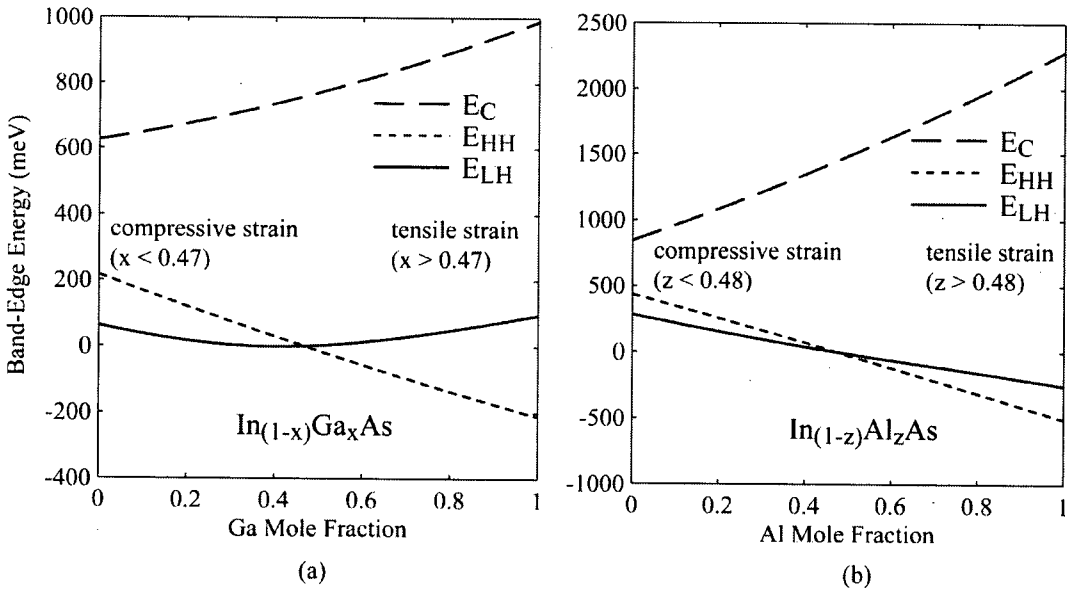

Figure 1.30: Conduction band edge (E_C), light-hole band edge (E_{LH}), and heavy-hole band edge (E_{HH}) for (a) $In_{(1-x)}Ga_xAs$ and (b) $In_{(1-z)}Al_zAs$, both of which are grown on (001) InP. The band-edge energies in (a) and (b) are plotted relative to those of $In_{0.53}Ga_{0.47}As$ and $In_{0.52}Al_{0.48}As$, respectively.

There is another important property of strained layers that is used in Chapter 4 to decrease the sensitivities of CQW structures to the compositional variations that are expected to occur during the growth process. It is obvious from Figs. 1.30(a) and (b) that

~±2 % variation in composition from the nominally unstrained $In_{0.53}Ga_{0.47}As$ and $In_{0.52}Al_{0.48}As$ layers will have a smaller effect on the light-hole band edge than on the electron or heavy-hole band edges. This is particularly true for the $In_{0.53}Ga_{0.47}As$ layer shown in Fig. 1.30(a). Therefore, if the electrorefraction effect in a CQW structure having $In_{0.53}Ga_{0.47}As$ quantum wells is based on anticrossing the light holes, rather than electrons or heavy holes, the CQW structure should be the least sensitive to compositional variations. Similar effects are characteristic of nearly-lattice-matched quaternary compounds.

The small sensitivity of the light-hole band edge to the lattice-mismatch-induced strain is due to the opposite-sign contributions of the hydrostatic and shear components of the strain, as can be explain using the model-solid theory presented below [50], [85]. The strain-dependent electron, heavy-hole, and light-hole band edges are given as

$$E_C = E^0_{V,AV} + \frac{\Delta^0}{3} + E^0_G + \Delta E^{hy}_C , \tag{1.63}$$

$$E_{HH} = E^0_{V,AV} + \frac{\Delta^0}{3} + \Delta E^{hy}_{V,AV} + \Delta E^{sh}_{HH} , \text{ and} \tag{1.64}$$

$$E_{LH} = E^0_{V,AV} + \frac{\Delta^0}{3} + \Delta E^{hy}_{V,AV} + \Delta E^{sh}_{LH} , \tag{1.65}$$

respectively, where the quantities having "0" superscripts correspond to unstrained materials. The first term in Eqs. (1.63)–(1.65) is called "the average valence-band

energy," as it is literally obtained as an average of the energies for the heavy-hole, light-hole, and split-off bands, *i.e.*,

$$E_{\mathrm{V,AV}}^{0} = \frac{E_{\mathrm{HH}}^{0} + E_{\mathrm{LH}}^{0} + E_{\mathrm{SO}}^{0}}{3}. \tag{1.66}$$

The average valence-band energy is used as an absolute energy level for each of the two materials across the heterojunction and, thus, determines the band-edge discontinuities. In the second term in Eqs. (1.63)–(1.65), Δ^0 is the spin-orbit splitting energy. The conduction band energy in Eq. (1.63) is different from the heavy-hole and light-hole band energies in Eqs. (1.64) and (1.65), respectively, because it contains the band-gap energy term (E_{G}^{0}), and because its hydrostatic strain contribution term

$$\Delta E_{\mathrm{C}}^{hy} = a_{\mathrm{C}}\left(2\varepsilon_{\parallel} + \varepsilon_{\perp}\right) \tag{1.67}$$

is proportional to the conduction-band hydrostatic deformation potential, a_{C}, rather than the valence-band hydrostatic deformation potential, a_{V}, which is the case for the hydrostatic strain contribution to the valence bands, *i.e.*,

$$\Delta E_{\mathrm{V,AV}}^{hy} = a_{\mathrm{V}}\left(2\varepsilon_{\parallel} + \varepsilon_{\perp}\right). \tag{1.68}$$

The strain-induced change of the average valence-band energy in Eq. (1.68) changes the energies of the light-hole band edge and the heavy-hole band edge in the same manner and does not lift their degeneracy. It is the shear-strain component of the total strain, not the hydrostatic-strain component, that lifts the degeneracy. The shear-strain effect on the heavy-hole and the light-hole band edges is represented by

$$\Delta E_{\mathrm{HH}}^{sh} = -\frac{1}{2}\delta E^{sh} \tag{1.69}$$

and

$$\Delta E_{\mathrm{LH}}^{sh} = -\frac{1}{2}\Delta^0 + \frac{1}{4}\delta E^{sh} + \frac{1}{2}\sqrt{\left(\Delta^0\right)^2 + \Delta^0 \delta E^{sh} + \frac{9}{4}\left(\delta E^{sh}\right)^2}, \tag{1.70}$$

respectively, where

$$\delta E^{sh} = 2b\left(\varepsilon_{\perp} - \varepsilon_{\parallel}\right). \tag{1.71}$$

The quantity b in Eq. (1.71) is the "tetragonal shear deformation potential." As b is a negative number and a_{V} is a positive number, $\Delta E_{\mathrm{LH}}^{sh}$ and $\Delta E_{\mathrm{V,AV}}^{hy}$ have opposite signs and make E_{LH} less sensitive to strain than E_{HH}. In this thesis, as is typical for ternary and quaternary strained layers [50], [85], the various quantities used in this theory are interpolated from their theoretically or experimentally obtained binary equivalents.

1.6 Thesis Outline

The following five chapters of this thesis (Chapters 2–6) present manuscripts that have been published, have been submitted for publication, or will shortly be submitted for publication in journals. More specifically, Chapter 2 (article published in IEEE Photonics Technology Letters) presents the initial design for a push-pull polarization modulator, which contains two types of InGaAlAs–InGaAlAs CQW structures in its waveguide. One of these two structures (TS structure) mainly increases the refractive index for the TM

polarization, via the anticrossing of the two lowest energy light holes, while the other structure (CS structure) mainly decreases the refractive index for the TE polarization, via the anticrossing of the two lowest energy heavy holes. In Chapter 3 (article published in Journal of Vacuum Science and Technology A), numerical simulations show that the TS structure is very insensitive to the layer thickness and compositional variations, while the CS structure is quite sensitive to these variations. In Chapter 4 (article published in IEEE Electron Device Letters), the mechanisms responsible for the decreased sensitivity of the TS structures to the layer variations are fully recognized. The anticrossing of the two lowest energy light holes, rather than the two lowest energy heavy holes or the two lowest energy electrons, is shown to be the mode of operation that is least sensitive to the layer variations, and, therefore, the most desirable technology for future CQW modulators. Chapter 5 (manuscript that will shortly be submitted for publication) presents a design method that can be used for improving the robustness to growth of CQW structures in general, including those that have their EA or ER effects based on the anticrossing of electrons or of light holes. In Chapter 6 (manuscript submitted to IEEE Photonics Technology Letters, moderate revisions have been requested), the robustness to growth of the initial design of the push-pull polarization modulator given in Chapter 2 is improved using the knowledge obtained in the work presented in Chapters 3–5. Here, besides several changes that are made to the original design, the CS structure is replaced by a more robust CQW structure that mainly decreases the refractive index for the TE polarization via the anticrossing of the two lowest energy electrons, not the heavy holes.

Chapter 7 is the concluding chapter of the thesis and contains discussion of the thesis' findings and recommendations for the future work.

References

[1] S. Ristic and N. A. F. Jaeger, "Push–pull polarization conversion using novel asymmetric coupled quantum-well structures," *IEEE Photon. Technol. Lett.*, vol. 18, no. 2, pp. 316–318, 2006.

[2] S. Ristic and N. A. F. Jaeger, "Influence of layer thickness and compositional variations on the electrorefractive properties of a quantum well polarization-conversion modulator," *J. Vac. Sci. Technol. A, Vac. Surf. Films*, vol. 24, no. 4, pp. 962–965, 2006.

[3] S. Ristic and N. A. F. Jaeger, "Robust coupled-quantum-well structure for use in electrorefraction modulators," *IEEE Electron Dev. Lett.*, vol. 28, no. 1, pp. 30–32, 2007.

[4] F. Rahmatian, "High-speed guided-wave electro-optic modulators and polarization converters in III–V compound semiconductors" Ph.D. dissertation, Dept. Elect. and Comp. Eng., University of British Columbia, Vancouver, BC, 1997.

[5] J. D. Bull, et al., "40 GHz electro-optic polarization modulator for fiber optic communications systems," in *Proc. of SPIE*, 2004, vol. 5577, pp. 133–143.

[6] G. P. Agrawal, *Fiber-Optic Communication Systems*. New York: Wiley, 1997, ch. 7.

[7] G. P. Agrawal, *Fiber-Optic Communication Systems*. New York: Wiley, 1997, ch. 1.

[8] G. P. Agrawal, *Fiber-Optic Communication Systems*. New York: Wiley, 1997, ch. 2.

[9] S. Saunders, *The McGraw-Hill High-Speed LANs Handbook*. New York: McGraw-Hill, 1996.

[10] G. L. Li and P. K. L. Yu, "Optical intensity modulators for digital and analog application," *J. Lightw. Technol.*, vol. 21, no. 9, pp. 2010–2030, 2003.

[11] G. P. Agrawal, *Fiber-Optic Communication Systems*. New York: Wiley, 1997, ch. 3.

[12] R. Ramaswami and K. N. Sivarajanl, *Optical Networks: A Practical Perspective*. San Francisco: Morgan Kaufmann Publishers, 2002, ch. 1.

[13] R. Ramaswami and K. N. Sivarajanl, *Optical Networks: A Practical Perspective*. San Francisco: Morgan Kaufmann Publishers, 2002, ch. 13.

[14] R. Ramaswami and K. N. Sivarajanl, *Optical Networks: A Practical Perspective*. San Francisco: Morgan Kaufmann Publishers, 2002, ch. 3.

[15] R. Ramaswami and K. N. Sivarajanl, *Optical Networks: A Practical Perspective*. San Francisco: Morgan Kaufmann Publishers, 2002, ch. 5.

[16] C. H. Cox, III, *Analog Optical Links: Theory and Practice*. New York: Cambridge University Press, 2004, ch. 1.

[17] C. H. Cox, III, *Analog Optical Links: Theory and Practice*. New York: Cambridge University Press, 2004, ch. 6.

[18] A. L. Campillo, "Interchannel nonlinear crosstalk in analog polarization modulated WDM systems," *J. Lightw. Technol.*, vol. 24, no. 3, pp. 1186–1193, 2006.

[19] H. Al-Raweshidy and S. Komaki, *Radio over Fiber Technologies for Mobile Communications Networks*. Boston: Artech House, 2002, ch. 2.

[20] L. Chrostowski, X. Zhao, and C. J. Chang-Hasnain, "Microwave performance of optically injection-locked VCSELs," *IEEE Trans. Microwave Theory Tech.*, vol. 54, no. 2, pp. 788–796, 2006.

[21] R. Ramaswami and K. N. Sivarajanl, *Optical Networks: A Practical Perspective*. San Francisco: Morgan Kaufmann Publishers, 2002, ch. 4.

[22] T. Tamir, *Guided-Wave Optoelectronics*. New York: Springer-Verlag, 1988, pp. 362–364.

[23] A. Yariv, *Introduction to Optical Electronics*. New York: Holt, Rinehart and Winston, 1976, pp. 256–259.

[24] A. Yariv and P. Yeh, *Optical Waves in Crystals*. New York: John Wiley and Sons, 1984, pp. 177–189.

[25] A. H. Gnauck, et al., "6 x 42.7-Gb/s transmission over ten 200-km EDFA-amplified SSMF spans using polarization-alternating RZ-DPSK," OFC 2004, in *Proc. OFC*, vol. 2, 2004.

[26] F. Heismann, "Compact electro-optic polarization scramblers for optically amplified lightwave systems," *J. Lightw. Technol.*, vol. 14, no. 8, pp. 1801–1814, 1996.

[27] N. Dagli, "Wide-bandwidth lasers and modulators for RF photonics," *IEEE Trans. Microw. Theory Tech.*, vol. 47, no. 7, pp. 1151–1171, 1999.

[28] T. Tamir, *Guided-Wave Optoelectronics*. New York: Springer-Verlag, 1988, pp. 157–167.

[29] G. L. Li, T. G. B. Mason, and P. K. L. Yu, "Analysis of segmented traveling-wave optical modulators," *J. Lightw. Technol.*, vol. 22, no. 7, pp. 1789–1796, 2004.

[30] N. A. F. Jaeger and Z. K. F. Lee, "Slow-wave electrode for use in compound semiconductor electrooptic modulators," *IEEE J. Quantum Electron.*, vol. 28, no. 8, pp. 1778–1784, 1992.

[31] Z. K. F. Lee, "Slow-wave electrode structures for III-V semiconductor based electro-optic travelling-wave modulators" M.A.Sc. Thesis, Dept. Elect. and Comp. Eng., University of British Columbia, Vancouver, BC, 1992.

[32] K. Noguchi, O. Mitomi, and H. Miyazawa, "Millimeter-wave Ti:$LiNbO_3$ optical modulators," *J. Lightw. Technol.*, vol. 16, no. 4, pp. 615–619, 1998.

[33] J. Bull, H. Kato, A. Guest, and N. Jaeger. Ultrahigh-speed, broad-band, integrated-optic mode converter for 40 Gp/s applications. JGKB Photonics Inc. (Versawave Pruduct Division). Vancouver, BC. [Online]. Available: http://www.versawave.com/products/pdf/OMI_2005_JGKB.pdf

[34] JGKB Photonics Inc. 40 Gb/s amplitude modulator electro-optic mode converter. JGKB Photonics Inc. (Versawave Pruduct Division). Vancouver, BC. [Online]. Available: http://www.versawave.com/products/pdf/Versawave_amplitude_2005.pdf

[35] JGKB Photonics Inc. 40 Gb/s amplitude modulator electro-optic mode converter. JGKB Photonics Inc. (Versawave Pruduct Division). Vancouver, BC. [Online]. Available: http://www.versawave.com/products/pdf/Versawave_polarization_2005.pdf

[36] C. Rolland, R. S. Moor, F. Shepherd, and G. Hillier, "10 Gbit/s, 1.56 μm multiquantum well InP/InGaAsP Mach-Zehnder optical modulator," *Electron. Lett.*, vol. 29, no. 5, pp. 471–472, 1993.

[37] T. Ido, H. Sano, M. Suzuki, S. Tanaka, and H. Inoue, "High-speed MQW electroabsorption optical modulators integrated with low-loss waveguides," *IEEE Photon. Technol. Lett.*, vol. 7, no. 2, pp. 170–172, 1995.

[38] S. L. Chuang, *Physics of Optoelectronic Devices*. New York: Wiley, 1995, ch. 13.

[39] S. L. Chuang, *Physics of Optoelectronic Devices*. New York: Wiley, 1995, ch. 9.

[40] T. H. Wood, "Multiple quantum well (MQW) waveguide modulators," *J. Lightw. Technol.*, vol. 6, no. 6, pp. 743–757, 1988.

[41] D. A. B. Miller, J. S. Weiner, and D. S. Chemla, "Electric-field dependence of linear optical properties in quantum well structures: waveguide electroabsorption and sum rules," *IEEE J. Quantum Electron.*, vol. QE-22, no. 9, pp. 1816–1830, 1986.

[42] D. A. B. Miller, D. S. Chemla, T. C. Damen, A. C. Gossard, and W. Wiegmann, "Electric field dependence of optical absorption near the band gap of quantum-well structures," *Phys. Rev. B*, vol. 32, no. 2, pp. 1043–1060, 1985.

[43] Reprinted with permission from J. S. Weiner et al., "Strong polarization-sensitive electroabsorption in GaAs/AlGaAs quantum well waveguides," *Appl. Phys. Lett.*, vol. 47, no. 11, pp. 1148–1150, 1985. Copyright 1985, American Institute of Physics.

[44] J. S. Weiner, D. A. B. Miller, and D. S. Chemla, "Quadratic electro-optic effect due to the quantum-confined Stark effect in quantum wells," *Appl. Phys. Lett.*, vol. 50, no. 13, pp. 842–844, 1987.

[45] Reprinted with permission from N. Susa, "Electric-field-induced refractive index changes in three-step asymmetric coupled quantum wells," *J. Appl. Phys.*, vol. 73, no. 12, pp. 8463–8470, 1993. Copyright 1993, American Institute of Physics.

[46] B. E. A. Saleh and M. C. Teich, *Fundamentals of Photonics*. New York: Wiley, 1991, pp. 928–933.

[47] R. Lewén, S. Irmscher, U. Westergren, L. Thylén, and U. Eriksson, "Segmented transmission-line electroabsorption modulators," *J. Lightw. Technol.*, vol. 22, no. 1, pp. 172–179, 2004.

[48] G. L. Li, T. G. B. Mason, and P. K. L. Yu, "Analysis of segmented traveling-wave optical modulators," *J. Lightw. Technol.*, vol. 22, no. 7, pp. 1789–1796, 2004.

[49] F. Devaux, S. Chelles, A. Ougazzaden, A. Mircea, and J. C. Harmand, "Electroabsorption modulators for high-bit-rate optical communications: a comparison of strained InGaAs/InAlAs and InGaAsP/InGaAsP MQW," *Semicond. Sci. Technol.*, vol. 10, pp. 887–901, 1995.

[50] S. L. Chuang, *Physics of Optoelectronic Devices*. New York: Wiley, 1995, pp. 662–670.

[51] T. Ido, S. Tanaka, M. Suzuki, M. Koizumi, H. Sano, and H. Inoue, "Ultra-high-speed multiple-quantum-well electro-absorption optical modulators with integrated waveguides," *J. Lightw. Technol.*, vol. 14, no. 9, pp. 2026–2034, 1996.

[52] J. Piprek, Y. Chiu, and J. E. Bowers, "Multi-quantum-well electroabsorption modulators," in *Proc. of SPIE*, 2002, vol. 4646, pp. 609–617.

[53] I. Betty, M. G. Boudreau, R. A. Griffin, A. Feckes, "An empirical model for high yield manufacturing of 10Gb/s negative chirp InP Mach-Zehnder Modulators," in *Proc. OFC'05 Tech. Digest. (Optical Fiber Communication)*, vol. 3, 2005, paper OWE5.

[54] S. Akiyama et. al., "40 Gb/s InP-based Mach-Zehnder modulator with a driving voltage of 3 V_{pp}," in *Proc. IPRM (International Conference on Indium Phosphide and Related Materials)*, 2004, paper ThA1-4, pp. 581–584.

[55] J. P. Pang, K. Tada, Y. Nakano, H. Feng, "Multiple-quantum-well traveling-wave-type ultra-high-speed optical modulator," in *Proc. OECC'98 Tech. Digest. (Optoelectronics and Communications Conference)*, 1998, paper 16B1–5, pp. 454–455.

[56] J. H. Shin, C. Ozturk, S. R. Sakamoto, Y. J. Chiu, and N. Dagli, "Novel T-rail electrodes for substrate removed low-voltage, high-speed GaAs/AlGaAs electro-optic modulators," *IEEE Trans. Microw. Theory Tech.*, vol. 53, no. 2, pp. 626–643, 2005.

[57] J. H. Shin, S. Wu, and N. Dagli, "Bulk undoped GaAs–AlGaAs substrate-removed electrooptic modulators with 3.7-V-cm drive voltage at 1.55 μm," *IEEE Photon. Technol. Lett.*, vol. 18, no. 21, pp. 2251–2253, 2006.

[58] J. -H. Noh, S. Hasegawa, T. Suzuki, T. Arakawa, K. Tada, H. Asahi, "Migration-enhanced epitaxy (MEE) growth of five-layer asymmetric coupled quantum well (FACQW) and its cross-sectional STM observation," *Physica E*, vol. 23, pp. 482–486, 2004.

[59] J. C. Cartledge, C. Rolland, S. Lemerle, and A. Solheimh, "Theoretical performance of 10 Gb/s lightwave systems using a III–V semiconductor Mach-Zehnder modulator," *IEEE Photon. Technol. Lett.*, vol. 6, no. 2, pp. 282–284, 1994.

[60] C. Thirstrup, "Refractive index modulation based on excitonic effects in GaInAs-InP coupled asymmetric quantum wells," *IEEE J. Quantum Electron.*, vol. 31, no.6, pp. 988–996, 1995.

[61] S. L. Chuang, *Physics of Optoelectronic Devices*. New York: Wiley, 1995, pp. 631–650.

[62] A. Harwit and J. S. Harris, Jr., "Calculated quasi-eigenstates and quasi-eigenenergies of quantum well superlattices in an applied electric field," *J. Appl. Phys.*, vol. 60, no. 9, pp. 3211–3213, 1986.

[63] I. Galbraith and G. Duggan, "Exciton binding energy and external-field-induced blue shift in double quantum wells," *Phys. Rev. B*, vol. 40, no. 8, pp. 5515–5521, 1989.

[64] N. Susa, "Electric-field-induced refractive index changes in InGaAs–InAlAs asymmetric coupled quantum wells," *IEEE J. Quantum Electron.*, vol. 31, no. 1, pp. 92–100, 1995.

[65] A. M. Fox, D. A. B. Miller, G. Livescu, J. E. Cunningham and W. Y. Jan, "Excitonic effects in coupled quantum wells," *Phys. Rev. B*, vol. 44, no. 12, pp. 6231–6242, 1991.

[66] M. N. Islam et. al., "Electroabsorption in GaAs/AlGaAs coupled quantum well waveguides," *Appl. Phys. Lett.*, vol. 50, no. 16, pp. 1098–1100, 1987.

[67] S. R. Andrews C. M. Murray, R. A. Davies, and T. M. Kerr, "Stark effect in strongly coupled quantum wells," *Phys. Rev. B*, vol. 37, no. 14, pp. 8198–8204, 1988.

[68] J. Lee, M. O. Vassel, E. S. Koteles, and B. Elman, "Excitonic spectra of asymmetric, coupled double quantum wells in electric fields," *Phys. Rev. B*, vol. 39, no. 14, pp. 10133–10143, 1989.

[69] P. Lefebvre, P. Bonnel, B. Gil, and H. Mathieu, "Resonant tunneling via-stress-induced valence-band mixing in GaAs-(Ga,Al)As asymmetrical double quantum wells," *Phys. Rev. B*, vol. 44, no. 11, pp. 5635–5647, 1991.

[70] S. Glutsch, D. S. Chemla, and F. Bechstedt, "Numerical calculation of the optical absorption in semiconductor quantum structures," *Phys. Rev. B*, vol. 54, no. 16, pp. 11592–11601, 1996.

[71] R. Winkler, "Excitons and fundamental absorption in quantum wells," *Phys. Rev. B*, vol. 51, no. 20, pp. 14395–14409, 1995.

[72] Y. C. Chan and K. Tada, "Field induced optical effects coupled quantum wells," *IEEE J. Quantum Electron.*, vol. 27, no. 3, pp. 702–707, 1991.

[73] J. A. Trezza, M. C. Larson, S. M. Lord, and J. S. Harris, Jr., "Low-voltage, low-chirp absorptively bistable transmission modulators using type-IIA and type-IIB $In_{0.3}Ga_{0.7}As/Al_{0.33}Ga_{0.67}As/\ In_{0.15}Ga_{0.85}As$ asymmetric coupled quantum wells," *J. Appl. Phys.*, vol. 74, no. 11, pp. 6495–6502, 1993.

[74] T. H. Stievater, W. S. Rabinovich, P. G. Goetz, R. Mahon, and S. C. Binari, "A surface-normal coupled-quantum-well modulator at 1.55 μm," *IEEE Photon. Technol. Lett.*, vol. 16, no. 9, pp. 2036–2038, 2004.

[75] N. Susa, "Electric-field-induced refractive index changes in three step asymmetric coupled quantum wells," *J. Appl. Phys.*, vol. 73, no. 12, pp. 8463–8470, 1993.

[76] M. P. Earnshaw and D. W. E. Allsopp, "Electrooptic effects in GaAs–AlGaAs narrow coupled quantum wells," *IEEE J. Quantum Electron.*, vol. 37, no. 7, pp. 897–904, 2001.

[77] T. Suzuki et. al., "Observation of giant electrorefractive effect in five-layer asymmetric coupled quantum wells (FACQWs)," *J. Journal Appl. Phys.*, vol. 43, no. 12A, pp. L1540–L1542, 2004.

[78] J. P. Pang, K. Tada, Y. Nakano, and H. Feng, "Multiple-quantum-well traveling-wave-type ultra-high-speed optical modulator," in *Proc. OECC'98 Tech. Digest. (Optoelectronics and Communications Conference)*, pp. 454–455, 1998, paper 16B1–5.

[79] T. Suzuki et. al., "Fabrication and optical characterization of five-layer asymmetric coupled quantum well (FACQW)," *J. Journal Appl. Phys.*, vol. 41, no. 4B, pp. 2701–2706, 2002.

[80] H. Feng, J. P. Pang, M. Sugiyama, K. Tada, Y. Nakano, "Field-induced optical effect in a five-step asymmetric coupled quantum well with modified potential," *IEEE J. Quantum Electron.*, vol. 34, no. 7, pp. 1197–1208, 1998.

[81] H. Mohseni, H. An, Z. A. Shellenbarger, M. H. Kwakernaak, and J. H. Abeles, "Enhanced electro-optic effect in GaInAsP–InP three-step quantum wells," *Appl. Phys. Lett.*, vol. 84, no. 11, pp. 1823–1825, 2004.

[82] Reprinted with permission from W. Bardyszewski, D. Yevick, Y. Liu, C. Rolland, and S. Bradshaw, "Theoretical and experimental analysis of Mach–Zehnder quantum-well modulators," *J. Appl. Phys.*, vol. 80, no. 2, pp. 1136–1141, 1996. Copyright 1996, American Institute of Physics.

[83] N. Yoshimoto, T. Yamanaka, S. Kondo, Y. Noguchi, and K. Wakita, "Large field-induced refractive-index change on TM-polarized light in a InGaAlAs–InAlAs MQW waveguide structure," *IEEE Photon. Technol. Lett.*, vol. 9, no. 2, pp. 200–202, 1997.

[84] S. L. Chuang, *Physics of Optoelectronic Devices*. New York: Wiley, 1995, pp. 707–711.

[85] M. P. C. M. Krijn, "Heterojunction band offsets and effective masses in III–V quaternary alloys," *Semiconduct. Sci. Technol.*, vol. 6, pp. 27–31, 1991.

[86] J. J. Coleman, "Strained layer quantum well heterostructure lasers," in *Quantum Well Lasers*, P. S. Zory, Jr., Ed. San Diego: Academic Press, 1993, pp. 367–413.

Chapter 2
Push-Pull CQW Polarization Modulator

2.1 Introduction

Electrorefraction (ER) modulators based on asymmetric coupled quantum-well (ACQW) structures exhibit an electric-field-induced refractive index change that can be an order of magnitude larger than in structures based on square quantum wells [1], [2]. Compared to electroabsorption modulators, ACQW modulators, as well as ER quantum well intensity modulators, in general, are typically implemented in a directional coupler or Mach–Zehnder configuration, and they can provide lower temperature and wavelength sensitivities, lower carrier generation rates, as well as push-pull modes of operation with

adjustable chirp [3]. In this letter, we propose a novel type of ER modulator, which, in a single optical waveguide, contains multiple repetitions of two novel InGaAlAs–InAlAs ACQW structures, grown on (001) InP. By applying an appropriate bias field in the [001] direction, in one of the structures a change in the applied field can be made to cause an increase in the refractive index for TM-polarized light without a commensurate increase in the refractive index for TE-polarized light. In a similar manner, in the other structure the same change in field will cause a decrease in the refractive index for TE light without a commensurate decrease in the refractive index for TM light. Since each structure provides unequal refractive index changes for the two polarizations, if either structure were placed in an optical waveguide, a change in polarization state at the output relative to the state at the input, *i.e.*, polarization conversion, could be achieved (provided that, at the input, light is coupled into both the TE and TM modes). Typically, the powers in the two modes would be matched at the output so that a 90° polarization rotation could be obtained. To achieve push-pull polarization conversion, the effective refractive index change for the TE mode should be opposite in sign to the change for the TM mode [3]. Incorporating both of our structures into an optical waveguide will allow for the design of new push-pull-type quantum well polarization conversion (QWPC) modulators. In addition to traditional applications such as on-off keying, these modulators would likely find applications in areas not typical for quantum well modulators [4].

2.2 Device Basics

A schematic illustration of the compositions and the thicknesses of the layers in the two ACQW structures is shown in Fig. 2.1. The figure also illustrates the direction of the applied electric field F. Each structure has $In_{0.53}Al_{0.47}As$ barriers, which are lattice-matched to the InP substrate, as well as one lattice-matched $In_{0.53}Ga_{0.47}As$ well. The $In_{0.46}Ga_{0.52}Al_{0.02}As$ well in Fig. 2.1(a) is under ~0.50 % of tensile strain (TS), and the $In_{0.58}Ga_{0.37}Al_{0.05}As$ well of the structure in Fig. 2.1(b) is under ~0.34 % of compressive strain (CS). Because of these lattice-mismatch-induced biaxial strains, the structures of Fig. 2.1(a) and (b) will be referred to as the TS structure and the CS structure, respectively.

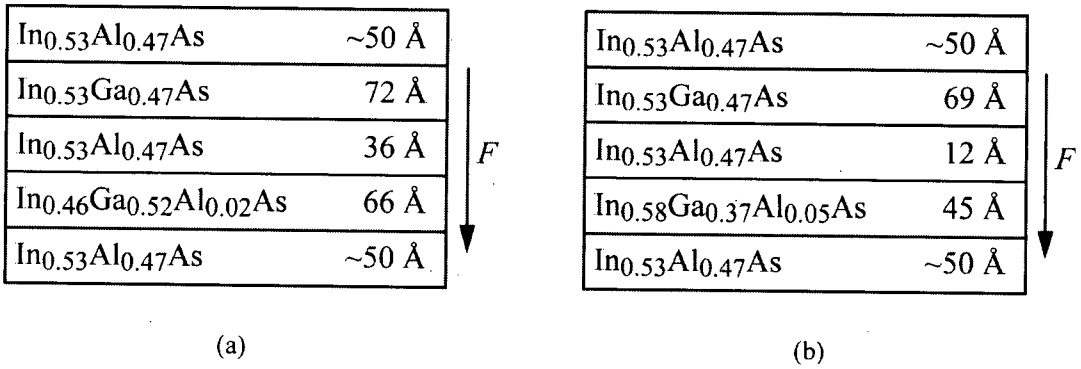

Figure 2.1: Schematic for layers (a) TS structure and (b) CS structure. Outside barriers of each structures are ~50 Å in order to ensure ~100 Å decoupling between any two neighboring structures. Direction of applied electric field F is indicated as well.

2.2.1 TS Structure

As mentioned above, for a well-chosen bias field, the TS structure provides a large electric-field-induced refractive index increase for TM light and a smaller electric-field-induced refractive index increase for the TE light. In ER modulators, typically, the refractive index change for TE light is somewhat larger than the one for TM light simply because the lowest energy light holes are at higher energies than the lowest energy heavy holes [2]. Although in some quantum well modulators the polarization dependence of the refractive index has been decreased by lowering the light-hole energies with a tensile strain [2], to the best of our knowledge, no other biaxially strained ACQW structure for use in 1550 nm ER waveguide modulators has been designed to provide a dominant TM-polarization refractive index change.

Fig. 2.2 shows the two lowest energy electron wave functions (Ψ_{E1} and Ψ_{E2}), heavy-hole wave functions (Ψ_{HH1} and Ψ_{HH2}), and light-hole wave functions (Ψ_{LH1} and Ψ_{LH2}) of the TS structure of Fig. 2.1(a) as well as the band edge diagram for its conduction and valence bands for $F = 0$, 13, and 35 kV/cm. The band gap in the figure is not to scale, and the strain-induced band edge splitting between the heavy-hole and the light-hole bands in the quantum well under tensile strain is illustrated by drawing the heavy-hole band edge with a full line and the light-hole band edge with a dashed line. The material parameters for the structures are calculated using the model-solid theory [5], [6], and the exciton

energies and wave functions are obtained using the effective-mass envelope-function approximation that includes intersubband mixing [7].

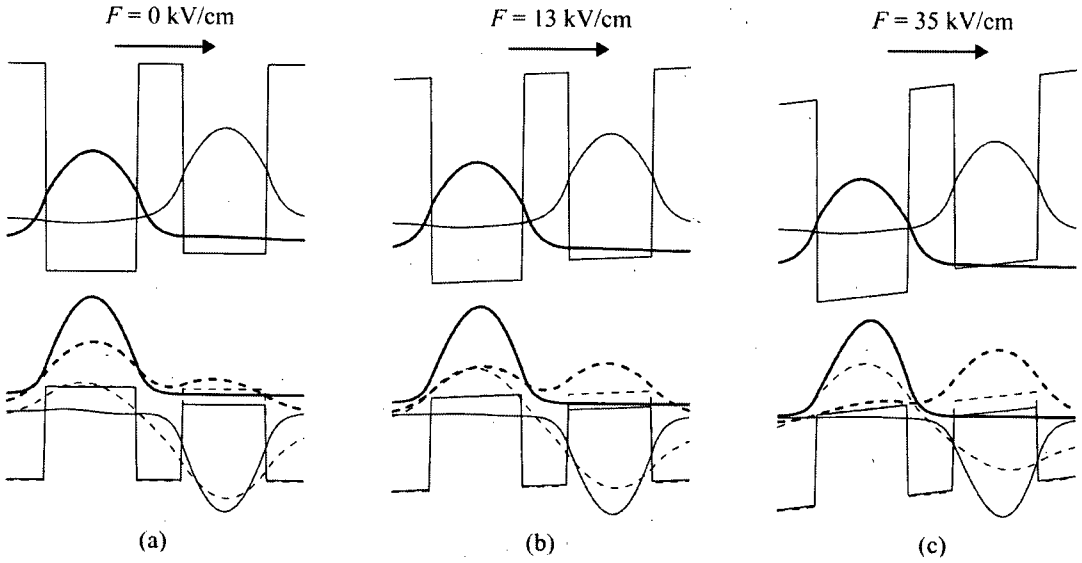

Figure 2.2: Energy band diagram of TS structure of Fig. 1(a) and two lowest energy electron, heavy-hole, and light-hole wave functions at applied electric fields of (a) 0, (b) 13, and (c) 35 kV/cm. Lowest energy electron wave function (Ψ_{E1}) and heavy-hole wave function (Ψ_{HH1}) are shown as full thick lines, whereas second lowest energy electron wave function (Ψ_{E2}) and heavy-hole wave function (Ψ_{HH2}) are shown as full thin lines. Lowest energy light-hole wave function (Ψ_{LH1}) is shown as dashed thick line, and second lowest energy light-hole wave function (Ψ_{LH2}) as dashed thin line. Light-hole band edge is indicated with dashed line. Band gap is not shown to scale.

For low electric fields, Ψ_{E1}, Ψ_{HH1}, and Ψ_{LH1} are predominantly localized in the wider unstrained well [see Fig. 2.2(a)]. Therefore, the Ψ_{E1}–Ψ_{LH1} and the Ψ_{E2}–Ψ_{LH2} excitons are direct, and the Ψ_{E1}–Ψ_{LH2} and the Ψ_{E2}–Ψ_{LH1} excitons are indirect. Since for low fields the overlaps between the electron and the light-hole wave functions of the direct excitons are

large and those of the indirect excitons are small, the direct excitons will dominate the light-hole absorption spectra for both polarizations [1].

At ~13 kV/cm, the direct and the indirect excitons start anticrossing as Ψ_{LH1} and Ψ_{LH2} are approximately equally distributed between the two wells [see Fig. 2.2(b)]. The Ψ_{E2}–Ψ_{LH1} and the Ψ_{E2}–Ψ_{LH2} excitons actually anticross at a somewhat different resonant electric field than the Ψ_{E1}–Ψ_{LH1} and the Ψ_{E1}–Ψ_{LH2} excitons. For thin middle barriers, however, these fields are close enough to be treated as one resonant electric field (F_R). At F_R, both the direct and the indirect light-hole excitons contribute to the light-hole absorption spectra, although their total contribution is smaller than it was for low electric fields because Ψ_{LH1} and Ψ_{LH2} are further delocalized [1]. In fact, at F_R, the area underneath the absorption spectrum of the Ψ_{E1}–Ψ_{LH1}, Ψ_{E1}–Ψ_{LH2}, Ψ_{E2}–Ψ_{LH1}, and Ψ_{E2}–Ψ_{LH2} excitons will be at its minimum for either polarization. For fields greater than F_R, the Ψ_{E1}–Ψ_{LH1} and Ψ_{E2}–Ψ_{LH2} excitons become indirect and the Ψ_{E2}–Ψ_{LH1} and the Ψ_{E1}–Ψ_{LH2} excitons become direct [see Fig. 2.2(c)]. The area underneath the absorption spectrum of the light-hole excitons, for either polarization, will increase to be approximately as large as it was for very low fields. Similar anticrossings of the heavy-hole excitons do not occur as the tensile strain in the strained well makes the well effectively shallower for Ψ_{HH1}. Ψ_{HH1} consequently stays localized to the unstrained well for the electric fields of interest here.

Considering that the heavy-hole momentum matrix element is practically zero for TM light, the area underneath the total absorption spectrum (including both the heavy-hole and the light-hole excitons) for the TM polarization will change in the same manner as the area underneath the light-hole excitons [3]. Also, there will be a similar, although smaller, change of the area underneath the total absorption spectrum for the TE polarization. The change is smaller because the momentum matrix element for the anticrossing light-hole excitons is one quarter of its value for TM polarization, and the heavy-hole excitons, although having a large momentum matrix element for TE polarization, remain stationary and inactive for the electric fields of interest.

As the two quantum wells are narrow enough to prevent the light-hole excitons from sizable "red shifting," the change of refractive index for TM light (Δn_{TM}), at wavelengths higher than the wavelength corresponding to the absorption peak of the Ψ_{E1}–Ψ_{LH1} exciton (λ = 1394 nm for F = 0 kV/cm), will follow the change of area underneath the TM polarization absorption spectrum in a straightforward manner [1]. As the electric field is increased toward F_R, the slope of Δn_{TM} will be negative, and as the electric field is increased above F_R, the slope will be positive. The change of the refractive index for TE light (Δn_{TE}) will behave similarly, following the smaller change of the area underneath the TE polarization absorption spectrum.

Fig. 2.3 illustrates how Δn_{TM} and Δn_{TE} of the TS structure, plotted relative to their zero-electric-field values, depend on the electric field. The two curves are plotted for operation at λ = 1550 nm and are labeled $\Delta n_{TM(TS)}$ and $\Delta n_{TE(TS)}$, respectively. Similarly, Fig. 2.3 also depicts Δn_{TE} and Δn_{TM} of the CS structure ($\Delta n_{TE(CS)}$ and $\Delta n_{TM(TC)}$, respectively).

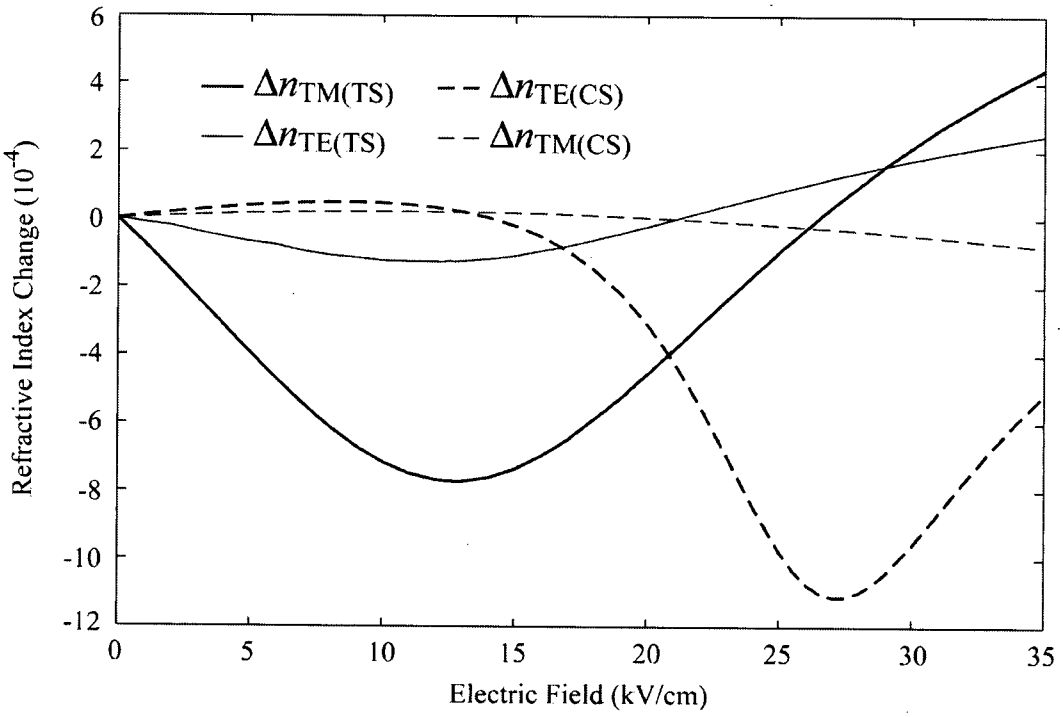

Figure 2.3: Refractive index changes of TS and CS structures, for both TE and TM polarizations, plotted relative to zero-electric-field values at λ = 1550 nm. $\Delta n_{TM(TS)}$ and $\Delta n_{TE(TS)}$ are labels for refractive index changes for respective TM and TE polarizations of TS structure. Similarly, $\Delta n_{TE(CS)}$ and $\Delta n_{TM(CS)}$ are refractive index changes for TE and TM polarizations of CS structure.

2.2.2 CS Structure

Fig. 2.4 depicts the band edge diagram and the two lowest energy electron, heavy-hole, and light-hole wave functions of the CS structure of Fig. 2.1(b), as was done for the TS structure in Fig. 2.2, now for $F = 0$, 27, and 35 kV/cm. In this case, however, it is the

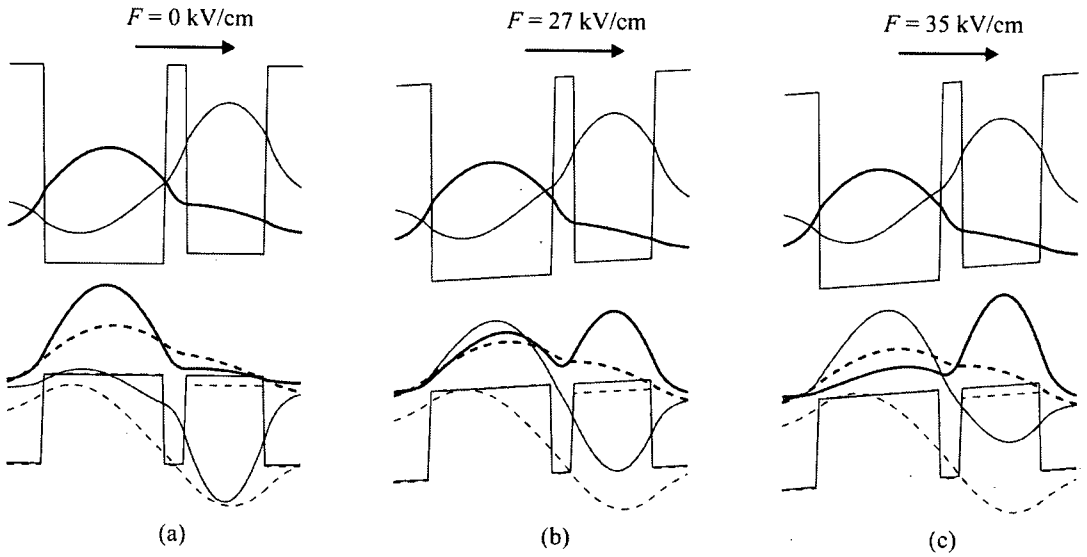

Figure 2.4: Energy band diagram of CS structure of Fig. 1(b) and two lowest energy electron, heavy-hole, and light-hole wave functions at applied electric fields of (a) 0, (b) 27, and (c) 35 kV/cm. Energy band diagrams and wave functions are depicted as in Fig. 2.2.

light-hole excitons that are stationary because the compressive strain in the right-hand side well makes it effectively shallower for the light holes. The CS structure is designed so that $F_R \approx 27$ kV/cm for the heavy-hole excitons. Considering that the heavy-hole momentum matrix element for the TM polarization is zero and that it is dominant for the TE polarization, the slopes of $\Delta n_{TE(CS)}$ on either side of F_R will have larger magnitudes as

compared to those of $\Delta n_{TM(CS)}$ for the electric fields of interest, as shown in Fig. 2.3. Here, the wavelength corresponding to the absorption peak of the $\Psi_{E1}-\Psi_{HH1}$ exciton, for $F = 0$ kV/cm, is $\lambda = 1465$ nm.

2.3 Low-Chirp Push-Pull QWPC Modulator

Between $F \approx 15$ kV/cm and $F \approx 25$ kV/cm, the TS structure mainly contributes a positive slope of $\Delta n_{TM(TS)}$ (with a much smaller positive slope of $\Delta n_{TE(TS)}$), and the CS structure mainly contributes a negative slope of $\Delta n_{TE(CS)}$ (with a much smaller negative slope of $\Delta n_{TM(CS)}$). Placed together in an optical waveguide of a QWPC modulator, multiple repetitions of the two structures will cause the effective refractive index seen by the fundamental TM mode ($n_{eff,TM}$) to increase and the effective refractive index seen by the fundamental TE mode ($n_{eff,TE}$) to decrease, providing a push-pull polarization conversion for input light that contains both polarizations.

Each structure's relative contribution to the changes in $n_{eff,TM}$ and $n_{eff,TE}$ depends on the structure's overlap with the TM and TE modes, respectively. These optical overlaps can be controlled by adjusting the number of repetitions of each structure in the waveguide, by adjusting the position and order of the repetitions of the two structures, and/or by adjusting the waveguide's geometry. For example, if one were to form a symmetric slab waveguide consisting of an $In_{0.53}Al_{0.47}As$ substrate, six repetitions of the TS structure,

five repetitions of the CS structure, six repetitions of the TS structure, and an $In_{0.53}Al_{0.47}As$ superstrate, *i.e.*, an $In_{0.53}Al_{0.47}As/6\times TS/5\times CS/6\times TS$ /$In_{0.53}Al_{0.47}As$ structure, in a 3.4 mm long waveguide, a 90° polarization rotation could be achieved when the electric field was increased from 20 to 25 kV/cm. Here, the magnitudes of the changes in $n_{eff,TM}$ and $n_{eff,TE}$ are relatively closely matched so that only a small chirp $\alpha_H < 0.1$ [3] should arise due to nonlinear refractive index and absorption changes in the two structures. Also, a similar result would be obtained or an $In_{0.53}Al_{0.47}As/10\times TS/6\times CS/In_{0.53}Al_{0.47}As$ structure. In both examples, the linear electro-optic contributions have been taken into account.

References

[1] C. Thirstrup, "Refractive index modulation based on excitonic effects in GaInAs-InP coupled asymmetric quantum wells," *IEEE J. Quantum Electron.*, vol. 31, no.6, pp. 988–996, 1995.

[2] H. Feng, J. P. Pang, M. Sugiyama, K. Tada, Y. Nakano, "Field-induced optical effect in a five-step asymmetric coupled quantum well with modified potential," *IEEE J. Quantum Electron.*, vol. 34, no. 7, pp. 1197–1208, 1998.

[3] G. L. Li and P. K. L. Yu, "Optical intensity modulators for digital and analog application," *J. Lightw. Technol.*, vol. 21, no. 9, pp. 2010–2030, 2003.

[4] A. H. Gnauck, et al., "6 x 42.7-Gb/s transmission over ten 200-km EDFA-amplified SSMF spans using polarization-alternating RZ-DPSK," OFC 2004, in *Proc. OFC*, vol. 2, 2004.

[5] M. P. C. M. Krijn, "Heterojunction band offsets and effective masses in III–V quaternary alloys," *Semiconduct. Sci. Technol.*, vol. 6, pp. 27–31, 1991.

[6] S. L. Chuang, *Physics of Optoelectronic Devices.* New York: Wiley, 1995, pp. 154–157.

[7] I. Galbraith and G. Duggan, "Exciton binding energy and external-field-induced blue shift in double quantum wells," *Phys. Rev. B*, vol. 40, no. 8, pp. 5515–5521, 1989.

Chapter 3
Robustness of Push-Pull CQW Polarization Modulator

3.1 Introduction

Studies on optimization of electro-optic [1] and nonlinear [2] properties of asymmetric coupled quantum well (ACQW) structures have been performed for many years now. Together with three-step quantum well structures [3], ACQW structures [4] have been shown to provide electrorefractive responses that are considerably greater than the ones of square quantum wells.

Recently, the authors proposed two InGaAlAs–InAlAs ACQW structures, grown on (001) InP, which, due to their electrorefractive properties, could be used in polarization-

---

conversion as well as intensity-modulation applications [5]. In one of the two structures, which contains a quantum well that is under tensile strain, the TS structure, a change in an applied electric field will increase the refractive index seen by TM-polarized light significantly more than the refractive index seen by TE-polarized light. In the other structure, which contains a quantum well that is under compressive strain, the CS structure, the same change in applied electric field will decrease the refractive index seen by TE-polarized light significantly more than the refractive index seen by TM-polarized light. Because each of the structures primarily affects only one of the supported polarizations, and thereby only one of the modes, placing multiple repetitions of either structure in an optical waveguide can facilitate an electric-field-induced change in the polarization state of the output light for input light that contains both the fundamental TE and TM modes. At the output of the waveguide, the powers of the two modes must be matched in order to achieve switching between two orthogonal polarization states (*i.e.*, to achieve 90° polarization rotation). However, if multiple repetitions of both the TS and CS structures are placed in the optical waveguide of a modulator, the two structures can be made to provide an opposite-sign, and approximately equal-magnitude, change of the effective refractive indices for the two modes. Such a device, which we refer to as a quantum well polarization-conversion (QWPC) modulator, should provide push-pull type of polarization modulation, a mode of operation that is not typical for quantum well modulators and that will find use in an ever-increasing number of polarization-modulation applications [5]–[7].

Figures 3.1(a) and (b) illustrate the thicknesses and compositions of the layers in the TS and CS structures, respectively, as well as the direction of the applied electric field F [5]. By placing appropriate numbers of repetitions of these TS and CS structures, so as to give overlap factors of ~0.41 and ~0.22 for the fundamental TE and TM modes in a waveguide forming a QWPC modulator, respectively, a push-pull polarization conversion giving a small chirp parameter, *i.e.* $\alpha_H \approx 0.05$ [8], should be possible to achieve in a 3.0 mm long device when the electric field is switched from 20 to 25 kV/cm. This chirp would mainly be due to nonlinearities in the absorption and refractive index changes in the two structures [5].

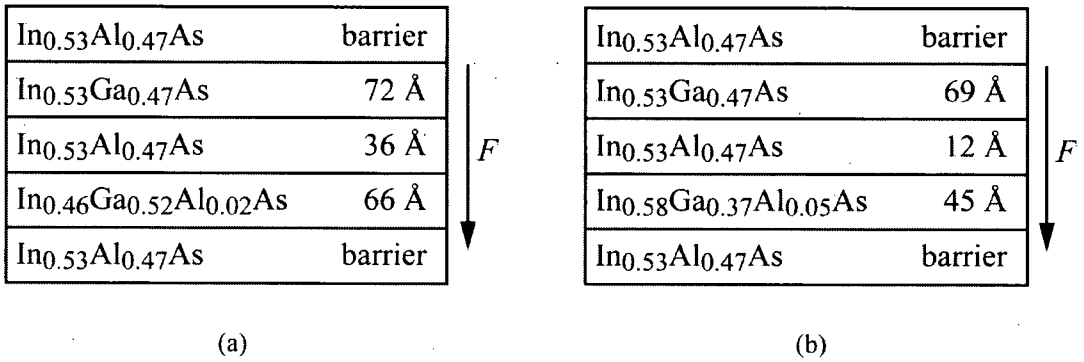

Figure 3.1: (a) TS structure containing a quaternary quantum well which is under ~0.50 % of tensile strain and (b) CS structure containing a quaternary quantum well which is under ~0.34 % of compressive strain.

3.2 Influence of Layer Variations

As the next step in developing the TS and CS structures for use in a QWPC modulator, we investigate how the electrorefractive properties of these structures depend on the thickness and compositional variations of their layers. The investigation reveals the trends and issues pertaining to the variations, and it indicates the design objectives for optimizing the performance of the structures. For each structure, the thickness of its unstrained quantum well, w_1, and the thickness of its strained quantum well, w_2, are varied by $\pm\Delta w_1$ and $\pm\Delta w_2$, respectively. The gallium mole fractions in both quantum wells, x_1 and x_2, are varied by the same amount, $\pm\Delta x$, and the aluminum mole fraction in the quaternary, strained quantum well, z_2, is varied by $\pm\Delta z$. Even when neglecting the compositional and thickness variations for the barriers in each structure, the remaining two thickness and three compositional variations necessitate 3^5 (=243) different simulations of each structure in order to obtain the statistical average absorptions and refractive indices of the two structures [4]. The statistical average responses, as figures of merit for the layer thickness and compositional variation effects on the TS and CS structures, are calculated as described below.

If in one of the variations of a structure, say structure i, x_1 is decreased by Δx, z_2 is increased by Δz, and w_2 is increased by Δw_2, the probability of its occurrence will be

$$P_i = (1 - p_{w1}^{+} - p_{w1}^{-})p_{x1}^{-}p_{w2}^{+}(1 - p_{x2}^{+} - p_{x2}^{-})p_{z2}^{+}. \tag{3.1}$$

Here, p_{w1}^{+} and p_{w1}^{-} are the probabilities of w_1 changing by $+\Delta w_1$ and $-\Delta w_1$, respectively, and p_{x1}^{-} is the probability of x_1 changing by $-\Delta x$. Similarly, p_{w2}^{+} and p_{z2}^{+} are the probabilities of w_2 and z_2 changing by $+\Delta w_2$ and $+\Delta z$, respectively, while p_{x2}^{+} and p_{x2}^{-} are the probabilities of x_2 changing by $+\Delta x$ and $-\Delta x$, respectively. In the rest of the discussion, we will assign the probability p_w to p_{w1}^{+}, p_{w1}^{-}, p_{w2}^{+}, and p_{w2}^{-}. Similarly, we will assign the probability p_c to p_{x1}^{+}, p_{x1}^{-}, p_{x2}^{+}, p_{x2}^{-}, p_{z2}^{+}, and p_{z2}^{-}. Also, the statistical average absorption at wavelength, λ, and electric field, F, of a structure for either polarization is calculated as

$$\overline{\alpha}_{\mathrm{pol(str)}}(\lambda, F) = \sum_{i=1}^{243} P_i \alpha_i^{\mathrm{pol(str)}}(\lambda, F), \tag{3.2}$$

where $\alpha_i^{\mathrm{pol(str)}}(\lambda, F)$ is the absorption for the ith structure for either polarization (pol = TE or TM) and structure (str = TS or CS) [4]. The statistical average refractive index for either polarization and structure, $\overline{n}_{\mathrm{pol(str)}}(\lambda, F)$, is obtained from $\overline{\alpha}_{\mathrm{pol(str)}}(\lambda, F)$ via the Kramers–Krönig relations, and both quantities are calculated relative to their values at F = 14 kV/cm, which is taken as the lower limit of the region of interest for the electric field.

3.2.1 TS Structure

The TS structure was first analyzed by allowing the thicknesses of its two quantum wells to change by ±5 % and allowing x in both wells and z in the strained well to change by ±0.02. At the wavelength of operation $\lambda = 1550$ nm and for electric fields between $F =$ 14 and 28 kV/cm, where the positive change of its refractive index for TM polarization $\Delta n_{TM(TS)}$ [5] is larger than the positive change of its refractive index for TE polarization $\Delta n_{TE(TS)}$ [5], Fig. 3.2(a) compares $\overline{n}_{TM(TS)}$ obtained for $p_c = 0$ and $p_w = 0$ ($\overline{n}_{TM(TS)}^{0,0}$) with $\overline{n}_{TM(TS)}$ obtained for $p_c = 0.10, 0.20, 0.33$ and $p_w = 0.33$. Similarly, Fig. 3.3(a) compares

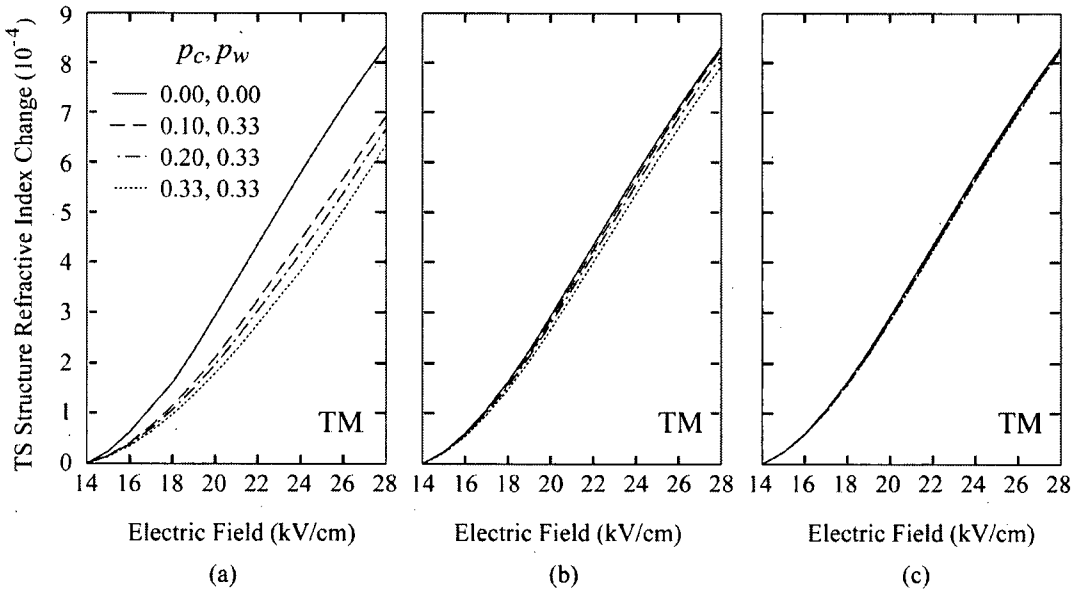

Figure 3.2: $\overline{n}_{TM(TS)}$ for (a) $\Delta w_1 = \pm 5\%$ of w_1, $\Delta w_2 = \pm 5\%$ of w_2, $\Delta x = \Delta z = \pm 0.02$, (b) $\Delta w_1 = \Delta w_2 = \pm 1$ Å, and $\Delta x = \Delta z = \pm 0.01$, and (c) $\Delta w_1 = \Delta w_2 = \pm 1$ Å, and $\Delta x = \Delta z = \pm 0.005$.

$\bar{n}_{TE(TS)}$ with $\bar{n}_{TE(TS)}^{0,0}$ for the same p_c and p_w values. $\bar{n}_{TM(TS)}^{0,0}$ and $\bar{n}_{TE(TS)}^{0,0}$ therefore represent the electric-field-induced refractive index changes of the nominally designed structure, when they are adjusted to be zero for F = 14 kV/cm, as shown in the two figures. In Fig. 3.2(a), the obtained $\bar{n}_{TM(TS)}$ curves behave similarly to $\bar{n}_{TM(TS)}^{0,0}$. This is not true for $\bar{n}_{TE(TS)}$ of Fig. 3.3(a), which is seen to have a pronounced zigzag pattern. The reason for this zigzag pattern is that the confinement of the lowest energy heavy-hole

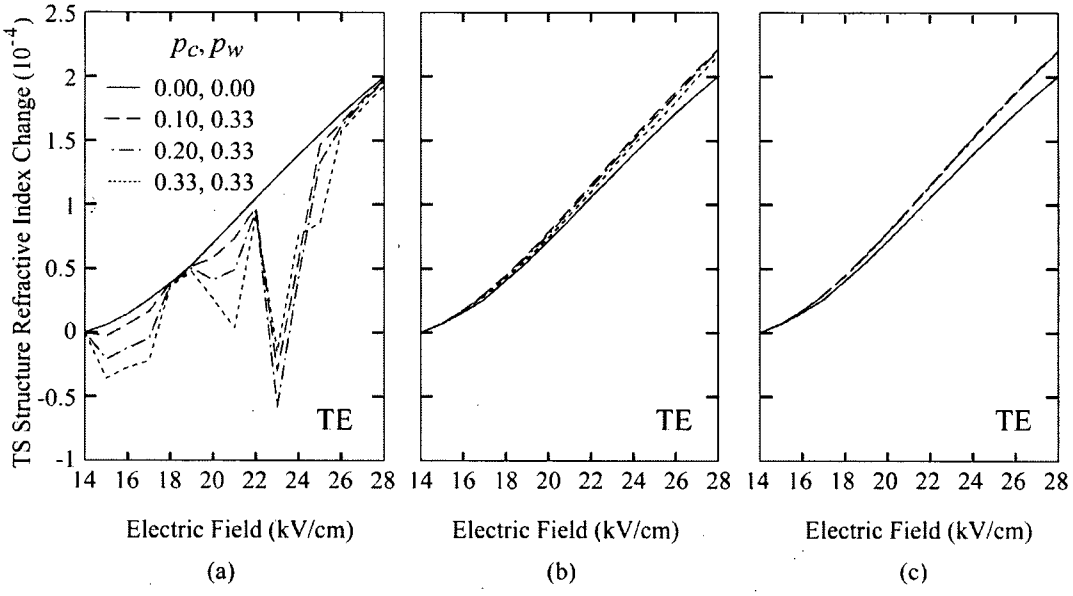

Figure 3.3: $\bar{n}_{TE(TS)}$ for the same variations as Fig. 3.2.

wave function (Ψ_{HH1}) [5] will be weakened for any structure variation that decreases the nominal depth or thickness of the unstrained well or increases the nominal depth or the thickness of the strained well. Ψ_{HH1} will, therefore, transfer to the strained well for lower values of the electric field than it would in the nominal structure contributing to a refractive index change for the TE polarization [9]. Due to the large heavy-hole mass and

the large thickness of the middle barrier, these Ψ_{HH1} transfers, *i.e.*, heavy-hole exciton anticrossings [1], [5] will occur for very small electric-field increments causing the rapid changes $\overline{n}_{TE(TS)}$. Fig. 3.3(a) does not capture all of the features of $\overline{n}_{TE(TS)}$ as the data in the figures have been obtained and plotted in 1 kV/cm increments in F.

Similar to Figs. 3.2(a) and 3.3(a), Figs. 3.2(b) and 3.3(b) show $\overline{n}_{TM(TS)}$ and $\overline{n}_{TE(TS)}$ for the same values of p_c and p_w except that now $\Delta w_1 = \Delta w_2 = \pm 1$ Å, $\Delta x = \pm 0.01$, and $\Delta z = \pm 0.01$. Even though, for these smaller variations, the refractive index for TM-polarized light changes less from its nominal value, the variations are still not small enough to eliminate the heavy-hole exciton anticrossings that contribute to $\overline{n}_{TE(TS)}$. However, here, the number of variations of the structure that result in the heavy-hole exciton anticrossings for the electric fields between $F = 14$ kV/cm and $F = 28$ kV/cm is smaller than in Fig. 3.3(a) so that none of the resulting zigzag features of the $\overline{n}_{TE(TS)}$ curves are captured. However, decreasing the compositional variations in the structure even further, [see Fig. 3.2(c) and Fig. 3.3(c)], so that $\Delta w_1 = \Delta w_2 = \pm 1$ Å, $\Delta x = \pm 0.005$, and $\Delta z = \pm 0.005$ does eliminate the zigzag pattern successfully and makes the $\overline{n}_{TM(TS)}$ and $\overline{n}_{TE(TS)}$ curves overlap almost entirely with the $\overline{n}_{TM(TS)}^{0,0}$ and $\overline{n}_{TE(TS)}^{0,0}$ curves. Here, the absence of the zigzag pattern in $\overline{n}_{TE(TS)}$ is real, and it is not an artifact of the sampling, as it was in Fig. 3.3(b). This is confirmed by simulating the most extreme variation of the structure, which is the one that gives the narrowest and shallowest unstrained well and

the widest and deepest strained well, and observing that Ψ_{HH1} does not transfer to the strained well for the electric fields of interest.

3.2.2 CS Structure

Similar to Figs. 3.2 and 3.3, Figs. 3.4 and 3.5, show $\overline{n}_{TE(CS)}$ and $\overline{n}_{TM(CS)}$ of the CS structure for the same well thickness and compositional variations. Compared to the TS

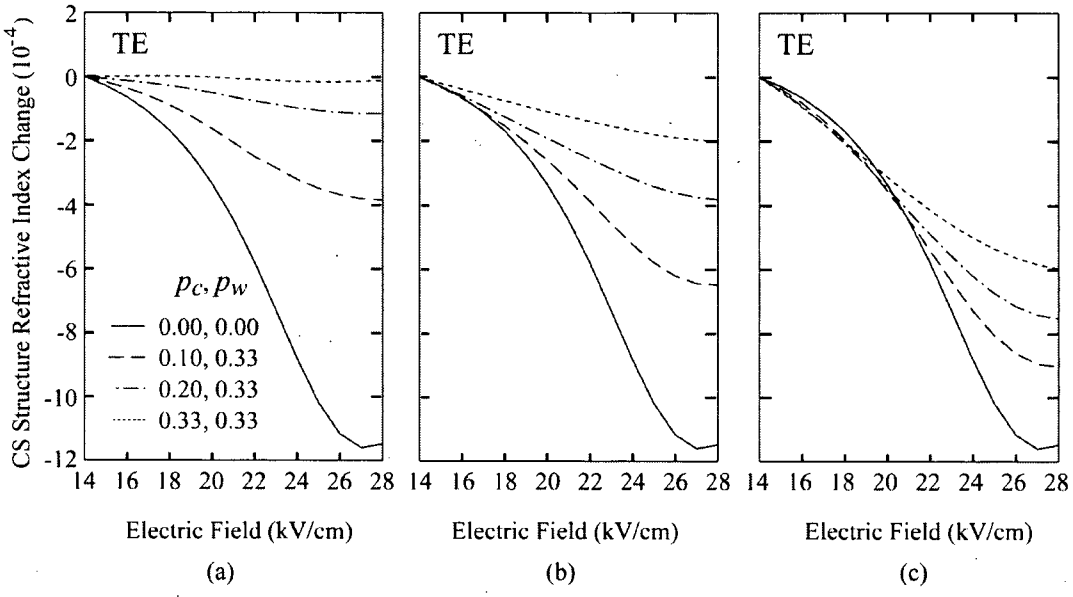

Figure 3.4: $\overline{n}_{TE(CS)}$ for the same variations as Fig. 3.2.

structure, $\overline{n}_{TE(CS)}$ for the CS structure deviates significantly from its nominal value, even for the smallest thickness and compositional variations, [see Fig. 3.4(c)]. The CS structure has a greater sensitivity to the compositional and thickness variations because the CS structure, for its operation, relies on the heavy holes, *i.e.*, the anticrossing of the

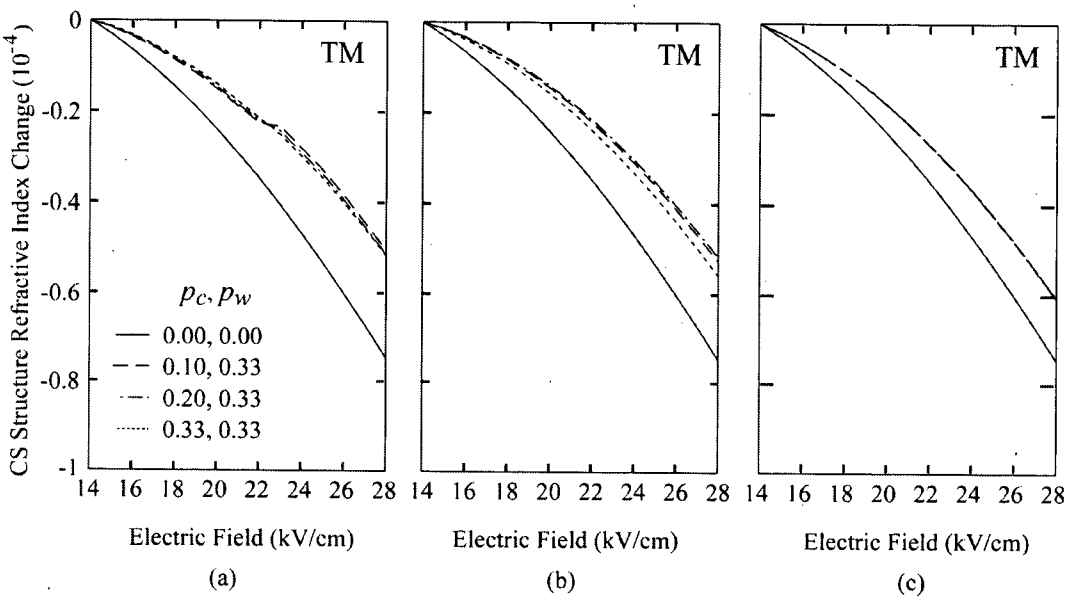

Figure 3.5: $\overline{n}_{TM(CS)}$ for the same variations as Fig. 3.2.

heavy-hole excitons, and the TS structure on the light holes, *i.e.*, the anticrossing of the light-hole excitons. The heavy holes, because of their greater mass, are closer to bottoms of the quantum wells and more susceptible to changes of the wells' compositions and widths. Also, the heavy-hole band edge (E_{HH}) and the conduction band edge (E_C) change more dramatically than the light-hole band edge (E_{LH}) when a variation in composition occurs [10]. For example, for the strained well of the CS structure, E_{LH} will change much less than E_{HH} and E_C when x is changed from its nominal value of 0.37. In fact, E_{LH} will increase (toward positive energies) by less than 1 meV when x is increased to 0.39. For the same change in x, E_{HH} will decrease by ~9 meV, and E_C will increase by ~7 meV. It is, therefore, not surprising that $\overline{n}_{TM(TS)}$ and $\overline{n}_{TM(CS)}$ show better performance than $\overline{n}_{TE(TS)}$ and $\overline{n}_{TE(CS)}$, both of which strongly depend on the behaviour of the heavy holes.

3.3 Discussion

In analyzing the TS and CS structures of Fig. 3.1, each of which could be used separately, or both of which could be combined to form a push-pull QWPC modulator, the electrorefractive properties of the TS structure prove to be less sensitive to the structure variations provided that it has been designed so that no variation of the structure allows the heavy-hole excitons to anticross. The electrorefractive properties of the TS structure will then barely deviate from their nominal values for compositional variations that are smaller than or equal to ~0.01 and for the well thickness variations of ~1 Å. This structure would be useful in any device requiring that upon the application of a (001) electric field the refractive index change for TM-polarized light be significantly greater than the refractive index change for TE-polarized light.

The current design of the CS structure is significantly more sensitive to small variations in thickness and composition than that of the TS structure. For example, considering the effect of a 1 Å thickness and 0.005 compositional variation on the performance of a QWPC modulator for all the different values of p_c and p_w used in the figures above, we find that as p_c increases from 0 to 0.10, 0.20, and 0.33 (again, here, $p_w = 0.33$ for all values of p_c except for the nominal structure, where they are both zero), the length of the

QWPC modulator needed to maintain a low drive electric field of 5 kV/cm increases from 3.0 mm to 3.7, 4.1, and 4.9 mm, respectively. Also, the chirp parameter corresponding to p_c =0.10, 0.20, and 0.33 will approximately increase to 1, 1.5, and 3, respectively. While we conclude that very tight control of the fabrication tolerances would be needed for the CS structure in a low-chirp QWPC modulator, this study has shown that a practical TS structure should be possible and provides the motivation for further investigation into the design of the CS structure.

References

[1] C. Thirstrup, "Refractive index modulation based on excitonic effects in GaInAs-InP coupled asymmetric quantum wells," *IEEE J. Quantum Electron.*, vol. 31, no.6, pp. 988–996, 1995.

[2] J. Khurgin, "Second-order nonlinear effects in asymmetric quantum-well structures," *Phys. Rev. B.*, vol. 38, no. 6, pp. 4056–4066, 1998.

[3] H. Mohseni, H. An, Z. A. Shellenbarger, M. H. Kwakernaak, and J. H. Abeles, "Enhanced electro-optic effect in GaInAsP–InP three-step quantum wells," *Appl. Phys. Lett.*, vol. 84, no. 11, pp. 1823–1825, 2004.

[4] K. Tada, T. Arakawa, K. Kazuma, N. Kurosawa, and J.-H. Noh, "Influence of one monolayer thickness variation in GaAs/AlGaAs five-layer asymmetric coupled quantum well upon electrorefractive index change,"

Jpn. J. Appl. Phys., vol. 40, no. 2A, pt. 1, pp. 656–661, 2001.

[5] S. Ristic and N. A. F. Jaeger, "Push–pull polarization conversion using novel asymmetric coupled quantum-well structures," *IEEE Photon. Technol. Lett.*, vol. 18, no. 2, pp. 316–318, 2006.

[6] F. Heismann, "Compact electro-optic polarization scramblers for optically amplified lightwave systems," *J. Lightw. Technol.*, vol. 14, no. 8, pp. 1801–1814, 1996.

[7] A. L. Campillo, "Interchannel nonlinear crosstalk in analog polarization modulated WDM systems," *J. Lightw. Technol.*, vol. 24, no. 3, pp. 1186–1193, 2006.

[8] G. L. Li and P. K. L. Yu, "Optical intensity modulators for digital and analog application," *J. Lightw. Technol.*, vol. 21, no. 9, pp. 2010–2030, 2003.

[9] R. Lang and K. Nishi, "Electronic state localization in semiconductor superlattices," *Appl. Phys. Lett.*, vol. 45, no. 1, pp. 98–100, 1984.

[10] S. L. Chuang, *Physics of Optoelectronic Devices.* New York: Wiley, 1995, pp. 154–157.

Chapter 4
Robust CQW Electrorefraction Modulator

4.1 Introduction

Similar to square quantum well (SQW) structures, coupled quantum well (CQW) structures have been studied for their use in both electroabsorption and electrorefraction (ER) modulators made in the InP and GaAs material systems [1]–[4]. Although, in ER modulators, the magnitude of the electric-field-induced refractive-index change achievable with CQW structures is similar to that achievable with SQW structures, CQW structures have the advantage that they exhibit no significant absorption modulation [1]. An additional advantage of CQW structures is that they provide the refractive-index

change for considerably lower applied electric field F (leading to much lower drive voltages in devices using them) [1]–[3]. Until now, CQW structures have had the disadvantage that they are typically very sensitive to layer thickness and compositional variations [2], [3], [5]. Here, we introduce an InGaAs/InAlAs CQW structure (structure #1) that is very robust to these layer thickness and compositional variations. To achieve this robustness, this structure has its ER effect based on the anticrossing of the lowest energy light-hole wave function (Ψ_{LH1}) with the second lowest energy light-hole wave function (Ψ_{LH2}) and, consequently, is more appropriate for use in transverse magnetic (TM) ER modulators [6]. We compare our structure to a similar InGaAs/InAlAs CQW structure (structure #2) that has its ER effect based on the anticrossing of the lowest energy electron wave function (Ψ_{E1}) with the second lowest energy electron wave function (Ψ_{E2}), and as such, the structure is more appropriate for use in transverse electric (TE) ER modulators [1]. In our comparison, we show that structure #1 has superior robustness, because its ER effect is based on the anticrossing of the light-hole wave functions. We also offer an explanation as to why designing an InGaAs/InAlAs CQW structure that has its ER effect based on the anticrossing of light holes rather than electrons, or heavy holes should provide for better robustness to layer thickness and compositional variations.

4.2 Influence of Layer Variations

In our model, the energy bands are obtained using the model-solid theory [7]. The absorption spectra are obtained using the variational method to solve the exciton equation in the effective-mass approximation [8]. The Lorentzian broadening function used in the model is described in [9], and the refractive-index changes are obtained using the Kramers–Krönig relation [1]. Our model is very similar to that used in [3] and [10] except that, in our model, the refractive-index changes are obtained for a whole period of a CQW structure and not only for the quantum well layers.

Fig. 4.1(a) illustrates Ψ_{E1}, Ψ_{E2}, Ψ_{LH1}, Ψ_{LH2}, and the two lowest energy heavy-hole wave functions (Ψ_{HH1} and Ψ_{HH2}), as well as the band-edge diagram of structure #1 for F = 0, 15, and 35 kV/cm. The structure has $In_{0.52}Al_{0.48}As$ barriers and $In_{0.53}Ga_{0.47}As$ wells, both of which are lattice-matched to (001) InP. The thickness of each of the two external barriers is 90 Å, while the thickness of the middle barrier is 27 Å. The thicknesses of the left-hand side well (QW1) and the right-hand side well (QW2) are 72 and 60 Å, respectively (*i.e.*, structure #1 is a 90-72-27-60-90 structure).

As shown in Fig. 4.1(a), for F = 0 kV/cm, Ψ_{LH1} and Ψ_{E1} will be mainly localized in the wider QW1, while Ψ_{LH2} and Ψ_{E2} will be mainly localized in the narrower QW2. As F is

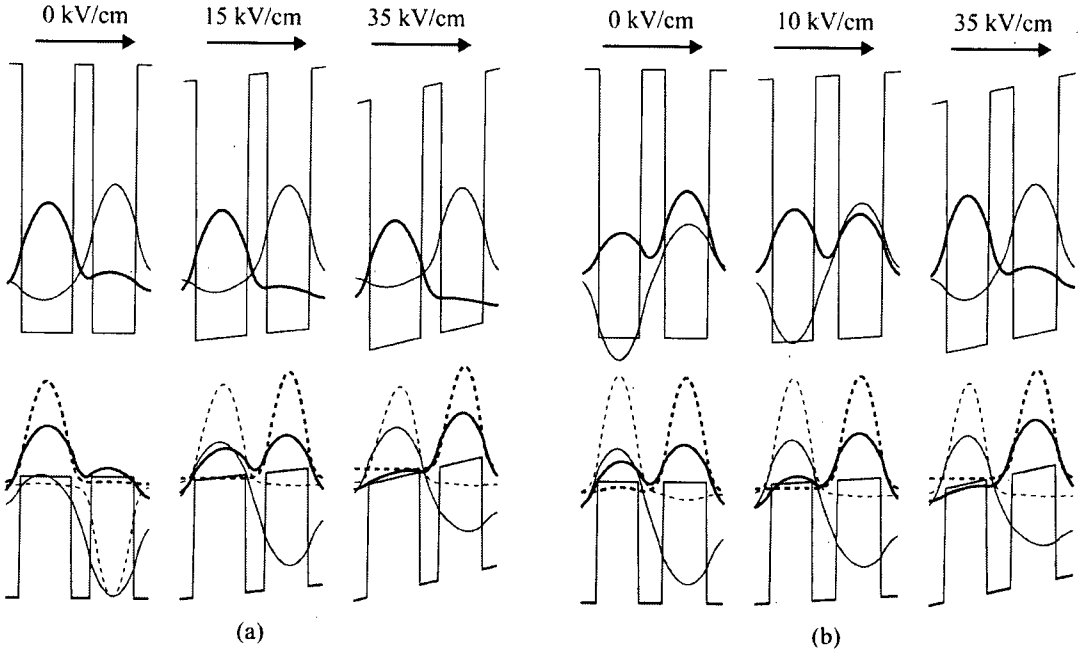

Figure 4.1: Energy band diagram of structure #1 and Ψ_{E1} and Ψ_{E2}, Ψ_{LH1} and Ψ_{LH2}, and Ψ_{HH1} and Ψ_{HH2} for $F = 0$, 15, and 35 kV/cm. Here, the size of the band gap and the thicknesses of the external barriers are not shown to scale. Ψ_{HH1} is shown as dashed thick line, while Ψ_{HH2} is shown as dashed thin line. Ψ_{E1} and Ψ_{LH1} are shown as full thick lines, while Ψ_{E2} and Ψ_{LH2} are shown as full thin lines. (b) Analogously, band diagram and wave functions of structure #2 for $F = 0$, 10, and 35 kV/cm.

increased to 15 kV/cm, Ψ_{LH1} and Ψ_{LH2} will become approximately equally distributed between the two wells, while Ψ_{E1} and Ψ_{E2} will become more strongly localized to the same wells as they were previously. As F is further increased to 35 kV/cm, Ψ_{LH1} will switch to QW2 and Ψ_{LH2} will switch to QW1, while Ψ_{E1} and Ψ_{E2} will be yet more strongly localized to their respective wells. Similar to [6], here, the electric field at which the anticrossing of Ψ_{LH1} and Ψ_{LH2} occurs is called the resonant electric field for the light holes F_{LH} (below, we will also use F_E for the resonant electric field for the electrons). For structure #1, $F_{LH} \approx 15$ kV/cm. Consequently, above F_{LH}, the electric-field-induced

refractive-index change for the TM polarization (Δn_{TM1}) will have a smooth positive slope and the electric-field-induced refractive-index change for the TE polarization (Δn_{TE1}) will also have a smooth positive, although considerably smaller, slope [6] as shown in Fig. 4.2. Here, Δn_{TE1} and Δn_{TM1} (shown relative to their zero-electric-field values) are plotted for $\lambda = 1550$ nm and the energy separation between Ψ_{E1} and Ψ_{LH1}

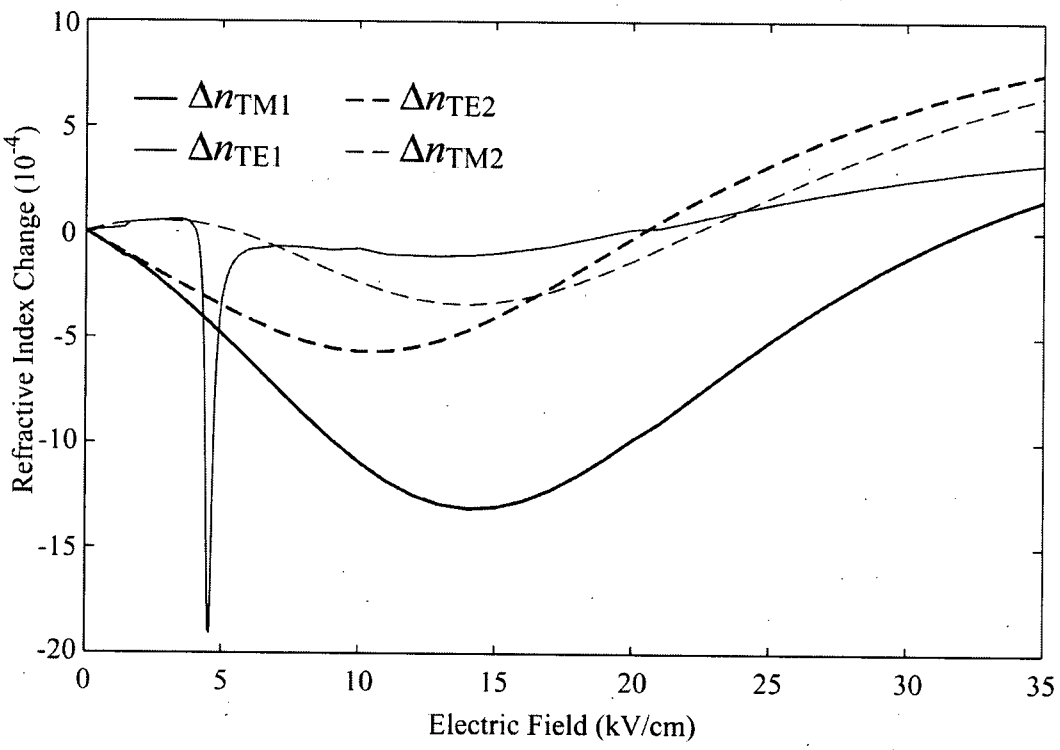

Figure 4.2: Structure #1 and structure #2 refractive-index changes for TE and TM polarizations.

corresponds to $\lambda = 1402$ nm for $F = 0$ kV/cm. Below F_{LH}, Δn_{TM1} and Δn_{TE1} will have smooth negative slopes except at $F \approx 4.5$ kV/cm, where there is a large dip in Δn_{TE1}. The dip is due to the anticrossing of Ψ_{HH1} and Ψ_{HH2} at $F_{HH} \approx 4.5$ kV/cm, and it does not appear in Δn_{TM1} as the heavy-hole momentum matrix element is zero for TM light. The

dip is very sharp because of the large effective masses of Ψ_{HH1} and Ψ_{HH2} and the relatively large thickness of the middle barrier [10].

Analogous to structure #1, structure #2 is a 90-51-30-54-90 lattice-matched structure, and its wave functions and the band-edge diagram are shown in Fig. 4.1(b) for $F = 0$, 10, and 35 kV/cm. Unlike structure #1, which is designed for modulation of TM light via the anticrossing of Ψ_{LH1} and Ψ_{LH2}, structure #2 is designed for modulation of TE light via the anticrossing of Ψ_{E1} and Ψ_{E2} ($F_E \approx 10$ kV/cm), while all other wave functions remain localized to their respective wells for the electric fields of interest. In structures of this type, the refractive-index change for TE light is somewhat larger than the refractive-index change for TM light and the structures are, therefore, better suited for use in TE modulators [1]. Here, Δn_{TE2} and Δn_{TM2} (shown relative to their zeroelectric-field values) are also plotted for $\lambda = 1550$ nm and the energy separation between Ψ_{E1} and Ψ_{HH1} corresponds to $\lambda = 1395$ nm for $F = 0$ kV/cm. Note: For the purpose of comparison, structure #1 and structure #2 were designed to have similar magnitudes of Δn_{TM1} and Δn_{TE2} above their corresponding resonant fields and similar resonant fields for light holes and electrons and, furthermore, they were designed to have nearly equal wavelength detunings of their lowest energy anticrossing wave functions from the wavelength of operation ($\lambda = 1550$ nm), which should yield similar absorption coefficients at the wavelength of operation.

To compare sensitivities to the layer variations, in each structure, the thicknesses of the two quantum wells and the middle barrier are changed by ±3 Å. In [3], it is shown that even such small thickness variations can significantly modify the distributions of wave functions in CQW structures and, in turn, influence the absorption spectra and the refractive-index changes in these structures. Similarly, the InAs mole fractions in the three barriers and each quantum well are changed by ±0.02. Treating the compositional and thickness variations separately amounts to 3^5(= 243) compositional and 3^3(= 27) thickness variations of each of the two structures. Each thickness variation is assigned the same occurrence probability of 1/27, and similarly, each compositional variation is assigned the same occurrence probability of 1/243. The refractive-index changes for either polarization corresponding to each of the variations are multiplied by the probability of the variation's occurrence and then added together in a statistical average, which is, again, obtained separately for the thickness and the compositional variations. Prior to any variations of structure #1, Δn_{TM1} is plotted as $\Delta n_{\mathrm{TM1}}{}^{O}$ in Fig. 4.3(a) relative to its value at F = 25 kV/cm for electric fields between F_{LH} and F = 35 kV/cm. The average refractive-index changes for the thickness variations ($\Delta n_{\mathrm{TM1}}{}^{T}$) and for the compositional variations ($\Delta n_{\mathrm{TM1}}{}^{C}$) are also plotted in Fig. 4.3(a). Similarly, Fig. 4.3(b) shows the corresponding curves for Δn_{TE2} for structure #2 as $\Delta n_{\mathrm{TE2}}{}^{O}$, $\Delta n_{\mathrm{TE2}}{}^{T}$, and $\Delta n_{\mathrm{TE2}}{}^{C}$, respectively. It is shown in Fig. 4.3(b) that there will be certain variations (only compositional variations for this particular design of structure #2) that will allow Ψ_{HH1} and Ψ_{HH2} to anticross in the electric-field region of interest, which creates the sharp dip

shown in the TE curve (the data in Fig. 4.3 are obtained and plotted in 1 kV/cm increments of F, which has resulted in loss of detail as regards the features of this dip).

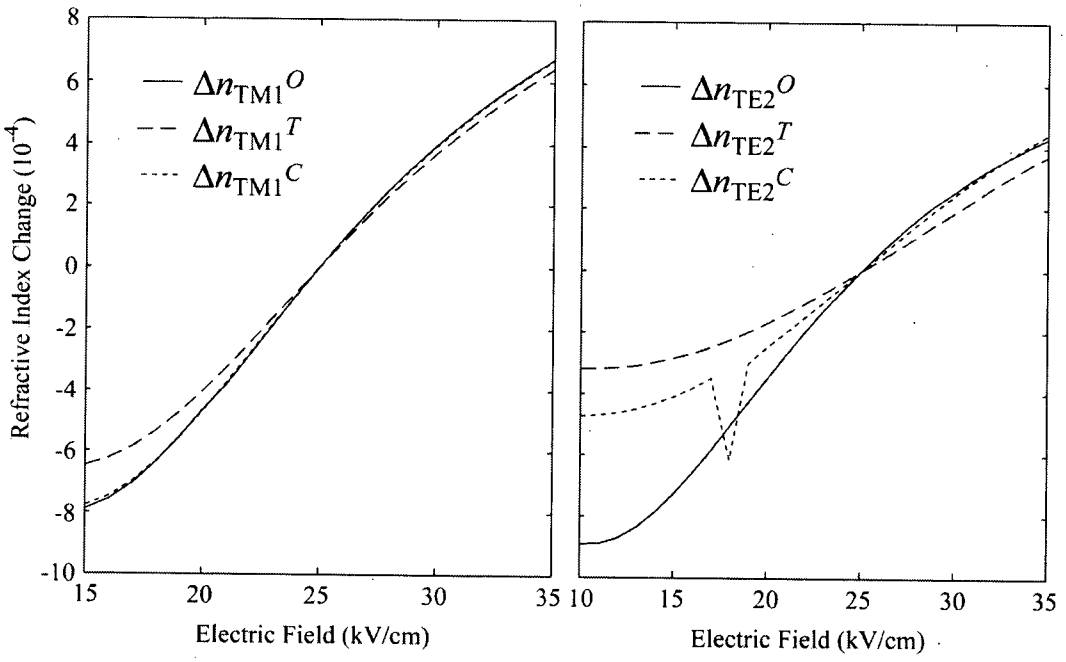

Figure 4.3: (a) Dependence of structure #1 refractive-index changes for TE and TM polarizations on the thickness and the compositional variations and (b) the same for structure #2.

Even ignoring the heavy-hole anticrossings, it is clear from Fig. 4.3 that Δn_{TM1} is less sensitive to both thickness and compositional variations than Δn_{TE2}. Here, $\Delta n_{TM1}{}^{O}$ and $\Delta n_{TM1}{}^{C}$ are practically indistinguishable for all electric fields, which means that structure #1 shows practically no sensitivity to the compositional variations. The same cannot be said for structure #2, as in the region of the greatest slope of $\Delta n_{TE2}{}^{O}$ (15 kV/cm $\leq F \leq$ 25 kV/cm), $\Delta n_{TE2}{}^{O} = 7.3 \times 10^{-4}$, and it is ~77 % larger than $\Delta n_{TE2}{}^{C}$. Structure #1 is also far less sensitive to the thickness variations than structure #2. In the region of the greatest

slope of $\Delta n_{TM1}{}^{O}$ (20 kV/cm $\leq F \leq$ 30 kV/cm), $\Delta n_{TM1}{}^{O} = 8.7 \times 10^{-4}$, and it is only ~11 % larger than $\Delta n_{TM1}{}^{T}$, whereas in the region of the greatest slope of $\Delta n_{TE2}{}^{O}$, $\Delta n_{TE2}{}^{O}$ is ~157 % larger than $\Delta n_{TE2}{}^{T}$. Above $F \approx 25$ kV/cm, Δn_{TE2} does not seem greatly influenced by the variations, however, its slope in this region is considerably smaller than its maximum slope.

The use of decoupled random variations of the layer thicknesses and compositions is intended to illustrate the robustness of structure #1 to such variations, but it is not intended to model any specific growth process. The main reason for the smaller sensitivity of structure #1 to thickness variations is that the barriers confining the anticrossing Ψ_{LH1} and Ψ_{LH2} in structure #1 are significantly lower than the barriers confining the anticrossing Ψ_{E1} and Ψ_{E2} in structure #2. When close to their respective resonances, Ψ_{LH1} and Ψ_{LH2} are thus spread out over a larger region in space than Ψ_{E1} and Ψ_{E2}, and Ψ_{LH1} and Ψ_{LH2} are less influenced by small thickness variations of the quantum well layers because they overlap less with these layers. For the same reason, any compositional variations will also have a smaller effect on Ψ_{LH1} and Ψ_{LH2} in structure #1 than they will on Ψ_{E1} and Ψ_{E2} in structure #2. Our simulations show that InGaAs/InAlAs CQW structures based on the anticrossing of Ψ_{HH1} and Ψ_{HH2} [6], [11] do not benefit from the small valence band discontinuity ratio to the extent that structure #1 does, because the effective masses of Ψ_{HH1} and Ψ_{HH2} are much larger than those of Ψ_{LH1} and Ψ_{LH2} and, thus, Ψ_{HH1} and Ψ_{HH2} are very sensitive to layer variations [5]. Also, even though the light

holes have larger effective masses than the electrons, their reduced localizations make them less sensitive to the layer variations. Another reason for the smaller sensitivity of structure #1 to thickness variations is that its quantum wells are thicker than those in structure #2 so that the ±3 Å thickness variations represent smaller percentage changes to the thicknesses of the quantum wells in it. In order for structure #1 and structure #2 to have similar wavelength detunings, structure #1 has to have thicker quantum wells because the energy separation between Ψ_{LH1} and Ψ_{E1} is larger than that between Ψ_{HH1} and Ψ_{E1} in lattice-matched CQW structures. In addition to the benefit that small valence band discontinuity ratio has on the sensitivity of structure #1 to compositional variations, these variations will have considerably smaller effects on the energy levels of the light-hole band edge than they will on the energy levels of the electron or the heavy-hole band edges because of the opposite-sign contributions of the hydrostatic and the shear strain components to the light-hole band edge [7].

Any wave function in a CQW structure will be far less sensitive to the layer variations when it is strongly localized to one of the two wells, as opposed to when it is approximately equally shared by both of the wells [5], which is the case when it is close to resonance and anticrossing with its counterpart of opposite symmetry. Consequently, for the electric fields of interest for structure #1, the variations will have very small effects on the otherwise sensitive Ψ_{E1}, Ψ_{E2}, Ψ_{HH1}, and Ψ_{HH2} as they are strongly localized. This is unlike other CQW structures that have the disadvantage of basing their ER effects

on anticrossing of either Ψ_{E1} and Ψ_{E2} or Ψ_{HH1} and Ψ_{HH2}, rather than the insensitive Ψ_{LH1} and Ψ_{LH2}.

References

[1] C. Thirstrup, "Refractive index modulation based on excitonic effects in GaInAs-InP coupled asymmetric quantum wells," *IEEE J. Quantum Electron.*, vol. 31, no.6, pp. 988–996, 1995.

[2] J.-H. Noh, S. Hasegawa, T. Suzuki, T. Arakawa, K. Tada, and H. Asahi, "Migration-enhanced epitaxy (MEE) growth of five-layer asymmetric coupled quantum well (FACQW) and its cross-sectional STM observation," *Physica E*, vol. 23, no. 3/4, pp. 482–486, 2004.

[3] K. Tada, T. Arakawa, K. Kazuma, N. Kurosawa, and J.-H. Noh, "Influence of one monolayer thickness variation in GaAs/AlGaAs five-layer asymmetric coupled quantum well upon electrorefractive index change," *Jpn. J. Appl. Phys.*, vol. 40, no. 2A, pt. 1, pp. 656–661, 2001.

[4] T. H. Stievater,W. S. Rabinovich, P. G. Goetz, R. Mahon, and S. C. Binari, "A surface-normal coupled-quantum-well modulator at 1.55 μm," *IEEE Photon. Technol. Lett.*, vol. 16, no. 9, pp. 2036–2038, 2004.

[5] R. Lang and K. Nishi, "Electronic state localization in semiconductor superlattices," *Appl. Phys. Lett.*, vol. 45, no. 1, pp. 98–100, 1984.

[6] S. Ristic and N. A. F. Jaeger, "Push–pull polarization conversion using novel asymmetric coupled quantum-well structures," *IEEE Photon. Technol. Lett.*, vol. 18, no. 2, pp. 316–318, 2006.

[7] M. P. C. M. Krijn, "Heterojunction band offsets and effective masses in III–V quaternary alloys," *Semiconduct. Sci. Technol.*, vol. 6, pp. 27–31, 1991.

[8] S. L. Chuang, *Physics of Optoelectronic Devices.* New York: Wiley, 1995, pp. 561–566.

[9] N. Susa, "Electric-field-induced refractive index changes in InGaAs/InAlAs asymmetric coupled quantum wells," *IEEE J. Quantum Electron.*, vol. 31, no. 1, pp. 92–100, 1995.

[10] T. Arakawa, K. Tada, N. Kurosawa, and J.-H. Noh, "Anomalous sharp dip of large field-induced refractive index change in GaAs/AlGaAs five-layer asymmetric coupled quantum well," *Jpn. J. Appl. Phys.*, vol. 39, no. 11, pp. 6329–6333, 2000.

[11] S. Ristic and N. A. F. Jaeger, "Influence of layer thickness and compositional variations on the electrorefractive properties of a quantum well polarization-conversion modulator," *J. Vac. Sci. Technol. A, Vac. Surf. Films*, vol. 24, no. 4, pp. 962–965, 2006.

Chapter 5
Improving Robustness in CQW Structures

5.1 Introduction

The coupled quantum well (CQW) structures used in electrorefraction (ER) and electroabsorption (EA) modulators can offer lower drive electric fields, *i.e.*, lower drive voltages, than the square quantum well (SQW) structures typically used in these devices [1], [2]. Increasing the thickness of the middle barrier separating the two quantum wells in a CQW structure can be used to further increase the sensitivities of the structure's electronic states to changes in the applied electric field, F, leading to lower drive voltages [3]. However, it has been shown that increasing the thickness of the middle barrier

---

A version of this chapter will be submitted for publication. S. Ristic and N. A. F. Jaeger, "Improving robustness to layer thickness and compositional variations of coupled quantum well structures," *J. Vac. Sci. Technol. A-Vacuum, Surfaces, and Films.*

increases the sensitivity of the electronic states to any thickness and compositional variations that may occur in the quantum well layers during the growth process [4], and the operation of devices using CQW structures can, therefore, be seriously compromised. Conversely, the middle barrier in CQW structures used in modern EA modulators is quite thin, and the potential of CQW structures to provide very low drive voltages is not fully realized [2]. In this article, we show how decreasing the depth of the quantum wells and simultaneously increasing the thickness of the middle barrier in a CQW structure can be used to reduce the sensitivities of the electronic states to the layer variations without sacrificing their sensitivities to changes in *F*.

5.2 Robustness improvement approach

The CQW structure of interest here, structure S_A, is lattice-matched and contains two 51 Å $In_{0.53}Ga_{0.47}As$ wells that are separated by a 30 Å $In_{0.52}Al_{0.48}As$ middle barrier and enclosed by 90 Å $In_{0.52}Al_{0.48}As$ external barriers. The energy difference between the wells and the barriers in the conduction band is $\Delta E_C = 481$ meV [5]. The electron effective mass used in the wells and the barriers is $m_c^* / m_0 = 0.0427 + 0.0328 / 0.48 \times z$, where z represents the Al mole fraction in $In_{(1-z-y)}Al_zGa_yAs$ [6]. The ground state electron wave function, Ψ_E, in the CQW structure is obtained by solving the one-dimensional, single-particle, time-independent Schrödinger equation using the transfer matrix method [7]. In order to make sure that the results presented here are not influenced by the

particular method of solving the Schrödinger equation, the results have also been confirmed using the finite-difference method [8], where S_A is enclosed in a larger quantum well with infinite barriers.

Fig. 5.1(a) shows S_A and Ψ_E for $F = 0$ kV/cm before (full lines) and after (dashed lines) the thickness of the left-hand side well (t_{w1}) has been increased by 3 Å. Before the increase in t_{w1}, Ψ_E will be equally distributed between the two wells because S_A is a

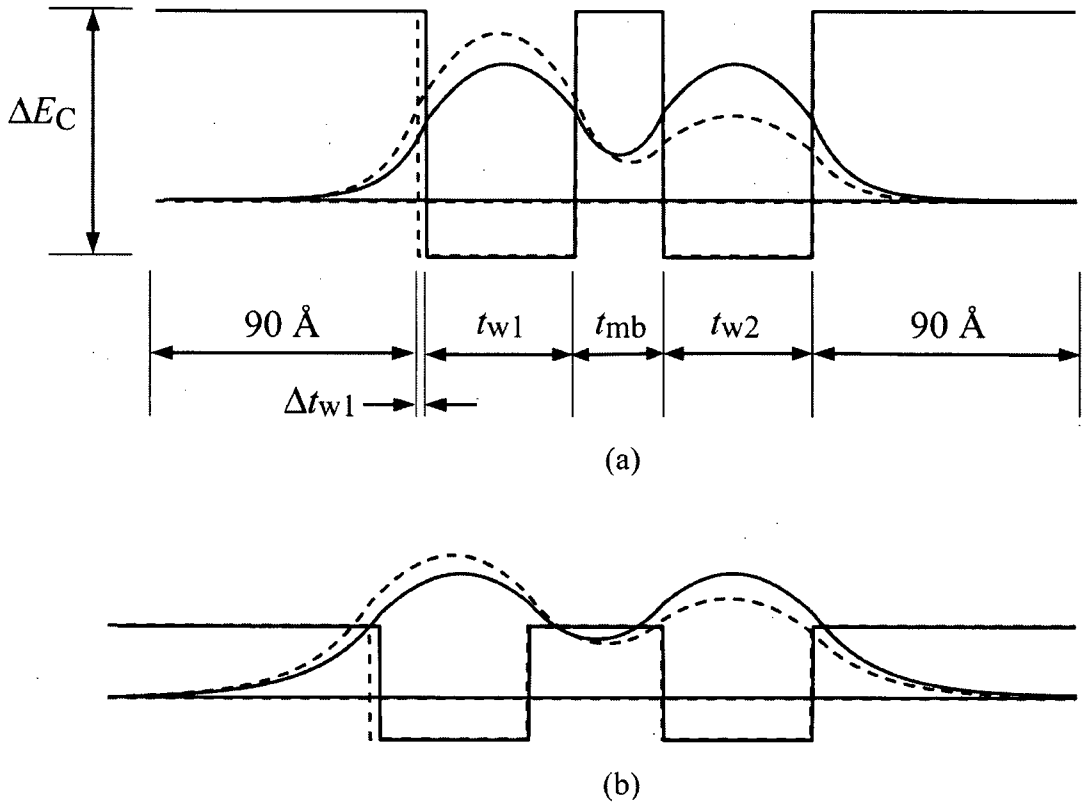

Figure 5.1: (a) S_A structure and its electron ground state wave function shown for $F =$ 0 kV/cm before (full lines) and after (dashed lines) the thickness of the left-hand side well is increased by 3 Å and (b) same for S_B structure.

symmetric structure. After the increase in t_{w1}, Ψ_E will be more strongly localized to the wider well. One way of quantifying the localization of Ψ_E in one of the two wells is to use the "localization parameter" P [4] which is defined as $P = (p_1 - p_2) / (p_1 + p_2)$, where p_1 and p_2 are the probabilities of finding the ground state electron in the left-hand side well and the right-hand side well, respectively. For example, in Fig. 5.1(a), for Ψ_E, $P = 0$ before the increase in t_{w1} and $P = 0.60$ after the increase in t_{w1}.

Fig. 5.1(b) shows how Ψ_E responds to a 3 Å change in t_{w1} for $F = 0$ kV/cm after the heights of the barriers have been decreased to $\Delta E_C = 219$ meV (*i.e.*, for $In_{0.52}Al_{0.24}Ga_{0.24}As$ lattice-matched barriers), and the thickness of the middle barrier (t_{mb}) has been increased to 46 Å. This new structure is labeled S_B. It is clear from Fig. 5.1(b) that the localization of Ψ_E does not change as much in S_B as it does in S_A for the same change in t_{w1} for $F = 0$ kV/cm; now P changes from 0 to 0.37. Furthermore, the larger thickness of the shorter middle barrier in S_B causes the localization of Ψ_E in S_B to have the same response to changes in F as the localization of Ψ_E in S_A does, as shown in Fig 5.2. This behaviour is both interesting and useful.

In Fig. 5.2, the electric-field dependences of localizations of Ψ_E in S_A and Ψ_E in S_B are illustrated by plotting the values of P for S_A and S_B, respectively. The two curves are practically indistinguishable for all values of F. In a similar fashion, it is also shown in Fig. 5.2 that Ψ_E in S_B is less sensitive to a 3 Å thickness variation ($\Delta t_{w1} = +3$ Å) than Ψ_E

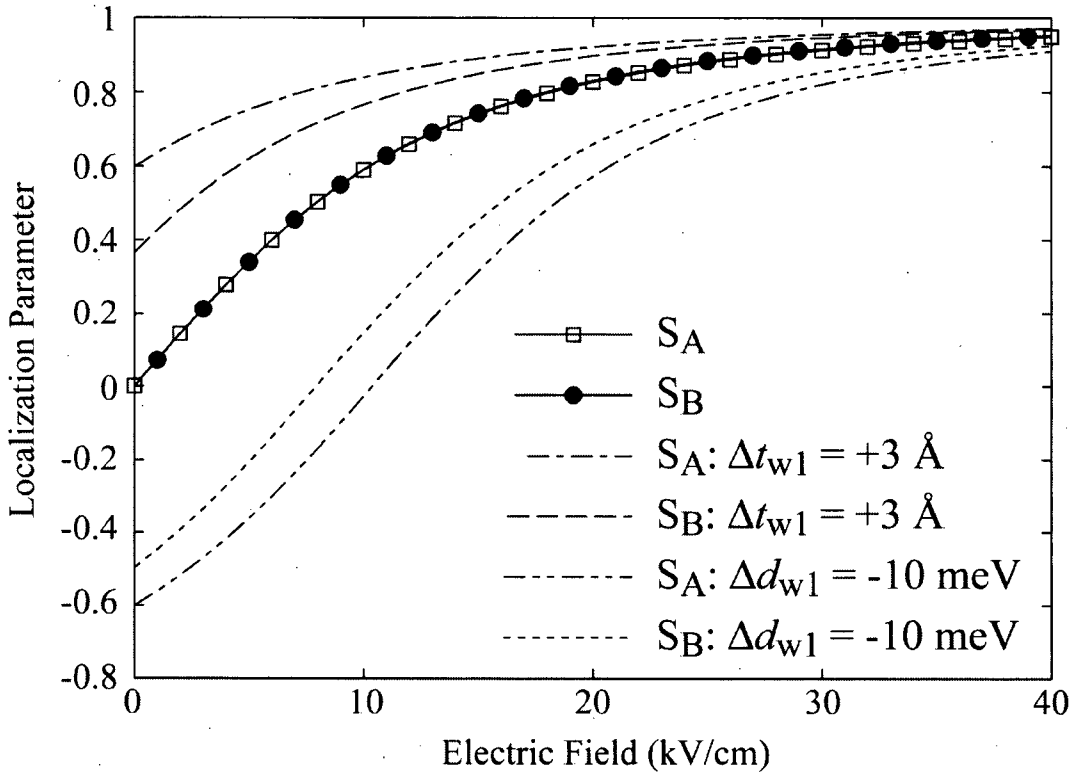

Figure 5.2: Localization parameters corresponding to structures S_A and S_B for a 3 Å increase of the thickness and a 10 meV decrease of the depth of the left-hand side well.

in S_A is, for all values of F. In addition, the remaining two curves in Fig. 5.2 show that Ψ_E in S_B will also be less susceptible to changes in the depth of the quantum wells. Here, the depths of the left-hand side wells in S_A and S_B have been decreased by 10 meV (Δd_{w1} = -10 meV) by making the wells out of quaternary compounds, here $In_{0.52}Al_{0.01}Ga_{0.46}As$ wells. Compared to Ψ_E in S_A, Ψ_E in S_B is less sensitive to thickness and compositional variations in the quantum wells because the barriers in S_B are shorter than the barriers in S_A. Consequently, Ψ_E will be located in the external barriers to a greater extent, see Fig

5.1(b), and it will be less influenced by any changes that occur in the quantum wells, while still providing the same response to the applied field.

Fig. 5.3 shows that similar changes to the thicknesses and compositions of the middle barriers in S_A and S_B will have smaller effects on Ψ_E than the changes in the quantum

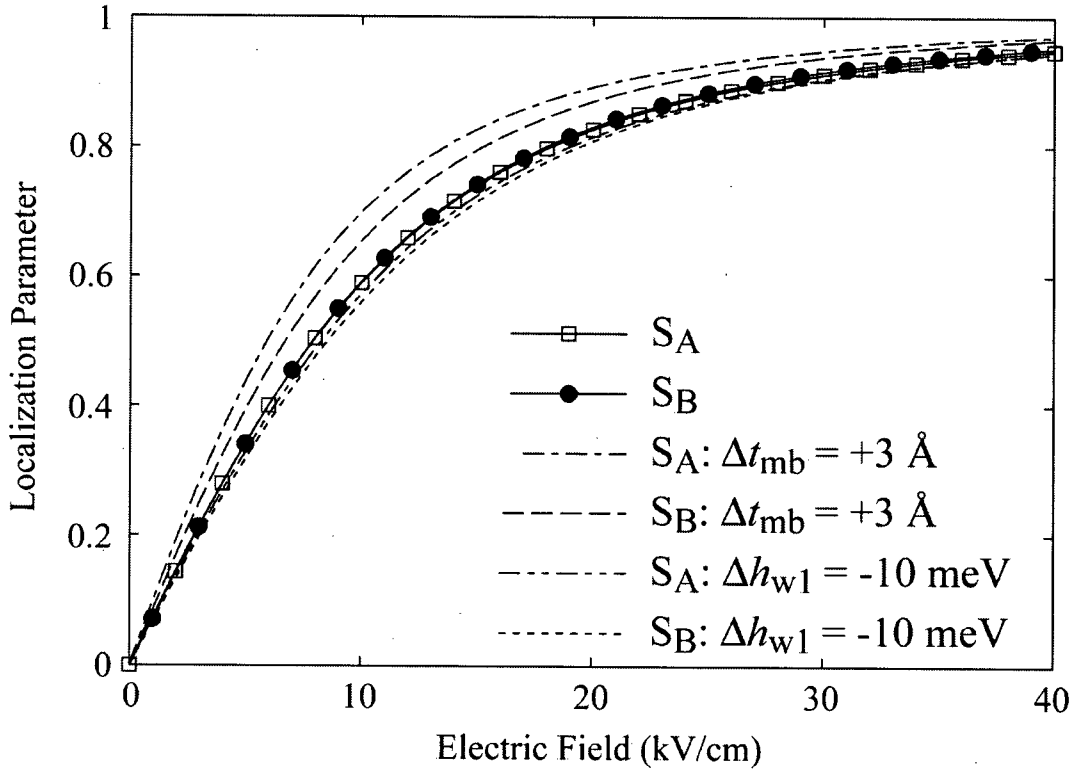

Figure 5.3: Localization parameters corresponding to structures S_A and S_B for a 3 Å increase of the thickness and a 10 meV decrease of the height of the middle barrier.

wells do. Here, the thicknesses of the middle barriers are increased by 3 Å (Δt_{mb} = +3 Å), and S_B, with its thicker barrier, performs somewhat better than S_A. When the heights of the middle barriers are decreased by 10 meV (Δh_{mb} = -10 meV), the effects on Ψ_E are

even smaller. Here, S_A performs better than S_B, but only slightly, when the middle barriers are $In_{0.52}Al_{0.47}Ga_{0.01}As$ and $In_{0.52}Al_{0.23}Ga_{0.25}As$, respectively. Lastly, Fig. 5.4 shows that decreasing the height of the left-hand side external barrier by 10 meV (Δh_{lb} = -10 meV) will also have small effects on Ψ_E in S_A and Ψ_E in S_B. Here, S_A again performs

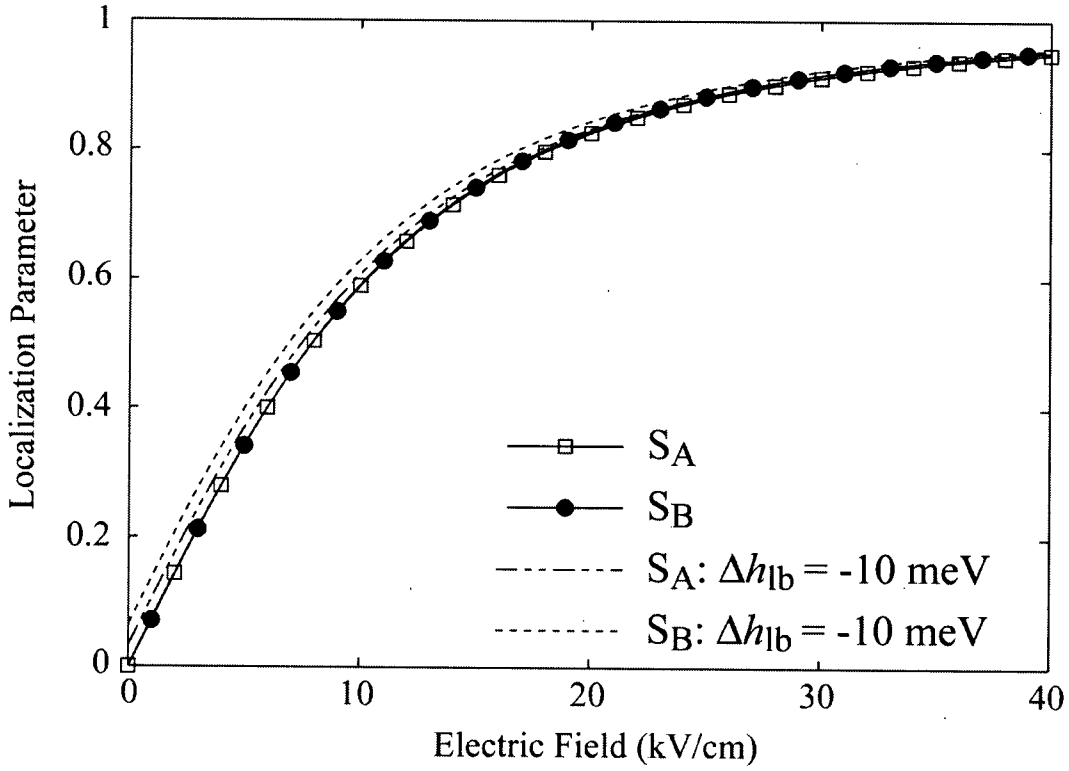

Figure 5.4: Localization parameters corresponding to structures S_A and S_B for a 10 meV decrease of the height of the left-hand side barrier.

only slightly better, and that is because the probability of finding Ψ_E in the in the external barriers is lower for S_A. Nevertheless, these marginally increased sensitivities of S_B to the compositional variations in the middle and external barriers by no means outweigh the

benefits of the structure's decreased sensitivities to the remaining possible layer variations.

5.3 Discussion

We have presented insights that form a basis for developing CQW structures that are robust to growth processes. As modern growth processes are becoming increasingly capable of achieving tight control of quaternary compounds [9], the approach to the design of CQWs should, in turn, allow the design of efficient ER and EA modulators.

References

[1] H. Feng, J. P. Pang, M. Sugiyama, K. Tada, Y. Nakano, "Field-induced optical effect in a five-step asymmetric coupled quantum well with modified potential," *IEEE J. Quantum Electron.*, vol. 34, no. 7, pp. 1197–1208, 1998.

[2] T. H. Stievater, W. S. Rabinovich, P. G. Goetz, R. Mahon, and S. C. Binari, "A surface-normal coupled-quantum-well modulator at 1.55 μm," *IEEE Photon. Technol. Lett.*, vol. 16, no. 9, pp. 2036–2038, 2004.

[3] C. Thirstrup, "Refractive index modulation based on excitonic effects in GaInAs–InP coupled asymmetric quantum wells," *IEEE J. Quantum Electron.*, vol. 31, no.6, pp. 988–996, 1995.

[4] R. Lang and K. Nishi, "Electronic state localization in semiconductor superlattices," *Appl. Phys. Lett.*, vol. 45, no. 1, pp. 98–100, 1984.

[5] M. P. C. M. Krijn, "Heterojunction band offsets and effective masses in III–V quaternary alloys," *Semicond. Sci. Technol.*, vol. 6, no. 1, pp. 27–31, 1991.

[6] S. L. Chuang, *Physics of Optoelectronic Devices.* New York: Wiley, 1995, pp. 710.

[7] S. L. Chuang, *Physics of Optoelectronic Devices.* New York: Wiley, 1995, pp. 157–160.

[8] K. Kawano, and T. Kitoh, *Introduction to optical waveguide analysis: solving Maxwell's equations and the Schrodinger equation.* New York: Wiley, 2001, pp. 253–254.

[9] C. Ebert, A. Bond, J. Levkoff, J. Seiler, and C. Wanamaker, "MOCVD process modeling using in-situ reflectance test structure measurements for process control improvement," in *Proc. IPRM (International Conference on Indium Phosphide and Related Materials)*, 2005, pp. 219–222.

Chapter 6
Improved Push-Pull CQW Polarization Modulator

6.1 Introduction

Traditionally associated with $LiNbO_3$ or GaAs modulators based on the linear electro-optic effect, polarization modulation has been used to improve the performance of both digital and analog optical communication systems [1]. Recently, we proposed a push-pull polarization-modulation scheme using InGaAlAs–InAlAs CQW structures, which, compared to the traditional polarization-modulation schemes, could provide significant reductions of drive electric fields and waveguide lengths for devices based on it [2]. In this scheme, an electric field, F, is applied to the optical waveguide containing multiple

---

A version of this chapter has been submitted for publication. S. Ristic and N. A. F. Jaeger, "Improved Push–Pull Polarization Modulation Using Coupled Quantum-Well Structures," *IEEE. Photon. Technol. Lett.*

repetitions of two types of CQW structure, which, in this manuscript, we will refer to as structure #1 and structure #2. As a result, structure #1 provides a large, positive change of the refractive index for TM-polarized light (Δn_{TM1}), accompanied by a smaller change of the refractive index for TE-polarized light (Δn_{TE1}). Similarly, structure #2 provides a large, negative change of the refractive index for TE-polarized light (Δn_{TE2}), accompanied by a smaller change of the refractive index for TM-polarized light (Δn_{TM2}). Placed together in an optical waveguide, the two structures could provide equal-magnitude and opposite-sign changes of the effective refractive indices for the fundamental TE and TM modes ($\Delta n_{eff(TE)}$ and $\Delta n_{eff(TM)}$) and enable push-pull polarization modulation [2]. Subsequent investigation into the effect that layer thickness and compositional variations have on the two CQW structures revealed that structure #2 is quite sensitive to these variations, which would make polarization modulators using this structure challenging to grow reliably [3]. The main reason for the poor robustness of structure #2 is that its electrorefraction is based on anticrossing of the two lowest energy heavy-hole wave functions (Ψ_{HH1} and Ψ_{HH2}), which have large masses and are thus very sensitive to the variations [3]. Here, we show how to redesign structure #2 [see Fig. 6.1(b)] to obtain a structure with dramatically improved robustness by designing its electrorefraction to be based on the anticrossing of the two lowest-energy electron wave functions (Ψ_{E1} and Ψ_{E2}), which have much smaller masses. We also show how structure #1 [see Fig. 6.1(a)], with its electrorefraction based on anticrossing of the two lowest-energy light-hole wave functions (Ψ_{LH1} and Ψ_{LH2}), could be improved. Modeling of each

structure is performed for 1550 nm light and is based on the variational method to solve the exciton equation in the effective-mass approximation [4].

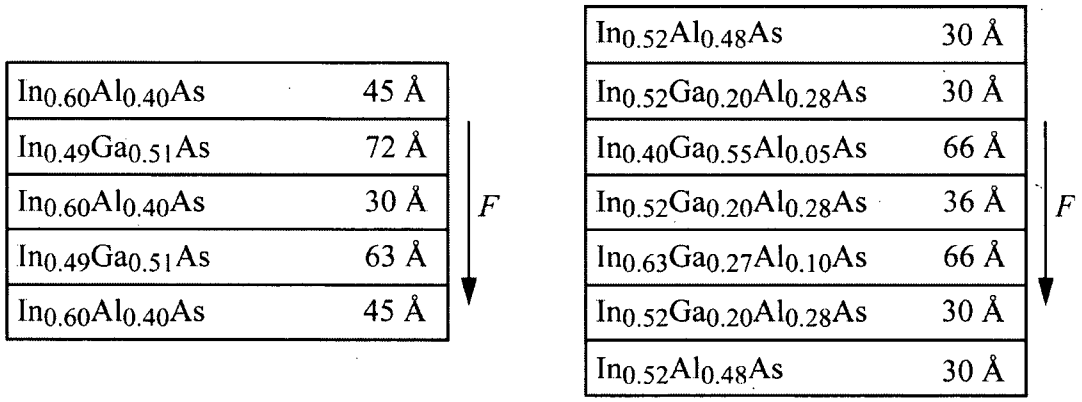

Figure 6.1: Schematic of layers for (a) structure #1 and (b) structure #2.

6.2 Improved Structure #1 and Structure #2

Fig. 6.2(a) illustrates the band edge diagram and the wave functions for structure #1, for F = 15 and 30 kV/cm. The left-hand side well (QW1) is made wider in order for Ψ_{E1} and Ψ_{LH1} to be mainly localized in it for F ≈ 0 kV/cm. As F is increased, Ψ_{LH1} and Ψ_{LH2} anticross at the resonant field $F_{LH} \approx 8$ kV/cm. Similar to [2], the electric field region of interest (15 kV/cm ≤ F ≤ 30 kV/cm) is above the resonant field, and Δn_{TM1} has a positive slope [see Fig. 6.3(a)]. This is because at F_{LH} both the 1S excitons corresponding to the symmetric-mode transitions (Ψ_{E1}–Ψ_{LH1} and Ψ_{E2}–Ψ_{LH2}) and the asymmetric-mode

transitions (Ψ_{E1}–Ψ_{LH2} and Ψ_{E2}–Ψ_{LH1}) have large radii (*i.e.*, small binding energies) and make small contributions to the TM-polarization absorption coefficient, and, in turn, via the Kramers–Krönig relation, to the refractive index [2]. As F is increased, the refractive index also increases, as the absorption

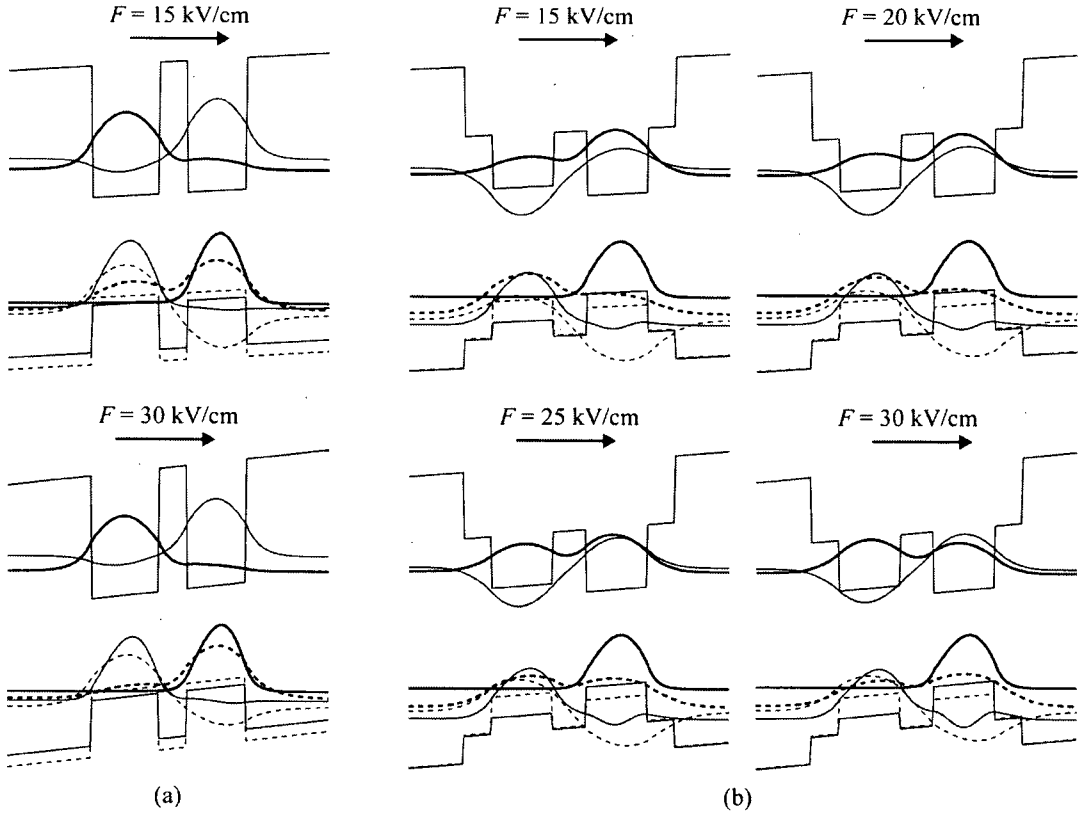

Figure 6.2: (a) Structure #1's wave functions and energy band diagram for F = 15 and 30 kV/cm. Band gap is not shown to scale. Ψ_{E1}, Ψ_{LH1}, and Ψ_{HH1} are shown as thick lines, while Ψ_{E2}, Ψ_{LH2}, and Ψ_{HH2} are shown as thin lines. In addition, light-hole wave functions and band edge are shown as dashed lines and (b) structure #2's wave functions and band diagram for F = 15, 20, 25, and 30 kV/cm. Here, Ψ_{HH3} is shown, instead of Ψ_{HH2}, as a full thin line.

coefficient is dominated by the asymmetric-mode excitons that become well confined and thus have small radii. As also shown in Fig. 6.3(a), Δn_{TE1} has a positive, although much

smaller, slope because the light-hole momentum matrix element is smaller for the TE polarization, and Ψ_{HH1} and Ψ_{HH2} do not anticross and make a negligible contribution to the electrorefraction [2].

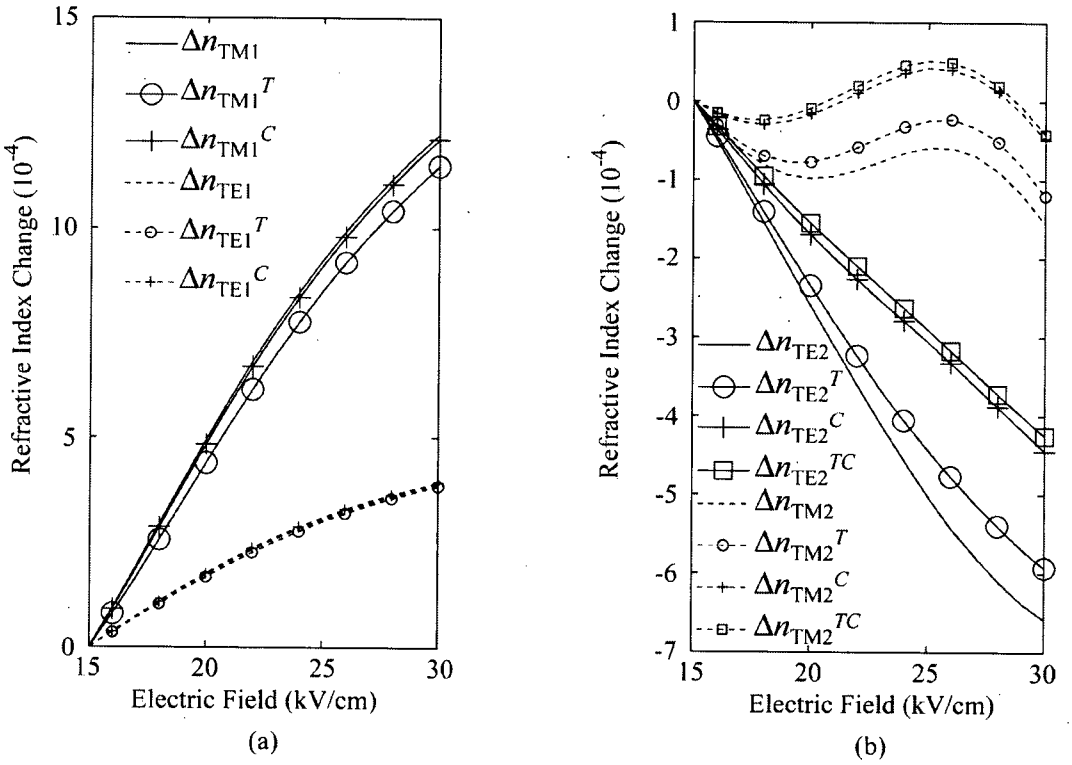

Figure 6.3: Effects of the layer variations on (a) Δn_{TE1} and Δn_{TM1} and (b) on Δn_{TE2} and Δn_{TM2} for 1550 nm operation wavelength.

Compared to structure #1 in [2], our new structure #1 offers two main improvements. First, QW1 and QW2 are under tensile strain in order to increase the energy separation between the electron and the heavy-hole wave functions. Consequently, the absorption coefficient for the TE polarization at the wavelength of operation is decreased. The compressive strain in the barriers is added to balance the total strain in structure #1 and

structure #2. Second, for the electric field region of interest, Ψ_{HH1} is localized in the right-hand side well (QW2) rather than QW1. The lowest energy $\Psi_{E1}-\Psi_{HH1}$ transition is, therefore, indirect, which should further reduce the TE polarization absorption. Here, the $\Psi_{E1}-\Psi_{HH1}$ energy separation corresponds to $\lambda = 1439$ nm for $F = 15$ kV/cm, and, similarly, the $\Psi_{E1}-\Psi_{LH1}$ energy separation corresponds to $\lambda = 1411$ nm. Considering these large energy separations and the fact that the high-energy asymmetric-mode excitons dominate the optical absorption above F_{LH}, the optical losses at 1550 nm should be small [5]. Also, localization of Ψ_{HH1} in QW2, rather than in QW1, offers another important benefit. For the electric fields of interest, it is easier to confine Ψ_{HH1} to QW2 than to QW1, so that the 3 Å thickness and 1 % compositional variations considered below cannot redistribute the heavy-hole wave functions and cause sharp dips in the refractive index change curves for the TE polarization [3].

We study the effects of the thickness and compositional variations on structure #1 separately, with no intention to model any specific growth process. To do so, the thicknesses of QW1, QW2, and the middle barrier are changed by ±3 Å independently (*i.e.*, 27 variations). For both polarizations, the refractive index change corresponding to each variation is multiplied by the variation's occurrence probability of 1/27 and added in the average refractive index change for TE polarization ($\Delta n_{TE1}{}^{T}$) or TM polarization ($\Delta n_{TM1}{}^{T}$). This is equivalent to having $p_w = 1/3$ in [3]. Similarly, the InAs composition in

all five layers is changed by ±0.01 (*i.e.*, 243 variations) and, using $p_c = 1/3$ [3], we obtain the average refractive index changes for each polarization ($\Delta n_{TE1}{}^{C}$ and $\Delta n_{TM1}{}^{C}$).

As illustrated in Fig. 6.3(a), structure #1 is quite insensitive to both thickness and compositional variations. Its insensitivity to compositional variations is, in part, due to the insensitivity of the light-hole band edge to these variations [3]. Also, the structure's insensitivity to both thickness and compositional variations is, in part, due to the small valence-band discontinuity ratio of the InGaAs–InAlAs material system [4]. The confinement of the anticrossing light-hole wave functions to the quantum well layers is, thus, small and the light-hole wave functions are, in turn, less sensitive to the thickness and compositional variations that occur in these layers.

The band edge diagram and the wave functions for structure #2 are shown in Fig. 6.2(b). Here, it is Ψ_{HH1} and Ψ_{HH3} that are shown in the figure as they make the main contributions to the electrorefraction (Ψ_{HH2} has negligible magnitude in QW1 and a node in QW2). The function of the small $In_{0.52}Ga_{0.20}Al_{0.28}As$ barriers is to decrease the confinement of the anticrossing electron wave functions and decrease their sensitivities to the layer variations [4]. The large $In_{0.52}Al_{0.48}As$ barriers are sufficiently far from QW1 and QW2 to significantly affect the sensitivities of the wave functions, and they help to confine the wave functions and decouple neighboring CQW structures. As shown in Fig. 6.2(b), the compressive strain in QW2 is used to make it deeper for Ψ_{E1} and Ψ_{HH1},

confining them for $F = 15$ kV/cm, while the tensile strain in QW1 is used to make it only slightly deeper for Ψ_{LH1}, confining it for $F = 15$ kV/cm and allowing it to move toward QW2 for larger F. The wavelengths corresponding to the $\Psi_{E1}-\Psi_{HH1}$ and $\Psi_{E1}-\Psi_{LH1}$ energy separations are 1391 nm and 1312 nm, respectively. As F is increased to 30 kV/cm, Ψ_{E1} and Ψ_{E2} become approximately equally shared by QW1 and QW2 giving the largest heavy-hole exciton radii and the smallest refractive index for the TE polarization [4] [see Fig. 6.3(b)]. Simultaneously, Ψ_{LH1} becomes approximately equally shared by the two wells, also giving largest exciton radii and smallest refractive index for the TM polarization. However, unlike in the CQW structures mentioned above, here, both the conduction-band, *i.e.*, electron, and the valence-band, *i.e.*, light-hole, wave functions exchange wells as F is increased. Consequently, the overlaps between Ψ_{E1} and Ψ_{LH1} as well as Ψ_{E2} and Ψ_{LH2} reach their maxima for $F \approx 25$ kV/cm, and Δn_{TM2} does not have the smooth, negative slope typical for CQW structures. Rather, it is a nonlinear function [see Fig. 6.3(b)], and a desirable large difference between Δn_{TE2} and Δn_{TM2} is achieved.

As illustrated in Fig. 6.3(b), structure #2 is not very sensitive to 3 Å thickness variations ($p_w = 1/3$), but it is somewhat sensitive to the compositional variations ($p_c = 1/3$). Since structure #2 has more layers than structure #1, most of which are also quaternary compounds, only the variations in the quantum wells are considered in order to keep the number of simulations manageable. Simulations show that the thickness and the compositional variations in the barriers, as compared to the wells, have much smaller

effects on the distributions of the wave functions, which justifies the approximation. Also, the effects of compositional variations are well approximated by restricting the changes of the Ga and Al mole fractions in each well to have the same magnitudes but opposite signs. Fig. 6.3(b) also shows the effect of treating the thickness and compositional variations as being coupled ($\Delta n_{TE2}{}^{TC}$ and $\Delta n_{TM2}{}^{TC}$).

Fig. 6.4(a) shows the effects that the layer variations have on $\Delta n_{eff(TE)}$ and $\Delta n_{eff(TM)}$ of the 1D waveguide in Fig. 6.4(b). $\Delta n_{eff(TE)}$ and $\Delta n_{eff(TM)}$ are obtained using the designed values for refractive index change curves (Δn_{TE1}, Δn_{TM1}, Δn_{TE2}, and Δn_{TM2}), biasing the electric field at $F_B = 23$ kV/cm, and applying an electric field change of $\Delta F = \pm 3$ kV/cm. The magnitudes of $\Delta n_{eff(TE)}$ and $\Delta n_{eff(TM)}$ are very similar, and polarization switching between two orthogonal states could be achieved for an electrode length of $L = 3.2$ mm. However, if for the same F_B, ΔF, and L we consider the effects of the layer variations on polarization modulation, Fig. 6.3 shows that the magnitudes of the effective index changes for the TE and TM polarizations ($\Delta n_{eff(TE)}{}^{I}$ and $\Delta n_{eff(TM)}{}^{I}$) become very different. Here, the actual variations that can be expected in the epitaxial layers are approximated by $\Delta n_{TE1}{}^{T}$ and $\Delta n_{TM1}{}^{T}$ in structure #1 and by $\Delta n_{TE1}{}^{TC}$ and $\Delta n_{TM1}{}^{TC}$ in structure #2. Due to the nonlinear shape of Δn_{TM2}, the magnitudes of the two effective index changes can be matched by changing the values of F_B and ΔF. In addition, if the long electrode is split into two equal-length electrodes ($L_1 = L_2 = 1.6$ mm), each having a different bias field

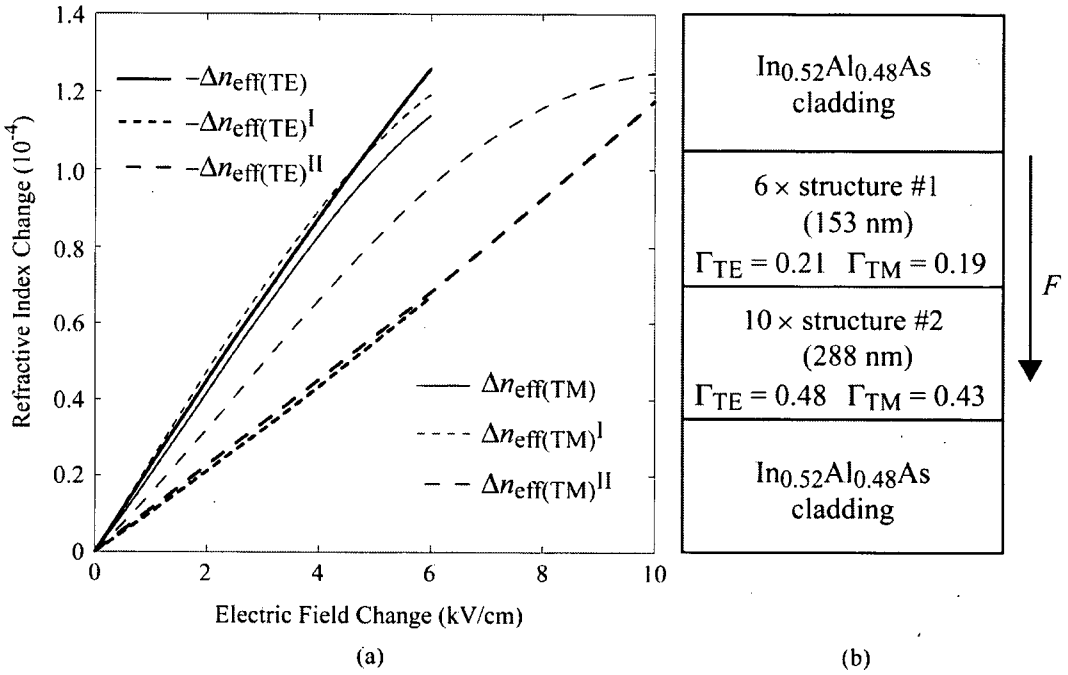

Figure 6.4: (a) Effects of the layer variations on $\Delta n_{eff(TE)}$ and $\Delta n_{eff(TM)}$ in a (b) 1-dimensional waveguide containing 6 periods of structure #1 and 10 periods of structure #2. In each CQW region, Γ_{TE} and Γ_{TM} are the optical confinement factors for the TE and TM fundamental modes.

(F_{B1} = 20 kV/cm and F_{B2} = 27 kV/cm) and the same field change $\Delta F = \pm 5$ kV/cm, not only would the effective index changes ($\Delta n_{eff(TE)}^{II}$ and $\Delta n_{eff(TM)}^{II}$) have closely matched magnitudes, but also the curvatures of the TM response would cancel themselves to an extent, making the TM response more linear [see Fig. 6.4(a)]. The nominal polarization switching efficiency in [2] is somewhat better than here, considering that the structures in [2] have smaller values for Γ_{TE} and Γ_{TM} (Γ_{TE} = 0.43 and Γ_{TM} = 0.37 for 10 periods of the old structure #1 and Γ_{TE} = 0.19 and Γ_{TM} = 0.17 for 6 periods of the old structure #2, respectively) and still provide a smaller $\Delta F \times L$ product (5 kV/cm × 3.5 mm). However, the new structures are more robust to the layer variations and provide for the possibility

of matching the magnitudes of $\Delta n_{eff(TE)}$ and $\Delta n_{eff(TM)}$ even in the presence of these variations.

References

[1] J. D. Bull, et al., "40 GHz electro-optic polarization modulator for fiber optic communications systems," in *Proc. of SPIE*, 2004, vol. 5577, pp. 133–143.

[2] S. Ristic and N. A. F. Jaeger, "Push–pull polarization conversion using novel asymmetric coupled quantum-well structures," *IEEE Photon. Technol. Lett.*, vol. 18, no. 2, pp. 316–318, 2006.

[3] S. Ristic and N. A. F. Jaeger, "Influence of layer thickness and compositional variations on the electrorefractive properties of a quantum well polarization-conversion modulator," *J. Vac. Sci. Technol. A, Vac. Surf. Films*, vol. 24, no. 4, pp. 962–965, 2006.

[4] S. Ristic and N. A. F. Jaeger, "Robust coupled-quantum-well structure for use in electrorefraction modulators," *IEEE. Electron Dev. Lett.*, vol. 28, no. 1, pp. 30–32, 2007.

[5] W. Bardyszewski, D. Yevick, Y. Liu, C. Rolland, and S. Bradshaw, "Theoretical and experimental analysis of Mach–Zehnder quantum-well modulators," *J. Appl. Phys.*, vol. 80, no. 2, pp. 1136–1141, 1996.

Chapter 7
Summary, Conclusions, and Suggestions for Future Work

7.1 Summary

It was clear in the early stages of the research presented in this thesis that ER modulators based on CQW structures would be strong competitors to other modulator technologies in future-generation digital and analog optical links. For example, compared to SQWs, CQW structures can provide similar refractive index changes for considerably lower drive electric fields. In addition, the exciton absorption peaks in CQW structures exhibit smaller red shifts, so that ER modulators based on CQW structures are expected to have smaller absorption coefficients and electric-field-induced changes of the absorption coefficients at the wavelength of operation than ER modulators based on SQWs. Consequently, ER CQW modulators have great potential to exceed the performance of ER SQW modulators in applications requiring ultra-fast intensity modulation. The same is true for polarization modulators. Push-pull polarization modulators based on CQW

structures are expected to have ultra-wide electro-optic bandwidths, low drive voltages, low differential group delays, and small voltage-dependent changes in the absorption. When compared to EA SQW modulators, ER CQW intensity modulators are expected to have lower chirp and lower drive voltages. Also, as they operate at wavelengths that are further from the lowest energy exciton (*i.e.*, they are more detuned) and, thus, absorb less light, the ER CQW intensity modulators are expected to have smaller temperature and wavelength dependences and higher optical saturation powers.

The thesis presents, in a chronological order, work aimed at improving the state-of-the-art of electro-optic modulators based on CQW structures. In Chapter 2, a design for the first quantum-well-based push-pull polarization modulator was presented. The conceptual push-pull polarization modulation was achieved by placing multiple repetitions of two different InGaAlAs–InAlAs CQW structures in the optical waveguide of the modulator. The electroabsorption in these CQW structures, and also in all of the InGaAlAs-based CQW structures designed in this thesis, was modeled by solving the 1S exciton equation in the effective-mass envelope-function approximation using the variational method, and the electrorefraction was obtained using the Kramers–Krönig relations. One of the two structures contains a small amount of tensile strain (TS structure) and provides a large increase of the refractive index for the TM polarization and only a small increase of the refractive index for the TE polarization. The other structure contains a small amount of compressive strain (CS structure) and provides a large decrease of the refractive index for

the TE polarization and only a small decrease of the refractive index for the TM polarization. The novel function of biaxial strain in each of the two structures was to achieve a large difference in the refractive index changes for the TE and TM polarizations. Placing 10 repetitions of the TS structure and 6 repetitions of the CS structure in a slab waveguide, similar-magnitude and opposite-sign changes of the effective refractive indices for the TE and TM modes were predicted for an electric-field change of 5 kV/cm, providing a 90° polarization rotation in a 3.4 mm long waveguide.

In Chapter 3, the sensitivities of the TS and CS structures to thickness and compositional variations were studied. Although the wave functions that contribute to the electrorefraction effects in CQW structures become less sensitive to the variations when the thicknesses of the middle barriers are decreased [1], doing so also decreases the slopes of the electric-field-induced refractive index changes [2]. The goal of the study in Chapter 3 was to obtain a better understanding of the TS and CS structures' sensitivities to the layer variations, and, eventually, based on the knowledge obtained from the study, minimize the effects of the layer variations without resorting to very thin middle barriers. It was found that the CS structure is very sensitive to the layer variations because its electrorefraction effect is based on the anticrossing of the two lowest energy heavy-hole wave functions and that the TS structure is quite insensitive to the layer variations because its electrorefraction effect is based on the anticrossing of the two lowest energy light-hole wave functions. The effective masses of the heavy-hole wave functions are

considerably larger than those of the light-hole wave functions, and distributions of heavy-holes wave functions in CQW structures are, therefore, more susceptible to any thickness or compositional variations in the CQW structures [1]. Although the CS structure provides a very large change of the refractive index change for the TE polarization and a very small change of the refractive index change for the TM polarization, which is very desirable in polarization modulators, it was clear from the study that major improvements of the CS structures needed to be done because of their great sensitivities to the layer variations. It was also learned from the study that the TS structure was quite insensitive to the compositional variations because the energy of the light-hole band edge depends less on the compositional variations than do the energies of the heavy-hole and electron band edges. It was anticipated that the TS structure could be made very robust to the layer variations if slightly redesigned in order to prevent the undesirable anticrossing of the two lowest energy heavy holes, which caused undesirable dips in the refractive index response for the TE polarization.

In Chapter 4, inspired by the robustness of the TS structure, a lattice-matched InGaAs–InAlAs CQW structure (structure #1) that has it electrorefractive effect based on the anticrossing of the two lowest energy light-hole wave functions, and is, thus, more appropriate for TM modulation, was compared with a similar lattice-matched InGaAs–InAlAs CQW structure (structure #2) that has it electrorefractive effect based on the anticrossing of the two lowest energy electron wave functions, and is, thus, more

appropriate for TE modulation. It was demonstrated that structure #1 is considerably less sensitive to the 3 Å thickness variations and the 2 % compositional variations and that InGaAlAs-based CQW structures that have their electrorefraction effects based on anticrossing of the light holes are a preferable technology for the future ER modulators. Besides the insensitivity of the light-hole band edge to compositional variations, it was seen in this study that there was an additional mechanism which contributed to structure #1's small sensitivity to both thickness and compositional variations. It was shown that a small valence band discontinuity ratio in InGaAlAs-based systems makes anticrossing light-hole wave functions quite insensitive to relative differences in thickness and composition between the two quantum wells because shallow quantum wells provide only weak confinement to the light-hole wave functions. Consequently, the magnitudes of the light-hole wave functions in the quantum well layers are relatively small, and so are the probabilities that the relative distributions of the wave functions between the two quantum wells can be affected by the thickness and compositional variations in the two quantum wells.

In Chapter 5, building on the findings in Chapter 4, it was shown that decreasing the confinements of electron wave functions in CQW structures could be used to improve the robustness to growth of EA and ER modulators that have their respective electroabsorption and electrorefraction effects based on anticrossing of electron wave functions. A lattice-matched CQW structure (S_A) that has ternary wells ($In_{0.53}Ga_{0.47}As$)

and ternary barriers ($In_{0.52}Al_{0.48}As$) was compared to another lattice-matched CQW structure (S_B) that has ternary wells ($In_{0.53}Ga_{0.47}As$) and quaternary barriers ($In_{0.52}Ga_{0.24}Al_{0.24}As$). The middle barrier in S_B was made wider than the one in S_A in order to compensate for its smaller height and provide the same sensitivities of the lowest energy electron wave functions in the two structures to the same change in the electric field. Although the lowest energy electron wave function in S_B has the same sensitivity to the electric field as the lowest energy electron wave function in S_A, it is considerably less sensitive to the 3 Å thickness variations and only slightly more sensitive to the 10 meV potential energy variations that can be expected to occur in the quantum well and barrier layers during growth. Consequently, increasing the thicknesses of the middle barriers in CQW structures and decreasing the confinements of the anticrossing electron wave functions by decreasing the potential energies of all barriers (or increasing the potential energies of the quantum wells) can be used as a design method for improving the overall robustness to growth in these structures. The same is true for the CQW structures where the anticrossing of the light-hole wave functions is used. However, as was shown in Chapter 3, anticrossing of the heavy-hole wave functions should be avoided because their large effective masses make them extremely sensitive to layer thickness and compositional variations.

In Chapter 6, the design method presented in Chapter 5 was used to improve the performance of the CS structure in Chapters 2 and 3. Although it is designed to achieve

the same effect as the CS structure, *i.e.*, large electric-field-induced decrease of the refractive index for the TE polarization without a commensurate decrease of the refractive index for the TM polarization, the new structure (structure #2) has two important characteristics that distinguish it from the original CS structure.

First, the large refractive index change for the TE polarization and the small refractive index change for the TM polarization in structure #2 are achieved via anticrossing electron wave functions, rather than heavy-hole wave functions. The small effective masses of the anticrossing electron wave functions in structure #2 make them considerably less sensitive to layer thickness and compositional variations than the anticrossing heavy-hole wave functions in the CS structure. However, the large refractive index change for the TE polarization and the small refractive index change for the TM polarization is an effect that is not easily achieved via anticrossing electron wave functions. The large negative change of the refractive index for the TE polarization is achieved by anticrossing the two lowest energy electron wave functions and preventing the heavy-hole wave functions from making any significant electric-field-induced redistribution between the two wells of structure #2, as is typically done in ER CQW modulators [2], [3]. However, in order to achieve only a small change of the refractive index for the TM polarization, considering that the anticrossing of the electron wave functions is used, a small, controllable redistribution of the two lowest energy light-hole wave functions is allowed. The redistribution of the light-hole wave functions

accompanied by a lack of redistribution of the heavy-hole wave functions is facilitated by using tensile strain in the left-hand side well and compressive strain in the right-hand side well. The opposite-sign strains provide unequal potential energies for the heavy-hole and light-hole wave functions, strongly confining the heavy-hole wave functions and allowing the light-hole wave functions to slowly redistribute between the two wells. The electric-field-induced movement of the light-hole and electron wave functions does not provide the typical monotonic decrease or increase of the overlap integrals between these wave functions. Rather, the overlap integrals have an "S-shape" dependence on the electric field, which is also evident in the refractive index change for the TM polarization. Consequently, the refractive index change for the TM polarization remains small in the electric field region of interest.

Second, unlike the CS structure, the new structure #2 has very small quaternary barriers in the vicinity of two quantum wells in order to decrease the confinement of the anticrossing electron wave functions and, ultimately, improve the structure's sensitivity to the layer variations. Simulations show that the heights of the barriers far from the quantum wells, where the magnitudes of the electron wave functions are small, do not affect the wave functions' sensitivities to the layer variations. Consequently, the barriers in these regions are made ternary in order to provide better decoupling between the neighboring structures and to provide confinement to the second lowest energy light-hole

wave function and the third lowest energy heavy-hole wave function, both of which are included in the modeling of electrorefraction.

Structure #1 in Chapter 6 is not fundamentally different from the TS structure in Chapters 2 and 3. Similar to the TS structure, the main function of structure #1 is to provide a large increase of the refractive index for the TM polarization without a commensurate increase of the refractive index for the TE polarization, and this effect is achieved by anticrossing the two lowest energy light-hole wave functions. However, in structure #1, the lowest energy heavy-hole wave function is confined to the right-hand side well and not the left-hand side well. This configuration is more energetically favorable for the heavy holes, and the undesirable heavy-hole anticrossing evident in Chapter 3 is extinguished for the 3 Å thickness and 1 % compositional variations used in Chapter 6. Also, confining the lowest energy heavy-hole wave function to the right-hand side well in the electric field region of interest decreases the optical absorption strength associated with the lowest energy electron-heavy-hole transition (E1–HH1) and effectively decreases the optical loss for the TE polarization at the wavelength of operation. In addition, tensile strain is used in both wells of structure #1 in order to increase the wavelength detuning of the heavy-hole excitons, which typically have lower energies than the light-hole excitons, and to further decrease the optical loss for the TE polarization. The compressive strain in the barriers of structure #1 is used to balance the overall strain in structure #1 and structure #2. Although structure #1 is very insensitive to the 3 Å thickness and the 1 %

compositional variations, structure #2 still shows a certain degree of sensitivity to the compositional variations. However, it is pointed out in Chapter 6 that two inline, separately biased electrodes can be used to match the magnitudes as well as to linearize the opposite-sign refractive index changes for the TE and TM polarizations, further reducing the sensitivities of modulators based on structure #1 and structure #2 to layer variations.

7.2 Conclusions

As mentioned above, CQW structures have the potential to provide large electroabsorption and electrorefraction effects, which will allow devices using them to have short lengths and, consequently, ultra-wide electro-optic bandwidths, while maintaining small drive voltages. Also, unlike in SQWs, in which the electrorefraction effect is based mainly on red shifting the lowest energy excitons, in CQW structures, the electrorefraction effect is based on changing the overlaps between the conduction and valence wave functions, and there is no appreciable red shifting that causes electric-field-induced increases of the optical absorption. Besides these two benefits of CQW structures, the work presented in this thesis reveals at least four additional properties of CQW structures that will be important when designing future CQW modulators.

First, as the electrorefraction effect in a CQW structure is based on the electric-field-induced transfer of particles (electrons, light holes, or heavy holes) between the two wells, it is relatively easy to select which particles are allowed to transfer by manipulating the strain and geometry of the layers in the CQW structure. Consequently, CQW structures can provide for efficient polarization modulators because, again, electron-light-hole transitions solely contribute to the TM-polarization response and electron-heavy-hole transitions dominate the TE-polarization response.

Second, in InGaAlAs-based CQW structures, because of the very small dependence of the light-hole band edge on compositional variations in the quantum wells, because of the relatively small effective masses of light holes, and because of the small valence band discontinuity ratio, the anticrossing light-hole wave functions are far less sensitive to layer thickness and compositional variations than the anticrossing electron or heavy-hole wave functions. Consequently, an InGaAlAs-based CQW structure can be made to be quite sensitive to the electric field, by allowing the middle barrier to be fairly thick, and still remain quite insensitive to the layer thickness and compositional variations that are expected to occur during the growth process. As the light-hole momentum matrix element for the TM polarization is considerably larger than that for the TE polarization, CQW structures that utilize anticrossing of light-hole wave functions are suitable for TM phase and intensity modulators, such as structure #1 in Chapter 4, or polarization modulators, such as structure #1 in Chapter 6. Therefore, if the designers of future phase

and intensity modulators desire to use TM light in their devices, the best choice for these devices would be simple lattice-matched, ternary InGaAs–InAlAs CQW structures, which utilize the anticrossing of light holes (such as structure #1 in Chapter 4). In addition, if the designers want to make very efficient polarization modulators that are not necessarily push-pull devices, the best choice for these devices would be simple strained, ternary InGaAs–InAlAs CQW structures, which utilize the anticrossing of light holes (such as structure #1 in Chapter 6).

Third, certain devices, such as surface-normal modulators used in optical interconnects, free-space optical communications, and optical links requiring large-area and/or polarization insensitive devices, do not have optical waveguides. For example, in the surface-normal electroabsorption modulator in [4], light enters the stack of InGaAs–InAlAs CQW structures through a p-doped region at normal incidence and, thus, its electric-field vector is parallel to the planes of the quantum wells. This device is polarization-independent because the CQW structures provide the same electroabsorption effect for all directions of the electric-field vector around the optical axis. For this device and other devices requiring modulation of plane-parallel light, the anticrossing of electrons is a more efficient mode of operation than the anticrossing of light holes because the light-hole momentum matrix element for the plane-parallel light is relatively small. Of course, the anticrossing of electrons in a CQW structure is more efficient than the anticrossing of light holes only if the CQW structure can be designed so that the

electron wave functions are not significantly more sensitive to the layer thickness and compositional variation than the light-hole wave functions. Chapter 5 presents a method that designers of devices that modulate the plane-parallel light can use to make CQW structures based on the anticrossing of electrons more robust to the layer variations. The method requires barriers or quantum wells in CQW structures to be quaternary in order to weaken the confinement of the electron wave functions to the quantum well layers and allow them to tunnel to a greater extent into the external barriers. As argued in Chapter 5, the small increase of the wave functions' sensitivities to the compositional variations in the barriers is small compared to the large decrease of their sensitivities to both the thickness and compositional variations in the quantum well layers.

Fourth, as mentioned above, the CQW structures that utilize the anticrossing of light-hole wave functions, such as structure #1 in Chapter 6, can be used in polarization modulators because these structures provide large phase changes for the TM polarization, accompanied by only small phase changes for the TE polarization. On the other hand, for those applications that may require devices that provide large phase changes for the TE polarization accompanied by only small phase changes for the TM polarization, a CQW structure similar to structure #2 in Chapter 6 could be used. Again, in Chapter 6, the structure #2 was used together with structure #1 for a particular purpose, which is a realization of a robust CQW push-pull polarization modulator.

7.3 Suggestions for Future Work

In order to fully realize the potential that the CQW structures developed in this thesis have for improving the state-of-the-art in optical modulators, additional work will be necessary. This future work will include: (a) Growth and fabrication of CQW modulators, (b) Systematic performance tests of these devices, (c) Improvement of their electro-optic bandwidth, and (d) Integration of CQW modulators with other devices. Compared to the polarization modulators that could be realized using the CQW structures in Chapter 6, TM-phase modulators that could be realized using the robust structure #1 in Chapter 4 are the simplest to build and are the most likely to provide good results in the short term. Therefore, initial future research should likely focus on TM CQW modulators.

(a) Multiple repetitions of the CQW structure could be grown using Molecular Beam Epitaxy in a typical Mach–Zehnder p-i-n diode configuration, as illustrated in Fig. 1.17. The shape of the optical waveguide could be patterned using reactive ion etching. Each wafer can contain many Mach–Zehnder interferometers with 1–2 mm long branches. In order to avoid Fabry-Perot resonances, the optical waveguide facets could be angle-cleaved or antireflection coated.

(b) Mach–Zehnder interferometers containing multiple repetitions of the CQW structure should be tested for their basic operation, and their low-frequency electro-optic transfer

functions should be obtained. Extinction ratios greater than 15 dB and drive voltages lower than 1 V are expected. Should more details of the electroabsorption and the electrorefraction properties of the CQW structures be required (*e.g.*, in order to compare the experimental results with the modeling), the photocurrent spectra of single branches of the Mach–Zehnder interferometers could be obtained. The single-branch experiments may also include more detailed phase and absorption measurements [5]. All measurements should be performed across the communication wavelength bands using a tunable laser, and the modulator is expected to show a flat response at least across the C-band. More than one modulator design will likely be needed to cover the whole telecommunication spectrum.

(c) Once the basic functionality and moderately wide electro-optic bandwidths of the p-i-n devices are demonstrated, additional work should be focused on the design, fabrication, and testing of the traveling-wave electrodes that will provide ultrahigh bandwidths (~100 GHz). These electrodes will not necessarily be of the typical p-i-n diode configuration. They may be coplanar strip or coplanar waveguide electrodes with Schottky contacts [6], or the new type of substrate-removed microstrip-like electrode recently introduced [7], [8].

(d) In order for CQW modulators to be competitive in future optical links, it will also be important to eventually integrate them with other devices (*e.g.*, lasers, photodetectors,

wavelength converters, optical amplifiers, etc.) on a single chip. The monolithic integration of several optoelectronic devices on a single chip reduces the cost of packaging, reduces the coupling losses between devices, reduces the power consumption, and improves the circuit reliability. How the integration will be achieved will depend on the photonic integrated circuit of interest [9].

Growth, fabrication, and testing procedures for the TE-polarization intensity modulators will be basically the same as those for the TM-polarization modulators. As CQW polarization modulators contain multiple repetitions of two types of CQW structure, each type of CQW structure should be grown, fabricated, and tested separately in procedures similar to the ones described above. Only when the electroabsorption and the electrorefraction properties of each type of CQW structure are well known, should the two structures can be put together in the optical waveguide of a polarization modulator for further optimization and testing. Also, if a polarization modulator is not intended to be used in the push-pull mode of operation, the device can be based on only one for the two structures presented in Chapter 6, *e.g.*, structure #1. Although the CQW polarization modulators based on the strained structures presented in Chapter 6 are more difficult to realize than the TM-phase modulators based on structure #1 presented in Chapter 4, both types of device are expected to provide state-of-the-art performance predicted by the modeling.

References

[1] R. Lang and K. Nishi, "Electronic state localization in semiconductor superlattices," *Appl. Phys. Lett.*, vol. 45, no. 1, pp. 98–100, 1984.

[2] C. Thirstrup, "Refractive index modulation based on excitonic effects in GaInAs-InP coupled asymmetric quantum wells," *IEEE J. Quantum Electron.*, vol. 31, no.6, pp. 988–996, 1995.

[3] H. Feng, J. P. Pang, M. Sugiyama, K. Tada, Y. Nakano, "Field-induced optical effect in a five-step asymmetric coupled quantum well with modified potential," *IEEE J. Quantum Electron.*, vol. 34, no. 7, pp. 1197–1208, 1998.

[4] T. H. Stievater, W. S. Rabinovich, P. G. Goetz, R. Mahon, and S. C. Binari, "A surface-normal coupled-quantum-well modulator at 1.55 μm," *IEEE Photon. Technol. Lett.*, vol. 16, no. 9, pp. 2036–2038, 2004.

[5] D. J. Krause and J. C. Cartledge, *IEEE Photon. Technol. Lett.*, vol. 16, no. 8, pp. 1915–1917, 2004.

[6] J. P. Pang, K. Tada, Y. Nakano, H. Feng, "Multiple-quantum-well traveling-wave-type ultra-high-speed optical modulator," in *Proc. OECC'98 Tech. Digest. (Optoelectronics and Communications Conference)*, 1998, paper 16B1–5, pp. 454–455.

[7] J. H. Shin, C. Ozturk, S. R. Sakamoto, Y. J. Chiu, and N. Dagli, "Novel T-rail electrodes for substrate removed low-voltage, high-speed GaAs/AlGaAs electro-optic modulators," *IEEE Trans. Microw. Theory Tech.*, vol. 53, no. 2, pp. 626–643, 2005.

[8] J. H. Shin, S. Wu, and N. Dagli, "Bulk undoped GaAs–AlGaAs substrate-removed electrooptic modulators with 3.7-V-cm drive voltage at 1.55 μm," *IEEE Photon. Technol. Lett.*, vol. 18, no. 21, pp. 2251–2253, 2006.

[9] L. A. Coldren, J. Raring, M. Sysak, J. Barton, and L. Johansson, "Improved functionality and performance in photonic integrated circuits," in *Proc. IPRM (International Conference on Indium Phosphide and Related Materials)*, 2006, paper PLE1, pp. 1–6.